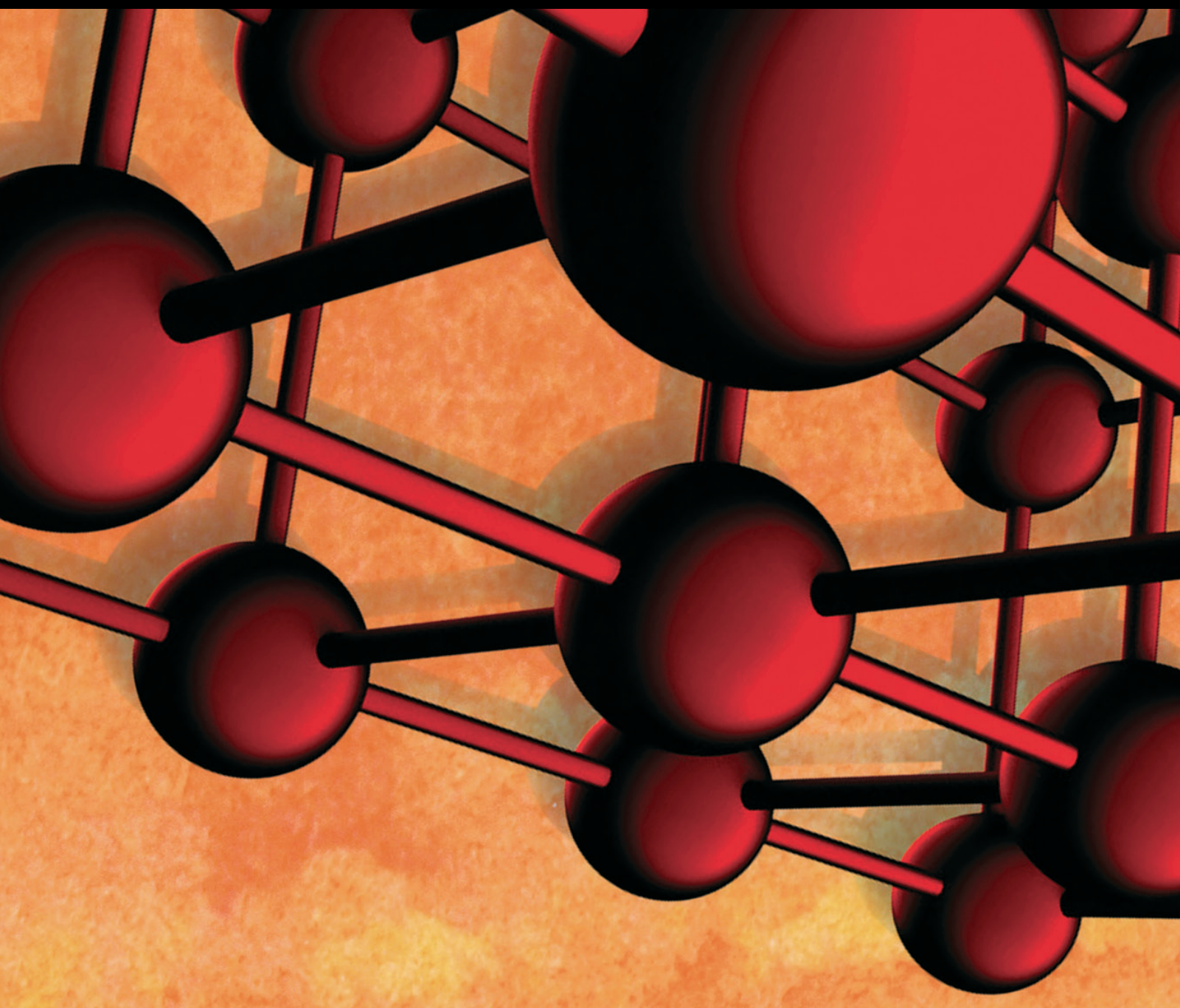


Advances in Materials Science and Engineering

# Brittle or Quasi-Brittle Fracture of Engineering Materials 2016

Guest Editors: Filippo Berto, Liviu Marsavina, Majid R. Ayatollahi, Sergei V. Panin, and Konstantinos I. Tserpes





---

**Brittle or Quasi-Brittle Fracture of  
Engineering Materials 2016**

Advances in Materials Science and Engineering

---

## **Brittle or Quasi-Brittle Fracture of Engineering Materials 2016**

Guest Editors: Filippo Berto, Liviu Marsavina,  
Majid R. Ayatollahi, Sergei V. Panin,  
and Konstantinos I. Tserpes



---

Copyright © 2016 Hindawi Publishing Corporation. All rights reserved.

This is a special issue published in “Advances in Materials Science and Engineering.” All articles are open access articles distributed under the Creative Commons Attribution License, which permits unrestricted use, distribution, and reproduction in any medium, provided the original work is properly cited.

## Editorial Board

- Michael Aizenshtein, Israel  
Jarir Aktaa, Germany  
Konstantinos Anthymidis, Greece  
Amit Bandyopadhyay, USA  
Arun Bansil, USA  
Massimiliano Barletta, Italy  
Mikhael Bechelany, France  
Jozef Bednarcik, Germany  
Avi Bendavid, Australia  
Jamal Berakdar, Germany  
Giovanni Berselli, Italy  
Patrice Berthod, France  
Didier Blanchard, Denmark  
Susmita Bose, USA  
H.-G. Brokmeier, Germany  
Steve Bull, United Kingdom  
Peter Chang, Canada  
Daolun Chen, Canada  
Gianluca Cicala, Italy  
Gabriel Cuello, France  
Narendra B. Dahotre, USA  
João P. Davim, Portugal  
Angela De Bonis, Italy  
Francesco Delogu, Italy  
Seshu B. Desu, USA  
Guru P. Dinda, USA  
Yong Ding, USA  
Nadka Tzankova Dintcheva, Italy  
Kaveh Edalati, Japan  
Philip Eisenlohr, USA  
Paolo Ferro, Italy  
Massimo Fresta, Italy  
Eric Freysz, France  
Sergi Gallego, Spain  
Santiago Garcia-Granda, Spain  
Filippo Giannazzo, Italy  
Daniel Guay, Canada  
Fawzy H. Samuel, Canada
- Hiroki Habazaki, Japan  
Joke Hadermann, Belgium  
Satoshi Horikoshi, Japan  
David Houivet, France  
Rui Huang, USA  
Michele Iafisco, Italy  
Katsuyuki Kida, Japan  
Jae-Ho Kim, Republic of Korea  
Akihiko Kimura, Japan  
Takayuki Kitamura, Japan  
Hongchao Kou, China  
Prashant Kumta, USA  
Luciano Lamberti, Italy  
Heinrich Lang, Germany  
Pavel Lejcek, Czech Republic  
Cristina Leonelli, Italy  
Ying Li, USA  
Jun Liu, China  
Meilin Liu, Georgia  
Wei Liu, France  
Yunqi Liu, China  
Fernando Lusquiños, Spain  
Peter Majewski, Australia  
Philippe Miele, France  
Hossein Moayedi, Iran  
Paul Munroe, Australia  
Rufino M. Navarro, Spain  
Luigi Nicolais, Italy  
Hiroschi Noguchi, Japan  
Chérif Nouar, France  
José L. Ocaña, Spain  
Tsutomu Ohzuku, Japan  
Olanrewaju Ojo, Canada  
Gianfranco Palumbo, Italy  
Anna Paradowska, Australia  
Matthew Peel, United Kingdom  
Gianluca Percoco, Italy  
Giorgio Pia, Italy
- Jean-Francois Pierson, France  
Simon C. Potter, Canada  
Manijeh Razeghi, USA  
Yuri Ribakov, Israel  
Anna Richelli, Italy  
Antonio Riveiro, Spain  
Pascal Roussel, France  
Timo Sajavaara, Finland  
Antti Salminen, Finland  
Carlo Santulli, Italy  
Franz-Josef Schmitt, Germany  
Jainagesh A. Sekhar, USA  
Fridon Shubitidze, USA  
Maria A. Signore, Italy  
Donato Sorgente, Italy  
Charles C. Sorrell, Australia  
Costas M. Soukoulis, USA  
Sam-Shajing Sun, USA  
Kohji Tashiro, Japan  
Somchai Thongtem, Thailand  
Achim Trampert, Germany  
Filip Tuomisto, Finland  
Krystyn Van Vliet, USA  
Qiang Wang, China  
Rong Wang, USA  
Rui Wang, China  
Lu Wei, China  
Jörg M. K. Wieszorek, USA  
Wei Wu, USA  
Hemmige S. Yathirajan, India  
Wenbin Yi, China  
Belal F. Yousif, Australia  
Jinghuai Zhang, China  
Li Zhang, China  
Ming-Xing Zhang, Australia  
Wei Zhou, China

# Contents

---

## **Brittle or Quasi-Brittle Fracture of Engineering Materials 2016**

Filippo Berto, Liviu Marsavina, Majid R. Ayatollahi, Sergei V. Panin, and Konstantinos I. Tserpes  
Volume 2016, Article ID 7094298, 2 pages

## **Investigation on Dynamic Propagation Characteristics of In-Plane Cracks in PVB Laminated Glass Plates**

Xiaoqing Xu, Bohan Liu, and Yibing Li  
Volume 2016, Article ID 1468390, 13 pages

## **Influence of Grain Boundary on the Fatigue Crack Growth of 7050-T7451 Aluminum Alloy Based on Small Time Scale Method**

Weihan Wang, Weifang Zhang, Hongxun Wang, Xiaoliang Fang, and Xiaobei Liang  
Volume 2016, Article ID 7671530, 7 pages

## **Prediction Intervals for the Failure Time of Prestressed Concrete Beams**

Sebastian Szugat, Jens Heinrich, Reinhard Maurer, and Christine H. Müller  
Volume 2016, Article ID 9605450, 8 pages

## **On the Tensile Strength of Granite at High Strain Rates considering the Influence from Preexisting Cracks**

Mahdi Saadati, Pascal Forquin, Kenneth Weddfelt, and Per-Lennart Larsson  
Volume 2016, Article ID 6279571, 9 pages

## **Modelling Thermal Shock in Functionally Graded Plates with Finite Element Method**

Vyacheslav N. Burlayenko  
Volume 2016, Article ID 7514638, 12 pages

## **Quasi-Brittle Fracture Modeling of Preflawed Bitumen Using a Diffuse Interface Model**

Yue Hou, Fengyan Sun, Wenjuan Sun, Meng Guo, Chao Xing, and Jiangfeng Wu  
Volume 2016, Article ID 8751646, 7 pages

## **Effect of the Yield Criterion of Matrix on the Brittle Fracture of Fibres in Uniaxial Tension of Composites**

Sergei Alexandrov, Yaroslav Erisov, and Fedor Grechnikov  
Volume 2016, Article ID 3746161, 7 pages

## **Mechanical Behavior of 3D Crack Growth in Transparent Rock-Like Material Containing Preexisting Flaws under Compression**

Hu-Dan Tang, Zhen-De Zhu, Ming-Li Zhu, and Heng-Xing Lin  
Volume 2015, Article ID 193721, 10 pages

## Editorial

# Brittle or Quasi-Brittle Fracture of Engineering Materials 2016

**Filippo Berto,<sup>1</sup> Liviu Marsavina,<sup>2</sup> Majid R. Ayatollahi,<sup>3</sup>  
Sergei V. Panin,<sup>4</sup> and Konstantinos I. Tserpes<sup>5</sup>**

<sup>1</sup>*Department of Engineering Design and Materials, Norwegian University of Science and Technology (NTNU),  
7491 Trondheim, Norway*

<sup>2</sup>*Faculty of Mechanical Engineering, Politehnica University of Timisoara, Blvd. M. Viteazu, Nr. 1,  
300222 Timisoara, Romania*

<sup>3</sup>*Fatigue and Fracture Research Laboratory, Center of Excellence in Experimental Solid Mechanics and Dynamics,  
School of Mechanical Engineering, Iran University of Science and Technology, Narmak, Tehran 16846, Iran*

<sup>4</sup>*Institute of Strength Physics and Material Science, Department of Mechanical Engineering & Aeronautics,  
Russian Academy of Sciences, Siberian Branch, Tomsk 634021, Russia*

<sup>5</sup>*Laboratory of Technology & Strength of Materials (LTSM), Department of Mechanical Engineering & Aeronautics,  
University of Patras, 26500 Patras, Greece*

Correspondence should be addressed to Filippo Berto; [berto@gest.unipd.it](mailto:berto@gest.unipd.it)

Received 22 September 2016; Accepted 22 September 2016

Copyright © 2016 Filippo Berto et al. This is an open access article distributed under the Creative Commons Attribution License, which permits unrestricted use, distribution, and reproduction in any medium, provided the original work is properly cited.

Brittle or quasi-brittle fracture of engineering materials is a wide field of research, which involves many researchers devoted to investigate different aspects of the mechanics and physics of fracture. Materials usually treated include metal alloys, polymers, composites, rocks, and ceramics.

Brittle failure is not a phenomenon limited only to static loading. It may also be related to the fatigue and failure under repeated loading cycles (mechanical or thermal). The material damage process is usually very complex because it involves the combined effects of loading, size and geometry, temperature, and environment. The understanding of the phenomena tied to the dissipation of energy in various forms and the identification of microscopic properties and their interactions with macroscopic variables are the actual challenging topics. The fracture mechanics science emphasizes material characterization techniques and translation of specimen data to design.

The present special issue contains original research and review articles that seek to define possible criteria against brittle and quasi-brittle failure and to present or discuss new sets of experimental data in combination with fracture assessment. Among the areas emphasized in the SI are case histories; material selection and structure design; sample calculations of practical design problems; material

characterization procedures; fatigue crack growth and corrosion; nondestructive testing and inspection; structural failure and ageing; failure prevention methodologies; and maintenance and repair. The papers submitted by the authors have been subjected to the normal journal peer-review process.

The papers submitted by the authors have been subjected to the normal journal peer-review process. Special topics include but are not limited to continuum mechanics, crack propagation, criteria for fatigue and fracture assessment, micromechanics, nanomechanics, energy absorption and dissipation, local approaches based on strain energy density, local approaches based on stress analysis, scale effect, singular stress field, interface behavior of small and large bodies, and three-dimensional effects.

## Acknowledgments

We thank the many anonymous reviewers who assisted us in the review process providing useful comments and proposing constructive improvements to the authors. Without their continuous and valuable support also our efforts could have been useless.

*Filippo Berto*  
*Liviu Marsavina*  
*Majid R. Ayatollahi*  
*Sergei V. Panin*  
*Konstantinos I. Tserpes*

## Research Article

# Investigation on Dynamic Propagation Characteristics of In-Plane Cracks in PVB Laminated Glass Plates

**Xiaoqing Xu, Bohan Liu, and Yibing Li**

*State Key Laboratory of Automotive Safety & Energy, Department of Automotive Engineering, Tsinghua University, Beijing 100084, China*

Correspondence should be addressed to Yibing Li; [liyb@mail.tsinghua.edu.cn](mailto:liyb@mail.tsinghua.edu.cn)

Received 12 March 2016; Revised 19 May 2016; Accepted 9 June 2016

Academic Editor: Majid R. Ayatollahi

Copyright © 2016 Xiaoqing Xu et al. This is an open access article distributed under the Creative Commons Attribution License, which permits unrestricted use, distribution, and reproduction in any medium, provided the original work is properly cited.

Polyvinyl butyral (PVB) laminated glass has been widely used as an important component of mechanical and construction materials. Cracks on PVB laminated glass are rich in impact information, which contribute to its impact resistance design. In this paper, a three-dimensional (3D) numerical simulation model describing PVB laminated glass under impact loading is firstly established and validated qualitatively and quantitatively compared with the corresponding experimental results recorded by the high-speed photography system. In the meantime, the extended finite element method (XFEM) is introduced to analyze the crack propagation mechanism of laminated glass based on dynamic stress intensity factors (DSIFs) and propagations of stress waves. Parametric studies are then carried out to investigate the influence of five critical parameters, that is, plate dimension, crack length, impact energy, glass properties, and PVB properties, on crack propagation characteristics of laminated glass. Results show that the interaction between crack tip and stress waves as well as the propagations of stress waves corresponds to the fluctuations of DSIFs at crack tip. Both the structure and material variables are proven to play a very important role in glass cracking DSIFs and thus govern the crack propagation behavior. Results may provide fundamental explanation to the basic crack propagation mechanism on radial cracks in PVB laminated glass under impact loading conditions, thus to instruct its impact design improvement.

## 1. Introduction

Due to its excellent transparency, formability, and impact resistance, polyvinyl butyral (PVB) laminated glass becomes great potential transparent protective material and has been widely used in both automotive and construction industry. The impact of foreign objects on laminated glass can generate microcracks, which will gradually extend and eventually lead to the failure of laminated glass. Regardless of whether fracture failure occurs, the fragility of glass layer and the good adhesion of PVB interlayer ensure the integrity of sandwiched structure and make the structure have certain energy absorption characteristics and toughness, which effectively improve the security of laminated structure. In order to utilize laminated glass as transparent protective material more effectively, its cracking propagation behavior under impact conditions needs to be comprehensively studied. However, dynamic failure characteristics of laminated glass are very complex; therefore studies on its dynamic cracking propagation characteristics become increasingly necessary.

In recent years, investigations on mechanical properties of PVB laminated glass have been thoroughly conducted, ranging from quasi-static mechanical properties [1–4] to dynamic impact response [4–10]. In general, the impact test in accordance with its impact velocity can be divided into three categories, that is, low-speed drop-weight test [11–13], high-speed impact test with air gun [3, 14, 15], and explosion shock wave impact test [6, 9, 10, 16], where low-speed drop-weight test is one of the most widely used testing methods to evaluate the material critical failure conditions and its fracture mechanism. Lee et al. [17] and Park and Chen [14], respectively, studied the static and dynamic crack propagation behavior in layered glass cross adhesive interlayers. Failure wave was introduced to account for their observations. Zhang et al. [18] and Hu et al. [19] experimentally and numerically studied failure conditions and crack morphologies in brittle plate with a thin polymer backing under various impact velocities and concluded the determining factors to predict its dynamic fracture patterns, that is, elastic properties, fracture energy, and accurate stress

wave tracing model. Meanwhile, Vandenberghe et al. [20] investigated crack patterns in brittle plate upon controlled transverse impact using a global scaling law to predict the number of radial cracks. Also, the coexistence of radial and circumferential cracks was observed. As for a further step, Xu et al. [21] and Chen et al. [22] conducted out-of-plane dynamic loading test on PVB laminated glass based on drop-weight combined with high-speed photography system. Velocity and acceleration time history for both radial and circular cracks were calculated to understand the crack initiation and propagation mechanism. It is found that radial cracks appear earlier than circular ones with higher propagation speed. Furthermore, Chen et al. [23, 24] investigated in-plane crack propagation behavior in PVB laminated glass plate via captured in-plane and interplane cracking process and found that the supported glass layer would always initiate before the loaded layer with the same final radial crack morphologies. The quantity effect of radial cracks on its propagation behavior was also thoroughly investigated.

Numerical simulation attracts more and more attentions to investigate the fracture mechanism of PVB laminated glass for its simplicity and efficiency [5, 8, 25–32]. Bennison et al. [33] studied the stress distribution and fracture sequence in PVB laminated glass upon biaxial flexure loading using finite element method (FEM) and found the relationship between crack initiation and maximum stress location. Meanwhile, Xu and Li [34] numerically investigated the crack evolutions on PVB laminated windshield plate subjected to pedestrian head. It was found that the plastic deformation, radial cracks, and circular cracks were mainly caused by shear stress, compressive stress, and tensile stress, respectively. Furthermore, a series of newly developed numerical simulation methods are increasingly applied to researches on fracture characteristics of PVB laminated glass for their unique advantages in cracking simulation. Xu and Zang [35], Zang et al. [36], and Gao and Zang [37] investigated the impact fracture mechanism of PVB laminated glass on the basis of discrete element method (DEM). Chen et al. [38] numerically investigated the cracking behavior of PVB laminated glass beam under low-velocity impact in the framework of cohesive zone modeling with the glass-ply cracking modeled by extrinsic cohesive model. The propagations of stress waves during cracking process were also primarily analyzed. Based on extended finite element method (XFEM), Xu et al. [39] and Xu et al. [40] established PVB laminated glass plate model subjected to impact loading validated by both radial crack velocity and crack morphology and deeply investigated its radial and circular crack propagation mechanism.

However, as a key parameter to indicate the cracking driving force and interpret the crack propagation behavior in cracking mechanism analysis, dynamic stress intensity factor (DSIF) cannot be easily obtained via experimental methods. The propagations of stress waves during cracking can also have significant effect on cracking response of PVB laminated glass under impact loading. Besides, seldom numerical studies are available in exploring the cracking behavior of PVB laminated glass during out-of-plane impact loading from the perspective of DSIFs and stress waves. It is therefore necessary to investigate the dynamic crack propagation behavior of

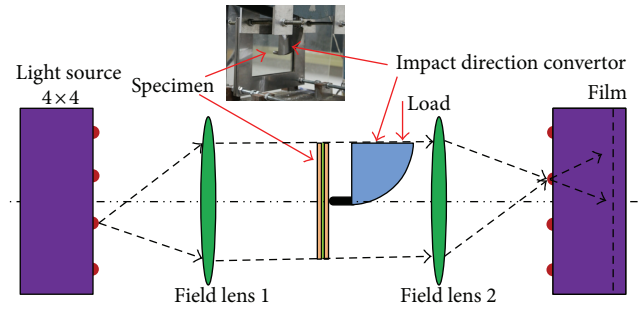


FIGURE 1: The schematic diagram of experimental system combining drop-weight test device with high-speed photography system.

PVB laminated glass on the basis of DSIFs and stress waves. Hence, the numerical model of PVB laminated glass plate with a layered structure is established in this study. The numerical model in simulations with propagation is then validated via the comparison between simulation and experimental results of radial crack propagation process, which are recorded by the high-speed photography system. Further, the time history of DSIFs is calculated in simulations with fixed crack, and the interaction between stress waves and crack tip is also introduced to interpret the relationship between crack propagation behavior and its driving force. Finally, parametric studies on five critical parameters, that is, plate dimension, crack length, impact energy, glass properties, and PVB properties, are conducted based on XFEM, which reveals the laws of crack propagation behavior on PVB laminated glass plates.

## 2. Experimental and Numerical Details

**2.1. Experiment Setup.** The drop-weight device combined with high-speed photography experimental system [21–23] is sketched in Figure 1. The 150 mm × 200 mm rectangular specimen of laminated glass is used in the experiment, which consists of a 0.76 mm PVB interlayer sandwiched by two 2 mm soda-lime glass sheets and is fabricated with the same processing technology of industrial automotive windshield. The drop-weight device is used to apply vertical load via free fall with different height. Meanwhile, the impact direction converter with hemispherical end transfers the vertical load to horizontal load at the specimen center, that is, a load direction perpendicular to specimen plane. The high-speed photography system is adopted to record the real time crack propagation process on glass layer of specimen. The radial crack morphology is recorded on the film and crack propagation speed is calculated [22].

**2.2. Computational Model.** In this study, the three-dimensional (3D) finite element (FE) model consisting of an impactor, a prefabricated crack, and a PVB laminated glass plate is shown in Figure 2. One-quarter of the laminated plate and impactor are modeled to take advantage of the structure symmetry. The cylinder impactor has a mass of

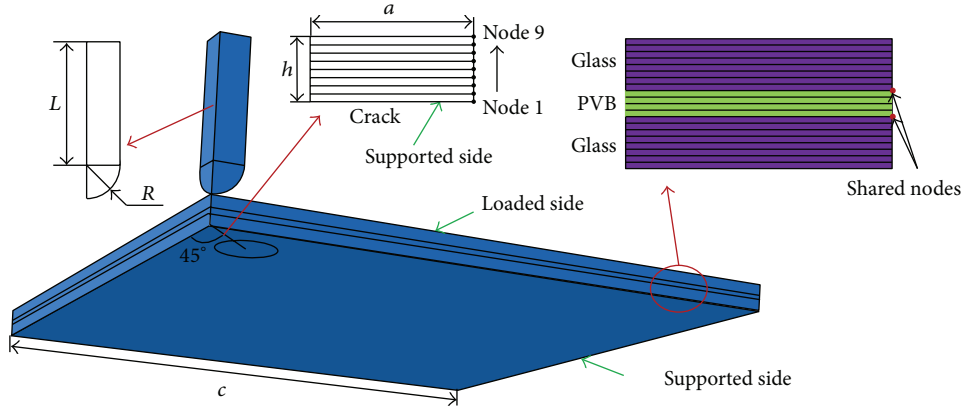


FIGURE 2: The overview of PVB laminated glass computational model subjected to impact loading.

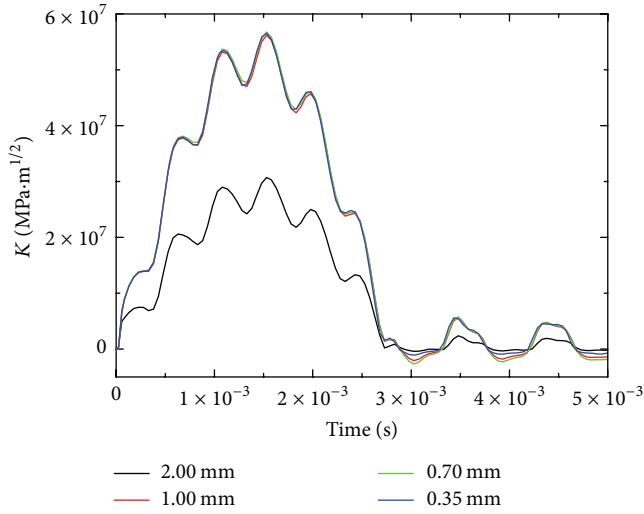


FIGURE 3: The mode I DSIFs of different mesh sizes at node 1 with fixed crack length of 0.02 m and impact speed of 5 m/s.

2 kg via equivalent density with the same mass of experimental impactor. The 2 mm thick crack with the length of  $a$  (shown in Figure 2) is placed at the center of laminated plate in the glass layer of supported side and the angle between crack and structure symmetry line is 45 degrees. In order to eliminate the influence of structural asymmetry, square laminated plate model with dimensions of 200 mm  $\times$  200 mm on plane direction is introduced to study its crack propagation characteristics. The laminated plate model is meshed with 2 mm  $\times$  2 mm (in plane direction) 3D eight-node reduced integration solid (C3D8R) elements. Since stress concentration exists and the stress gradients are very large at crack tip, the crack tip area needs to be meshed with sufficient fine elements to achieve stress and strain accurately. For this purposes, four mesh sizes at crack tip area in plane direction, that is, 0.35 mm  $\times$  0.35 mm, 0.7 mm  $\times$  0.7 mm, 1 mm  $\times$  1 mm, and 2 mm  $\times$  2 mm, are applied to achieve a stable convergence of the computational model. The results are shown in Figure 3, where the mode I DSIFs of node 1 (node 1 to node 9 at crack tip are defined in Figure 2) with

fixed crack length  $a = 0.02$  m under the impact speed of 5 m/s are illustrated. As can be seen, all simulations show the same oscillation frequencies and the mesh refinement has only effect on oscillation amplitudes. Therefore, the configuration of 0.35 mm  $\times$  0.35 mm can be used for further simulations sufficiently. In longitudinal direction, the laminated structure of specimen is modeled with 20 element layers, wherein the outside 8 element layers represent glass layers and the inner 4 element layers stand for the PVB interlayer (shown in Figure 2). Therefore, each layer of the laminated structure has more than three integration points to guarantee the accuracy of calculation and analysis in longitudinal direction.

Clamped boundary conditions of the laminated plate model and frictionless surface-to-surface contact between impactor and specimen are adopted to simulate the real experimental conditions. As typical viscoelastic material, PVB interlayer is simulated with a linear elastic model with a shear modulus  $G = G_0$  and bulk modulus  $K$ , combined with a viscoelastic model. The elastic modulus  $E_{PVB}$  and Poisson's ratio  $\nu$  are described as [42]

$$E_{PVB} = \frac{9KG_0}{3K + G_0}, \quad (1)$$

$$\nu = \frac{3K - 2G_0}{6K + 2G_0},$$

where  $K$  and  $G_0$  are bulk modulus and short time shear modulus of PVB, respectively. The generalized Maxwell model using Prony series with one term is introduced to simulate the viscoelasticity of PVB [42]:

$$G(t) = G_\infty + (G_0 - G_\infty) e^{-\beta t}, \quad (2)$$

where  $G(t)$  is the relaxation modulus which is the function of time  $t$ ,  $G_\infty$  is long time shear modulus, and  $\beta$  is decay factor.

As typical brittle material, glass layers are defined by linear elastic model. Reference parameters of glass layer, PVB interlayer, and impactor are listed in Table 1.

The computational model with the same dimensions of experimental system is set up using a cylinder impactor and a laminated plate model [39] to verify the effectiveness of the

TABLE 1: Basic parameters for numerical model.

	Properties	Reference parameters
Glass layer [40, 41]	Density	2500 kg/m <sup>3</sup>
	Young's modulus	70 GPa
	Poisson's ratio	0.22
	Maximum allowable principal stress	60 MPa
	Energy release rate: $G_{IC}$ , $G_{IIC}$ , $G_{IIIC}$	$G_{IC} = 10 \text{ J/m}^2$ , $G_{IIC} = G_{IIIC} = 50 \text{ J/m}^2$
	Thickness $t_{\text{glass}}$	2 mm
PVB interlayer [41, 42]	Density	1100 kg/m <sup>3</sup>
	Shear modulus: $G_0$ , $G_\infty$	$G_0 = 0.33 \text{ GPa}$ , $G_\infty = 0.69 \times 10^{-3} \text{ GPa}$
	Decay factor $\beta$	12.6 s <sup>-1</sup>
	Bulk modulus $K$	20 GPa
	Thickness $t_{\text{PVB}}$	0.76 mm
Impactor	Mass	2 kg
	Young's modulus	207 GPa
	Poisson's ratio	0.22
	Length $L$	20 mm
	Radius $R$	5 mm

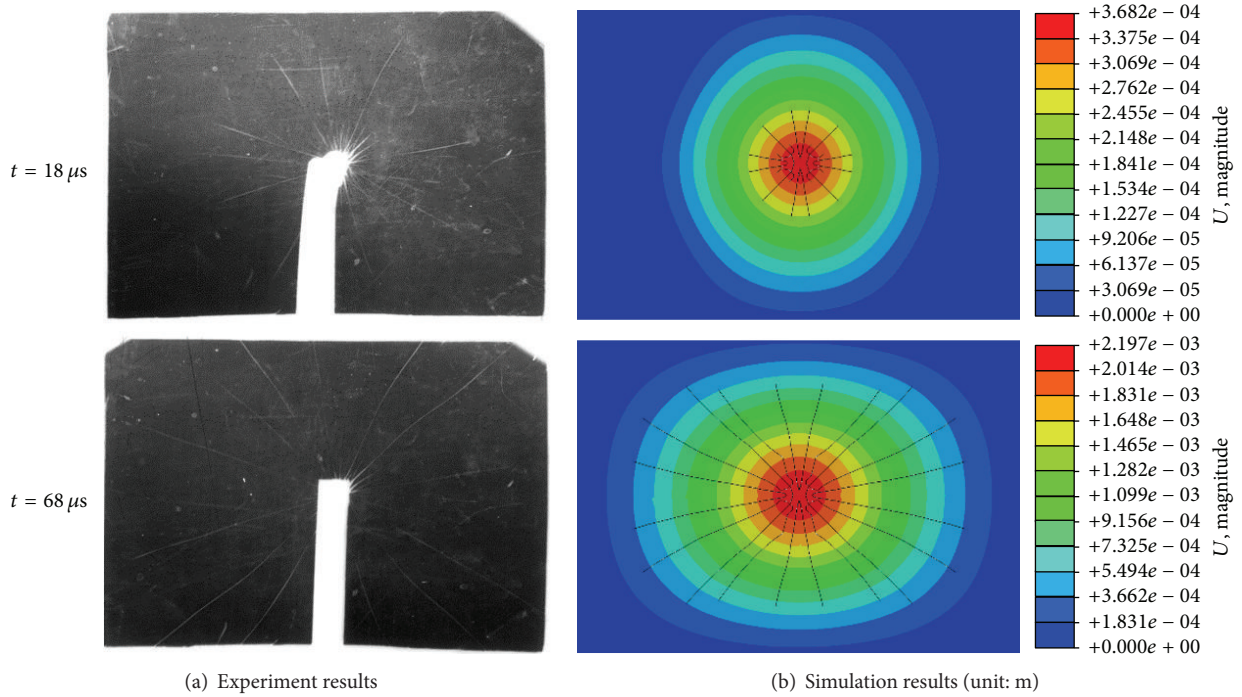


FIGURE 4: Qualitative verification: comparison of radial crack morphologies between simulation results and experimental results.

abovementioned model. The experimental system model is then verified in simulations with propagation via qualitative method (radial crack morphology) and quantitative method (crack propagation velocity) shown in Figures 4 and 5, respectively. As can be seen from Figure 4, a total of 22 radial cracks exist in experimental images and most of them have propagated to the border of the specimen shown in Figure 4(a). In comparison, 20 radial cracks in all have propagated close to the border in simulation images shown in Figure 4(b). Thus, both the crack propagation process and

the morphology of cracks in simulation agree well with the experimental results. Figure 5 shows the comparison of crack velocity time history curves between experiment and simulation results. As can be observed, the cracks propagation time history in simulation is recorded from the increment of the original crack, for initial flaws are preembedded in the model. Another difference between the experimental and simulation results is that the gradient of the descending stage of the velocity curves in simulation is smaller than that in experiment. The responsible reason should be the

rubber pad used between the mental clamp and glass sheet to avoid possible damage during screwing in experiment. The rebound velocity in simulation is higher in simulation where no cushion pad is provided. So the peak value as well as the time history of the simulation results is in good agreement with the experimental results. The computational results are in good agreement with the corresponding experimental results from both qualitative perspective and quantitative perspective. Therefore, a reliable FE model with fairly high quality is established and can be adopted for further studies on crack behavior of PVB laminated glass.

**2.3. Fundamentals of XFEM.** The extended finite element method XFEM, which is a numerical technique based on generalized finite element method and the partition of unity method, extends the piecewise polynomial function space of conventional finite element methods with extra enrichment functions. XFEM does not need to be updated to track the crack path and can obtain accurate solution with coarse mesh [43, 44].

The displacement interpolation of XFEM is described as below [43]:

$$\begin{aligned} \mathbf{u}^h(\mathbf{x}) &= \sum_{I \in N_\Gamma} N_I(\mathbf{x}) \left[ \mathbf{u}_I + H(\mathbf{x}) \mathbf{a}_I + \sum_{\alpha=1}^4 \sum_{J \in N_\Lambda} F_\alpha(\mathbf{x}) \mathbf{b}_J^\alpha \right], \quad (3) \end{aligned}$$

where  $N_\Gamma$  is the number of nodes in elements cut by crack;  $N_\Lambda$  is the number of nodes in elements with crack tip;  $N_I(\mathbf{x})$  are the conventional shape functions;  $\mathbf{u}_I$  are the nodal DOFs for conventional shape functions;  $\mathbf{a}_I$  and  $\mathbf{b}_J^\alpha$  are the nodal DOFs associated with the Heaviside function  $H(\mathbf{x})$ , with the value above the crack and  $-1$  below the crack. The crack tip enrichment functions  $F_\alpha(\mathbf{x})$  are expressed as [43]

$$\begin{aligned} [F_\alpha(\mathbf{x}), \alpha = 1 \sim 4] &= \left[ \sqrt{r} \sin \frac{\theta}{2}, \sqrt{r} \cos \frac{\theta}{2}, \sqrt{r} \sin \theta \right. \\ &\left. \cdot \sin \frac{\theta}{2}, \sqrt{r} \sin \theta \cos \frac{\theta}{2} \right], \quad (4) \end{aligned}$$

where  $\mathbf{x}$  is an integration point and  $(r, \theta)$  denote the coordinate values from a polar coordinate system located at the crack tip.

Details of XFEM can be found in [43–45].

**2.4. Calculation of Dynamic Stress Intensity Factors.** In linear fracture mechanics, for example, soda-lime glass, the dynamic stress intensity factors ( $K_I^{\text{Dyn}}$ ,  $K_{II}^{\text{Dyn}}$ ,  $K_{III}^{\text{Dyn}}$ ) are widely used to characterize the stress and displacement fields near the crack tip, where  $K_I^{\text{Dyn}}$ ,  $K_{II}^{\text{Dyn}}$ , and  $K_{III}^{\text{Dyn}}$  are mode I, II, and III DSIFs. DSIFs relevant to energy release rate ( $J$ -integral) can be described as

$$J = \frac{1}{8\pi} \bar{\mathbf{K}}^T \cdot \bar{\mathbf{B}}^{-1} \cdot \bar{\mathbf{K}}, \quad (5)$$

where  $\bar{\mathbf{K}} = [K_I^{\text{Dyn}}, K_{II}^{\text{Dyn}}, K_{III}^{\text{Dyn}}]^T$  is SIF vector and  $\bar{\mathbf{B}}$  is the prelogarithmic energy factor matrix, which is diagonal for

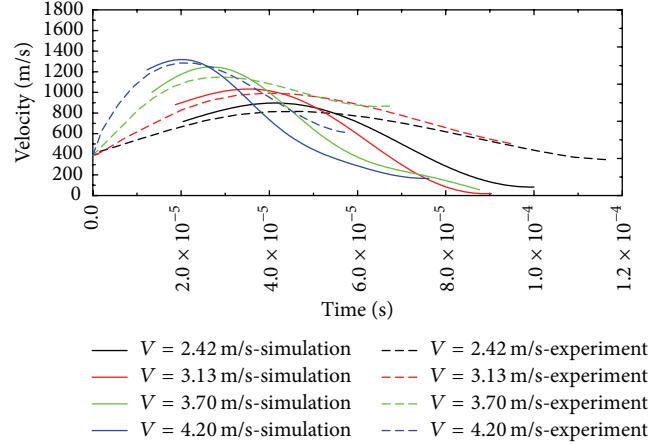


FIGURE 5: Quantitative verification: comparison of crack propagation velocities between simulation results and experimental results.

homogeneous and isotropic materials. Therefore the equation can be simplified to

$$J = \frac{1}{E^*} \left[ \left( K_I^{\text{Dyn}} \right)^2 + \left( K_{II}^{\text{Dyn}} \right)^2 \right] + \frac{1}{2G} \left( K_{III}^{\text{Dyn}} \right)^2, \quad (6)$$

where  $E^* = E$  for plane stress and  $E^* = E/(1 - \nu^2)$  for plane strain.

The interaction integral method [46] is introduced to calculate DSIFs for cracks under mixed-mode loading, instead of according to a known  $J$ -integral. The  $J$ -integral can be described as

$$\begin{aligned} J &= \frac{1}{8\pi} \left[ K_I^{\text{Dyn}} B_{11}^{-1} K_I^{\text{Dyn}} + 2 K_I^{\text{Dyn}} B_{12}^{-1} K_{II}^{\text{Dyn}} \right. \\ &\left. + 2 K_I^{\text{Dyn}} B_{13}^{-1} K_{III}^{\text{Dyn}} + \left( \text{terms not involving } K_I^{\text{Dyn}} \right) \right]. \quad (7) \end{aligned}$$

With regard to an auxiliary pure mode I crack tip field, the DSIF  $k_I^{\text{Dyn}}$  can be defined as

$$J_{\text{aux}}^I = \frac{1}{8\pi} k_I^{\text{Dyn}} B_{11}^{-1} k_I^{\text{Dyn}}. \quad (8)$$

Then overlay the auxiliary field on the actual field yields

$$\begin{aligned} J_{\text{tot}}^I &= \frac{1}{8\pi} \left[ \left( K_I^{\text{Dyn}} + k_I^{\text{Dyn}} \right) B_{11}^{-1} \left( K_I^{\text{Dyn}} + k_I^{\text{Dyn}} \right) \right. \\ &+ 2 \left( K_I^{\text{Dyn}} + k_I^{\text{Dyn}} \right) B_{12}^{-1} K_{II}^{\text{Dyn}} \\ &+ 2 \left( K_I^{\text{Dyn}} + k_I^{\text{Dyn}} \right) B_{13}^{-1} K_{III}^{\text{Dyn}} \\ &\left. + \left( \text{terms not involving } K_I^{\text{Dyn}} \text{ or } k_I^{\text{Dyn}} \right) \right]. \quad (9) \end{aligned}$$

Since

$$\begin{aligned} &\left( \text{terms not involving } K_I^{\text{Dyn}} \right) \Big|_J \\ &= \left( \text{terms not involving } K_I^{\text{Dyn}} \text{ or } k_I^{\text{Dyn}} \right) \Big|_{J_{\text{tot}}^I} \quad (10) \end{aligned}$$

the interaction integral for mode I field can be expressed as

$$\begin{aligned} J_{\text{int}}^{\text{I}} &= J_{\text{tot}}^{\text{I}} - J - J_{\text{aux}}^{\text{I}} \\ &= \frac{k_{\text{I}}^{\text{Dyn}}}{4\pi} \left( B_{11}^{-1} K_{\text{I}}^{\text{Dyn}} + B_{12}^{-1} K_{\text{II}}^{\text{Dyn}} + B_{13}^{-1} K_{\text{III}}^{\text{Dyn}} \right). \end{aligned} \quad (11)$$

For mode II and mode III, similar results can be obtained:

$$\begin{aligned} J_{\text{int}}^{\text{II}} &= \frac{k_{\text{II}}^{\text{Dyn}}}{4\pi} \left( B_{21}^{-1} K_{\text{I}}^{\text{Dyn}} + B_{22}^{-1} K_{\text{II}}^{\text{Dyn}} + B_{23}^{-1} K_{\text{III}}^{\text{Dyn}} \right) \\ J_{\text{int}}^{\text{III}} &= \frac{k_{\text{III}}^{\text{Dyn}}}{4\pi} \left( B_{31}^{-1} K_{\text{I}}^{\text{Dyn}} + B_{32}^{-1} K_{\text{II}}^{\text{Dyn}} + B_{33}^{-1} K_{\text{III}}^{\text{Dyn}} \right). \end{aligned} \quad (12)$$

**2.5. Crack Propagation Criteria.** In static case, the open mode crack propagation criteria are generally expressed as  $K_{\text{I}} \geq K_{\text{IC}}$ , where  $K_{\text{I}}$  and  $K_{\text{IC}}$  (for glass:  $K_{\text{IC}} \approx 0.7 \text{ MP}\sqrt{\text{m}}$ ) are static stress intensity factor and static fracture toughness, respectively. Similarly, the dynamic open mode crack propagation criteria are defined as  $K_{\text{I}}^{\text{Dyn}}(t) \geq K_{\text{IC}}^{\text{Dyn}}$  [47], where  $K_{\text{I}}^{\text{Dyn}}(t)$  related to time  $t$  is DSIF and  $K_{\text{IC}}^{\text{Dyn}}$  associated with strain rate is dynamic fracture toughness.  $K_{\text{I}}^{\text{Dyn}}(t)$  is determined by experiments, while  $K_{\text{IC}}^{\text{Dyn}}$  is determined through dynamic structural analysis. Since the cracks are generated in linear elastic glass layer, the influence of loading rate on  $K_{\text{IC}}^{\text{Dyn}}$  can be neglected within the scope of our discussion impact velocity [48, 49]. Therefore, the rate sensitivity of  $K_{\text{IC}}^{\text{Dyn}}$  for glass layer can be ignored in the analysis of laminated glass fracture mechanism, that is,  $K_{\text{IC}}^{\text{Dyn}} \approx K_{\text{IC}} \approx 0.7 \text{ MP}\sqrt{\text{m}}$ .

**2.6. Cracking Propagation Direction.** The maximum tangential stress criterion is adopted to compute the cracking propagation direction, where  $K_{\text{III}}^{\text{Dyn}}$  is not taken into consideration in these criteria. In the case of  $\partial\sigma_{\theta\theta}/\partial\theta = 0$  (or  $\tau_{r\theta} = 0$ , where  $\sigma$  and  $\tau$  are normal stress and tangential stress, resp., and  $r$  and  $\theta$  are polar coordinates at the crack tip in a plane perpendicular to the crack plane), the crack propagation angle relative to the crack plane can be obtained [46]:

$$\begin{aligned} \hat{\theta} \\ = \cos^{-1} \left( \frac{3(K_{\text{II}}^{\text{Dyn}})^2 + \sqrt{(K_{\text{I}}^{\text{Dyn}})^4 + 8(K_{\text{I}}^{\text{Dyn}})^2(K_{\text{II}}^{\text{Dyn}})^2}}{(K_{\text{I}}^{\text{Dyn}})^2 + 9(K_{\text{II}}^{\text{Dyn}})^2} \right), \end{aligned} \quad (13)$$

where  $\hat{\theta} = 0$  indicates the crack propagation in a straight direction.  $\hat{\theta} > 0$  corresponds to  $K_{\text{II}}^{\text{Dyn}} < 0$ , while  $\hat{\theta} < 0$  stands for  $K_{\text{II}}^{\text{Dyn}} > 0$ .

**2.7. Simulations with Fixed Crack.** According to our previous experimental studies [23], there are three types of cracks in PVB laminated plate under impact loading, that is, radial cracks in supported side, radial cracks in loaded side, and circumferential cracks in supported side, where supported side and loaded side are defined in Figure 2. Besides, radial cracks

appear before circumferential cracks, while radial cracks in supported side are generated earlier than radial cracks in loaded side and radial cracks in both sides overlap completely. Therefore, the study on radial cracking propagation behavior in supported side is fairly important for investigating the fracture properties of PVB laminated glass.

Then, a series of numerical simulations on dynamic response of laminated glass with a fixed crack are conducted under different impact conditions using commercial finite element software ABAQUS. In our simulations, the crack is specified to be stationary and the material in crack tip should be in pristine condition to predict the crack propagation. Five structure and material variables, that is, plate dimension, crack length, impact energy, glass properties, and PVB properties, are introduced to conduct parametric studies in Section 4, and the detailed variable settings in parametric study are listed in Table 2 with other parameters kept at their reference values shown in Table 1.

### 3. Analysis of the Time History of DSIFs

In the condition of dynamic fracture, DSIFs are functions of time and the in-depth analysis of the time history of DSIFs helps to fully understand the crack propagation characteristics. Figure 6(a) shows the velocity and acceleration time history of impactor with the initial velocity of 5 m/s, and the corresponding mode I, II, and III DSIFs of node 1 at crack tip are shown in Figure 6(b). It can be seen that both the acceleration curve and DSIF curves exhibit regular fluctuations in the same law before  $3 \times 10^{-3}$  s, while the acceleration curve almost has no fluctuation and DSIF curves still have slight regular fluctuations after  $3 \times 10^{-3}$  s. Since the impactor has been away from the plate after  $3 \times 10^{-3}$  s, the existence of stress waves leads to the fluctuations of DSIF curves in the entire time course and the crest appears when crack tip interacts with stress waves, indicating that the interaction between crack tip and stress waves accounts for the DSIFs' changes. Therefore, the time of interaction between the crack tip and stress waves corresponds to the fluctuation crests of DSIFs.

Since  $|K_{\text{I}}^{\text{Dyn}}|$  is much larger than  $|K_{\text{II}}^{\text{Dyn}}|$  and  $|K_{\text{III}}^{\text{Dyn}}|$  (Figure 6), the crack tip field is mixed-mode crack tip field which mode I is in dominance [21, 22], that is, the mixed-mode DSIF  $K^{\text{Dyn}} \approx K_{\text{I}}^{\text{Dyn}}$ , and mode I DSIF can be introduced to represent mixed-mode DSIF. Figure 7 shows the mode I DSIF time history of node 1 to node 8 at crack tip under the impact velocity of 5 m/s (Figure 7(b) shows the data before  $5 \times 10^{-5}$  s). As can be seen, mode I DSIFs of node 1 to node 8 at crack tip begin to rise rapidly after a time lag which is defined as lag time, then fluctuate in the same regularity under the impact stress waves, and finally fluctuate slightly with the crest decreasing under the residual stress waves, so the entire process can be divided into three stages: lag stage, interaction stage, and residual stage. The propagation process of stress waves is introduced to explain this phenomenon (shown in Figure 8): the impact generates the compressive stress waves, which propagate from the loaded side to the supported side in the thickness direction.

TABLE 2: The detailed variable settings in parametric numerical study.

Numerical variables		Reference parameters
Plate dimension (m × m)		0.05 × 0.05, 0.1 × 0.1, 0.2 × 0.2
Crack length (m)		0.01, 0.02, 0.04
Impact energy	Impact velocity (m/s)	2, 5, 8, 10, 15, 20
	Impact mass (kg)	0.32, 2, 8
Glass properties	Young's modulus (GPa)	7, 70, 700
	Density (kg/m <sup>3</sup> )	250, 2500, 25000
PVB properties	Young's modulus	0.1E <sub>PVB</sub> , E <sub>PVB</sub> , 10E <sub>PVB</sub>
	Density (kg/m <sup>3</sup> )	110, 1100, 11000
	Shear modulus ratio	2.1 × 10 <sup>-4</sup> , 2.1 × 10 <sup>-3</sup> , 2.1 × 10 <sup>-2</sup>
	Delay factor (s <sup>-1</sup> )	0.126, 12.6, 1260

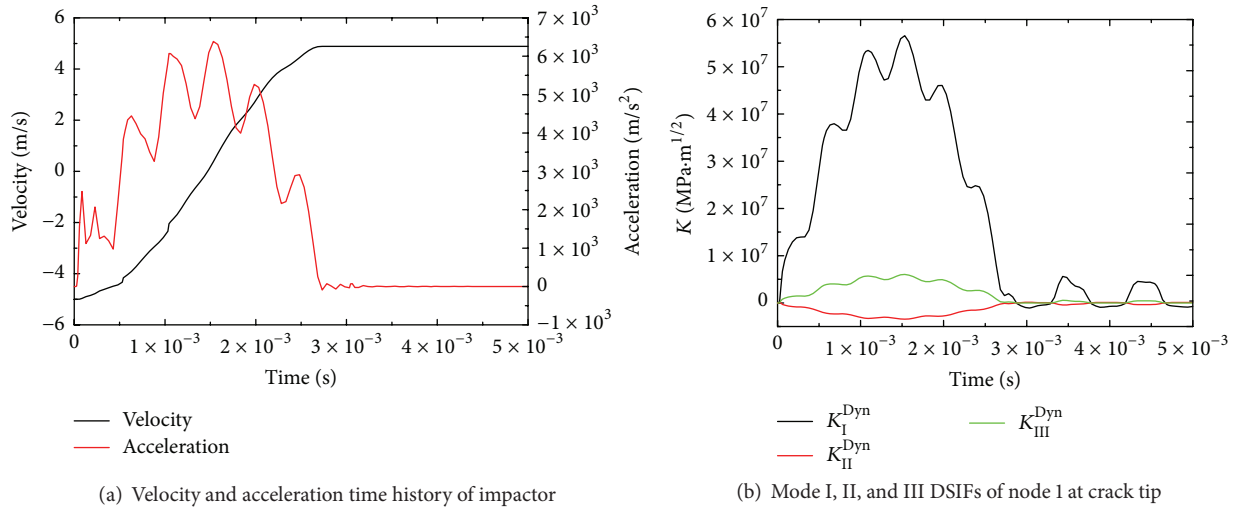


FIGURE 6: Simulation results with the impact velocity of 5 m/s and crack length of 0.02 m.

Then the compressive stress waves reflect from the supported side (free surface) into tension stress waves, which consist of shear wave, longitudinal wave, and Rayleigh wave. The tension stress waves further propagate to the boundaries and reflect to the crack tip (shear wave and longitudinal wave through glass layer, while Rayleigh wave through free surface of supported side), which results in the crests of DSIFs. Besides, mode I DSIFs of node 1 to node 8 decrease one by one for the weakening of reflected tension stress waves during propagation, while there is almost no difference in peak times of these nodes for the extremely high propagation velocity of stress waves. Therefore, the round-trip propagation of tension stress waves leads to the fluctuations of DSIFs.

The velocities of involved stress waves are expressed as follows [50]:

$$\begin{aligned}
 c_l &= \sqrt{\frac{E(1-\nu)}{(1-2\nu)(1+\nu)\rho}} \\
 c_s &= \sqrt{\frac{E}{2(1+\nu)\rho}} \\
 c_R &\approx 0.495c_l,
 \end{aligned} \tag{14}$$

where  $c_l$ ,  $c_s$ , and  $c_R$  stand for the velocities of longitudinal wave, shear wave, and Rayleigh wave, respectively, besides  $c_l = \max\{c_l, c_s, c_R\}$ ;  $E$ ,  $\nu$ , and  $\rho$  represent Young's modulus, Poisson's ratio, and density, respectively. The layer interfaces can cause large amounts of stress wave reflection and further dramatically delay the stress wave propagation. Similar delays have also been discovered in other experimental researches [14]. Therefore, the lag time of DSIF, which is the shortest propagation time of compressive stress waves from loaded side to supported side, can be expressed as

$$\begin{aligned}
 t_l &\approx 2 \cdot t_{\text{Glass}} + t_{\text{PVB}} + 2 \cdot t_{\text{Interface}} \\
 &= 2 \cdot \frac{d}{c_l} \Big|_{\text{Glass}} + \frac{d}{c_l} \Big|_{\text{PVB}} + 2 \cdot t_{\text{Interface}},
 \end{aligned} \tag{15}$$

where  $t_{\text{Glass}}$ ,  $t_{\text{PVB}}$ , and  $t_{\text{Interface}}$  represent propagation time of longitudinal wave through glass layers, PVB interlayer, and layer interfaces, respectively. Analogously, the interval of propagation time between node 1 and node 8 should be

$$t_{\text{Interval}} \approx \frac{d}{c_l} \Big|_{\text{Glass}} \approx 3.54 \times 10^{-7} \text{ s}. \tag{16}$$

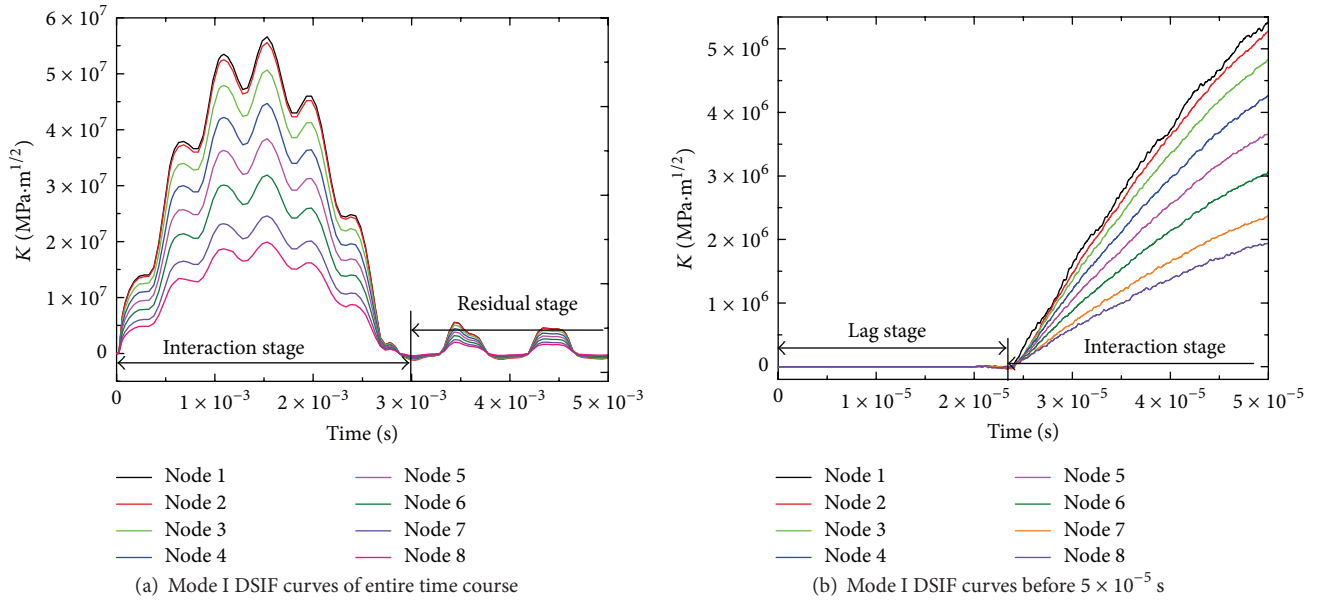


FIGURE 7: The mode I DSIF time history of node 1 to node 8 at crack tip with the impact velocity of 5 m/s and crack length of 0.02 m.

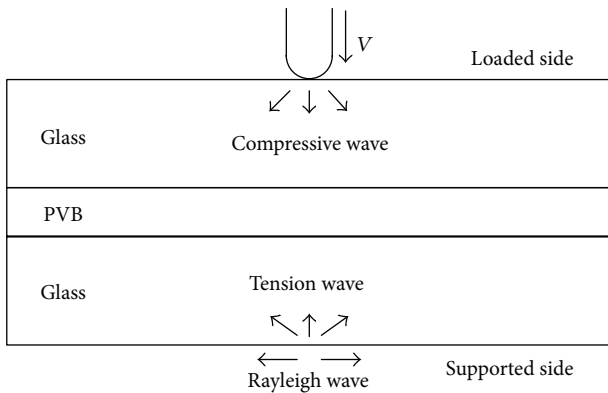


FIGURE 8: The propagation process of stress waves.

Furthermore, the time when DSIF increases to dynamic fracture toughness with the stress waves accumulation, that is,  $K^{\text{D}^{\text{yn}}} \approx K_{\text{IC}}^{\text{D}^{\text{yn}}} \approx K_{\text{IC}} \approx 0.7 \text{ MP}\sqrt{\text{m}}$ , is considered as the simulated propagation time. The simulated crack propagation times of node 1 to node 8 and the corresponding linear fitting results are illustrated in Figure 9; then the simulated propagation time interval between node 1 and node 8 can be calculated as  $4.55 \times 10^{-7}$  s which is in good agreement with theoretical calculation.

According to the stress wave propagation theory, crack propagation firstly occurs at node 1, so parametric studies on crack propagation characteristics focus on mode I DSIF at node 1 in Section 4.

#### 4. Discussions

4.1. Effects of Plate Dimension. Three different plate dimensions ( $0.05 \text{ m} \times 0.05 \text{ m}$ ,  $0.1 \text{ m} \times 0.1 \text{ m}$ , and  $0.2 \text{ m} \times 0.2 \text{ m}$ )

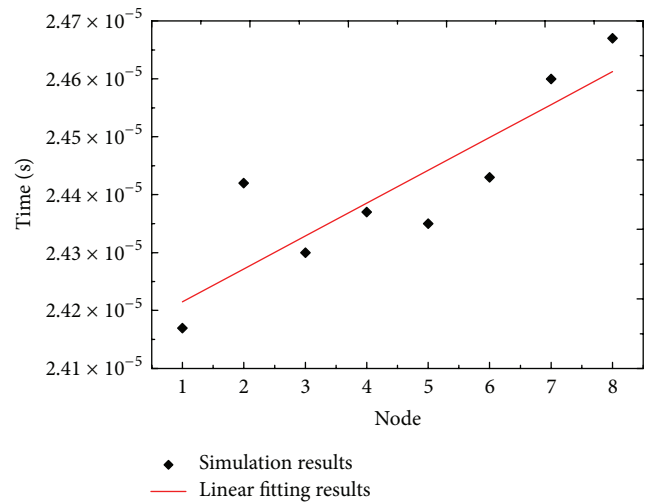


FIGURE 9: The simulated crack propagation times of node 1 to node 8 and the corresponding linear fitting curve.

in plane direction are considered to study the dimension effect on cracking propagation characteristics of glass layer. Figure 10 gives the effect of plate dimension on mode I DSIF of node 1. As can be seen, the interaction stage is getting longer and the peak DSIF would be smaller with the increase of plate size under the same impact energy due to the decrease of structure stiffness. The time that the stress wave propagation needed from the crack tip to the plate borders and return to the crack tip becomes longer due to the increase of plate edge length; therefore the time interval of DSIF peaks, that is, fluctuation cycle, increases with the increase of plate size which is fully consistent with the simulation results as shown in Figure 10.

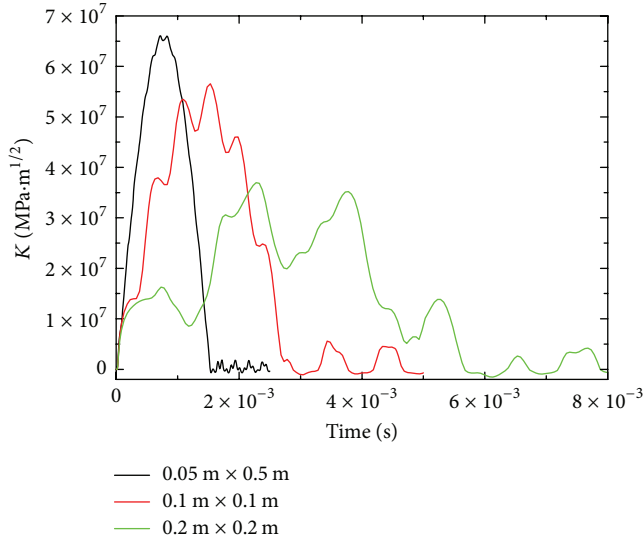


FIGURE 10: Mode I DSIF curves at node 1 of different plate dimensions with the impact velocity of 5 m/s and crack length of 0.02 m.

**4.2. Effects of Crack Length.** Figure 11 shows the mode I DSIF curves at node 1 with different fixed crack lengths (0.01 m, 0.02 m, and 0.04 m) under the impact velocity of 5 m/s. As can be seen, with the increase of fixed crack length, the lag time increases proportionally (Figure 11(b)) and the peak times are postponed with fluctuation frequency (reciprocal of fluctuation cycle) changing slightly (Figure 11(a)). Since the pre-crack length increases, the stress wave propagation path from impact point to crack tip increases, which leads to the increase of lag time, and the propagation path from crack tip to proximal border decreases, while it increases to distal border, which results in the changes of fluctuation frequency. In addition, the DSIF decreases with the increase of pre-crack length, due to the increase of propagation path from impact point to crack tip which leads to the increased stress wave weakening.

**4.3. Effects of Impact Energy.** Two aspects, that is, impact velocity and impact mass, are introduced to investigate the influence of impact energy on cracking propagation characteristics of glass layer. The mode I DSIFs of node 1 with different impact velocities and impact masses are given in Figures 12(a) and 12(b), respectively. As shown in Figure 12, both the increase of impact velocity and impact mass lead to the increase of peak mode I DSIF at all stages and almost have no effect on fluctuation frequency of DSIF curve. Besides, the interaction time between impactor and plate increases with the increase of impact mass but is not affected by impact velocity. Since the acceleration of impactor is mainly affected by impact velocity, the rebound time of impactor increases with the impact mass and almost has no change with impact speed. In summary, the increase of impact energy results in the increase of stress wave accumulation, that is, peak DSIF, while it has little influence on stress wave propagation velocity, that is, fluctuation frequency.

**4.4. Effects of Glass Properties.** In static case, stress intensity factors have nothing to do with material's Young's modulus and density. However, under impact loading conditions, the stress wave accumulation at crack tip leads to the crack propagation; thus stress wave propagation speed plays a critical role in crack propagation characteristics. As can be seen from (14), longitudinal wave, shear wave, and Rayleigh wave velocities are all functions of Young's modulus and density. Besides, stress wave velocities are proportional to Young's modulus and inversely proportional to density.

Figures 13(a) and 13(b) show the effects of glass Young's modulus  $E_{\text{Glass}}$  and density  $\rho_{\text{Glass}}$  on mode I DSIF at node 1. As can be observed, larger Young's modulus corresponds to the shorter interaction stage and larger peak DSIF owing to the increase of structure stiffness, while density changes have little effect on the length of interaction stage and peak DSIF with structure stiffness unchanged. Besides, the lag time increases and the peak times are postponed, for the decrease of Young's modulus or the increase of density leads to the decrease of stress wave velocities. Furthermore, the stress wave propagation time becomes longer with the decrease of Young's modulus or the increase of density; therefore the fluctuation frequency increases with the increase of Young's modulus or the decrease of density, which agrees well with the simulation results shown in Figure 13.

**4.5. Effects of PVB Properties.** As longitudinal boundaries of cracks in glass layers, PVB interlayer has an important influence on DSIFs of glass layer. Figures 14(a) and 14(b) show the effects of PVB Young's modulus  $E_{\text{PVB}}$  and density  $\rho_{\text{PVB}}$  on mode I DSIF curves at node 1. As can be seen, the interaction stage and peak DSIF decrease with the increase of PVB Young's modulus due to the increase of structure stiffness, while density changes have little effect on the length of interaction stage and peak DSIF with structure stiffness unchanged. Moreover, the fluctuation frequency increases with the increase PVB Young's modulus or the decrease of PVB density. According to (14), the stress wave propagation velocities in glass layer are far higher than that in PVB interlayer; thus the existence of PVB interlayer has an inhibiting effect on the stress wave propagation in glass layer, which leads to the increase of stress wave propagation time in glass layer.

The viscosity  $\eta$  in the one-term generalized Maxwell model can be expressed as

$$\eta = (G_0 - G_\infty) \tau = \frac{(G_0 - G_\infty)}{\beta}. \quad (17)$$

As seen, shear modulus ratio  $G_\infty/G_0$  and delay factor  $\beta$  are two main viscosity factors, which are inversely proportional to viscosity. Figures 14(c) and 14(d) give the effects of shear modulus ratio and delay factor on mode I DSIF curves at node 1. One may draw conclusion that the interaction stage, peak DSIF, and fluctuation cycle decrease with the increase of PVB viscosity. Besides, shear modulus ratio has a greater influence than delay factor. The relaxation occurs in PVB interlayer during the impact, which leads to the decrease of PVB modulus. PVB modulus decreases faster with the increase

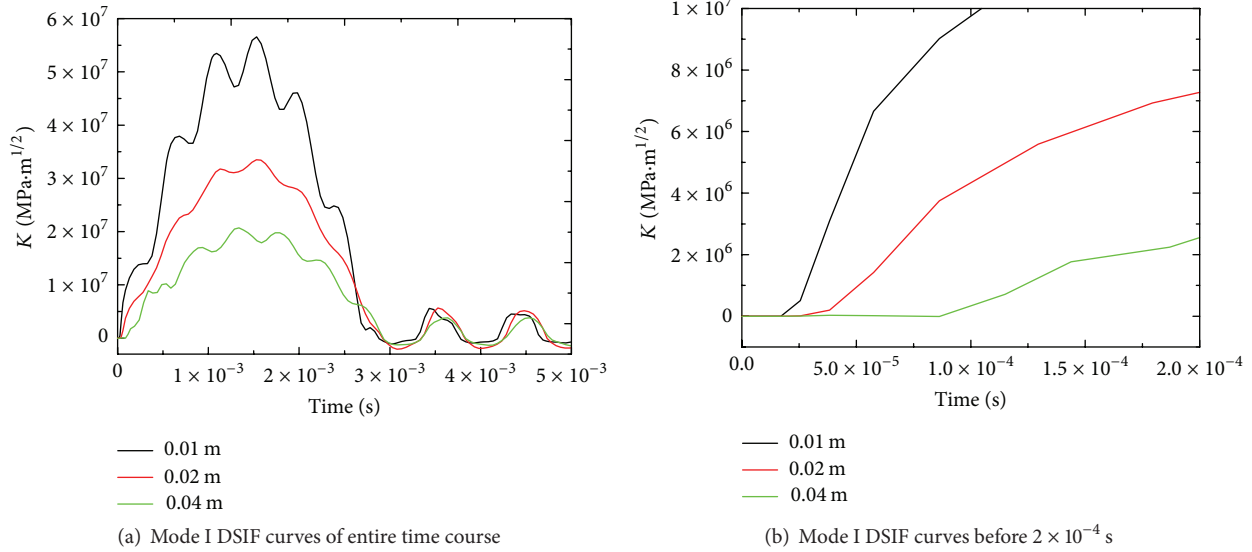


FIGURE 11: Mode I DSIF curves at node 1 with different fixed crack lengths under the impact velocity of 5 m/s.

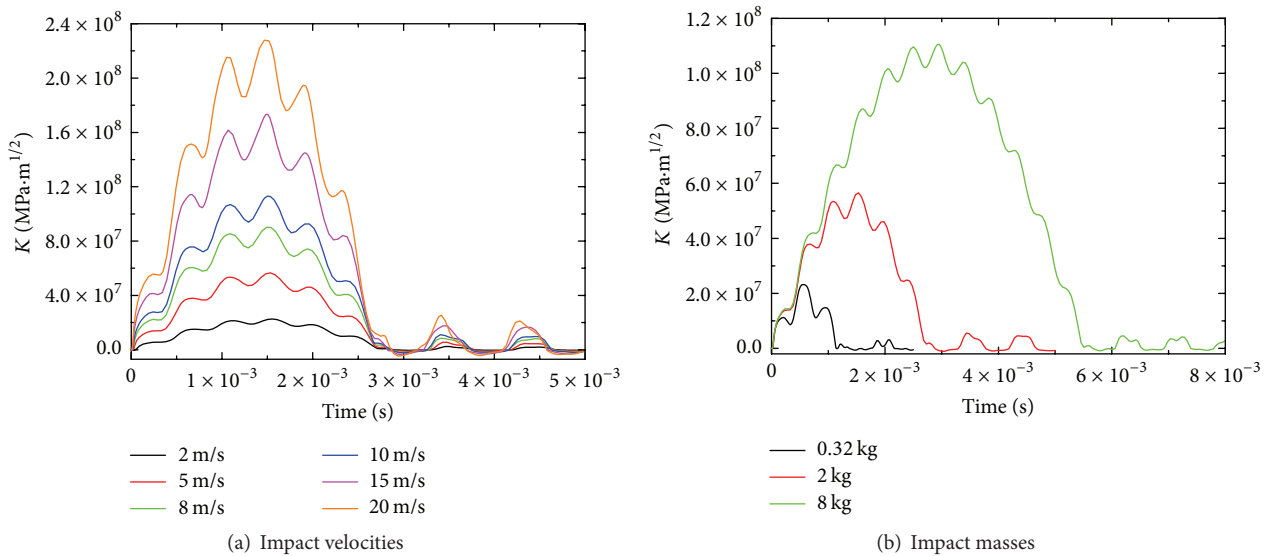


FIGURE 12: Mode I DSIF curves at node 1 with crack length of 0.02 m under different impact energy.

of viscosity, which explains the viscosity effect. However, the stress wave propagation time is far less than the PVB relaxation time and only a small amount of relaxation occurs during the impact. Therefore, the influence of delay factor on DSIF is less obvious than shear modulus ratio.

### 5. Concluding Remarks

In this paper, the crack propagation characteristics of PVB laminated glass under low-speed impact are investigated in the framework of XFEM. A PVB laminated glass 3D model is proposed, which has been qualitatively and quantitatively validated via comparing with the experimental results captured by high-speed photography system. The verified numerical

model with fixed crack is then used to systematically investigate the crack propagation behavior. The time history of brittle DSIFs as well as the propagations of stress waves is derived to interpret the crack propagation mechanism.

Further, five critical structure and material variables, that is, plate dimension, crack length, impact energy, glass properties, and PVB properties, are introduced to conduct parametric studies. It is found that the interaction between the crack tip and stress waves and the round-trip propagations of tension stress waves lead to the fluctuations of DSIFs, which corresponds to the influence of plate dimension and crack length. The impact energy and glass properties result in the changes of DSIF peak values and fluctuation frequencies, respectively. As longitudinal boundaries of cracks in glass

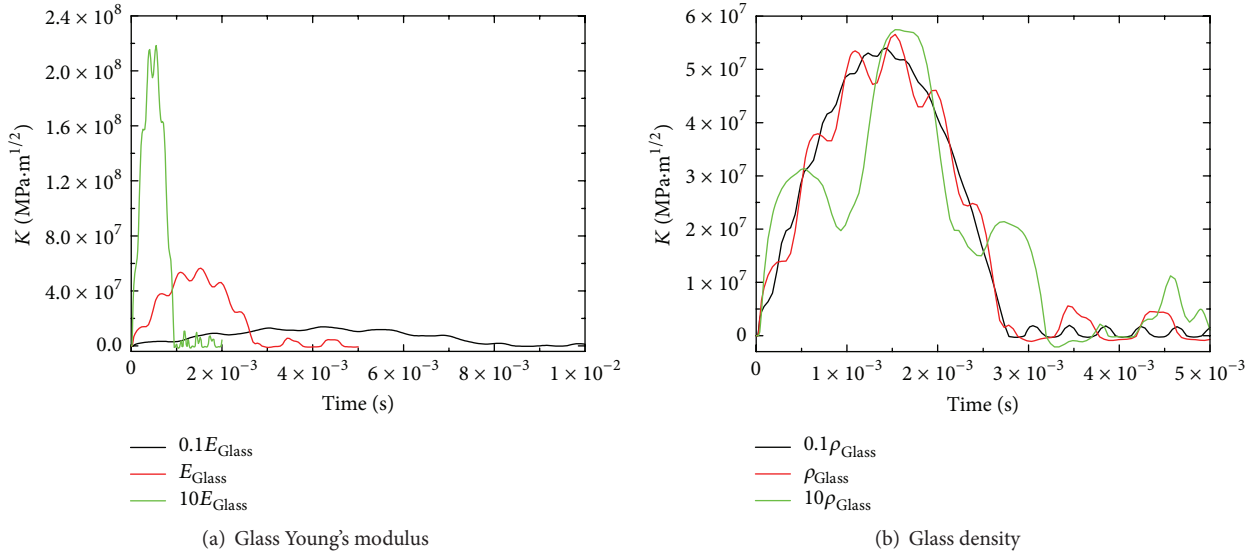


FIGURE 13: Mode I DSIF at node 1 of different glass properties with the impact velocity of 5 m/s and crack length of 0.02 m.

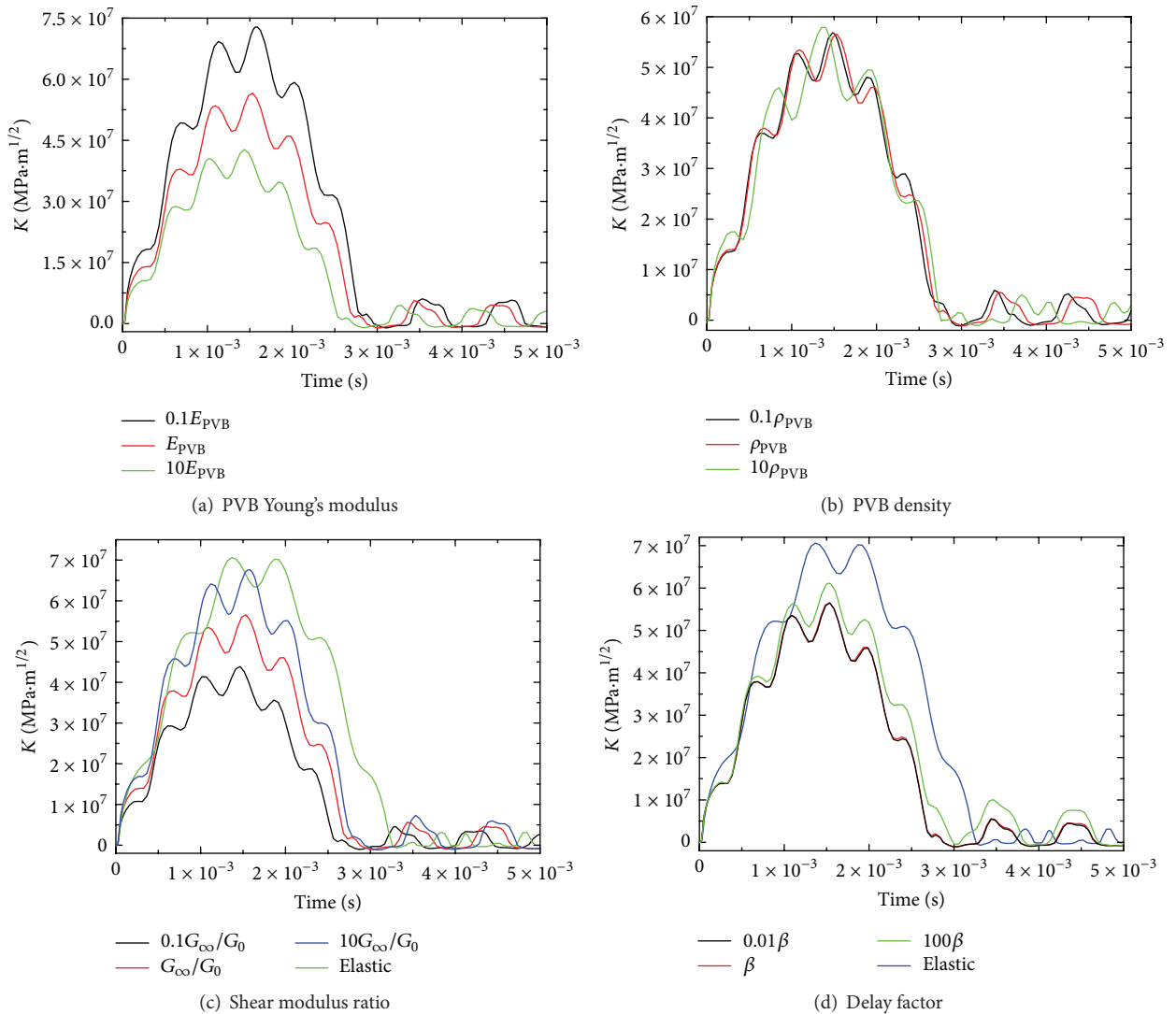


FIGURE 14: Mode I DSIF at node 1 of different PVB properties with the impact velocity of 5 m/s and crack length of 0.02 m.

layers, PVB interlayer has an important influence on DSIFs of glass layer.

This research may provide basic crack propagation laws for researches on cracking mechanism of PVB laminated glass under impact loading conditions in the future.

## Competing Interests

The authors declare that they have no competing interests.

## Acknowledgments

The work is supported by the National Natural Science Foundation of China (11372164 and 11102099) and Tsinghua University under Grants nos. 20121080050 and 20132001016.

## References

- [1] J. Belis, J. Depauw, D. Callewaert, D. Delincé, and R. Van Impe, "Failure mechanisms and residual capacity of annealed glass/SGP laminated beams at room temperature," *Engineering Failure Analysis*, vol. 16, no. 6, pp. 1866–1875, 2009.
- [2] C. V. G. Vallabhan, Y. C. Das, M. Magdi, M. Asik, and J. R. Bailey, "Analysis of laminated glass units," *Journal of Structural Engineering*, vol. 119, no. 5, pp. 1572–1585, 1993.
- [3] J. Xu, Y. Li, B. Liu, M. Zhu, and D. Ge, "Experimental study on mechanical behavior of PVB laminated glass under quasi-static and dynamic loadings," *Composites Part B: Engineering*, vol. 42, no. 2, pp. 302–308, 2011.
- [4] G. Herndon, K. Allen, A. Roberts, D. Phillips, and S. A. Batzer, "Automotive side glazing failure due to simulated human interaction," *Engineering Failure Analysis*, vol. 14, no. 8, pp. 1701–1710, 2007.
- [5] M. Larcher, G. Solomos, F. Casadei, and N. Gebbeken, "Experimental and numerical investigations of laminated glass subjected to blast loading," *International Journal of Impact Engineering*, vol. 39, no. 1, pp. 42–50, 2012.
- [6] P. A. Hooper, R. A. M. Sukhram, B. R. K. Blackman, and J. P. Dear, "On the blast resistance of laminated glass," *International Journal of Solids and Structures*, vol. 49, no. 6, pp. 899–918, 2012.
- [7] K. Fischer and I. Häring, "SDOF response model parameters from dynamic blast loading experiments," *Engineering Structures*, vol. 31, no. 8, pp. 1677–1686, 2009.
- [8] X. Zhang, H. Hao, and G. Ma, "Laboratory test and numerical simulation of laminated glass window vulnerability to debris impact," *International Journal of Impact Engineering*, vol. 55, pp. 49–62, 2013.
- [9] X. Zhang, H. Hao, and Z. Wang, "Experimental study of laminated glass window responses under impulsive and blast loading," *International Journal of Impact Engineering*, vol. 78, pp. 1–19, 2015.
- [10] X. Zhang and H. Hao, "Experimental and numerical study of boundary and anchorage effect on laminated glass windows under blast loading," *Engineering Structures*, vol. 90, pp. 96–116, 2015.
- [11] Y. Liu and B. Liaw, "Drop-weight impact tests and finite element modeling of cast acrylic/aluminum plates," *Polymer Testing*, vol. 28, no. 8, pp. 808–823, 2009.
- [12] J. Stenzler and N. Goulbourne, "Impact mechanics of transparent multi-layered polymer composites," in *Proceedings of the Society for Experimental Mechanics-Sem Annual Conference and Exposition on Experimental and Applied Mechanics*, 2009.
- [13] H. Chai and G. Ravichandran, "On the mechanics of fracture in monoliths and multilayers from low-velocity impact by sharp or blunt-tip projectiles," *International Journal of Impact Engineering*, vol. 36, no. 3, pp. 375–385, 2009.
- [14] H. Park and W. W. Chen, "Experimental investigation on dynamic crack propagating perpendicularly through interface in glass," *Journal of Applied Mechanics*, vol. 78, no. 5, Article ID 051013, 2011.
- [15] A. J. Hsieh and J. W. Song, "Measurements of ballistic impact response of novel coextruded PC/PMMA multilayered-composites," *Journal of Reinforced Plastics and Composites*, vol. 20, no. 3, pp. 239–254, 2001.
- [16] M. Hebert, C.-E. Rousseau, and A. Shukla, "Shock loading and drop weight impact response of glass reinforced polymer composites," *Composite Structures*, vol. 84, no. 3, pp. 199–208, 2008.
- [17] J. J.-W. Lee, I. K. Lloyd, H. Chai, Y.-G. Jung, and B. R. Lawn, "Arrest, deflection, penetration and reinitiation of cracks in brittle layers across adhesive interlayers," *Acta Materialia*, vol. 55, no. 17, pp. 5859–5866, 2007.
- [18] W. Zhang, S. Tekalur, and L. Huynh, "Impact behavior and dynamic failure of PMMA and PC plates," *Dynamic Behavior of Materials*, vol. 1, pp. 93–104, 2011.
- [19] W. Hu, Y. Wang, J. Yu, C.-F. Yen, and F. Bobaru, "Impact damage on a thin glass plate with a thin polycarbonate backing," *International Journal of Impact Engineering*, vol. 62, pp. 152–165, 2013.
- [20] N. Vandenberghe, R. Vermorel, and E. Villermaux, "Star-shaped crack pattern of broken windows," *Physical Review Letters*, vol. 110, no. 17, Article ID 174302, 2013.
- [21] J. Xu, Y. Sun, B. Liu et al., "Experimental and macroscopic investigation of dynamic crack patterns in PVB laminated glass sheets subject to light-weight impact," *Engineering Failure Analysis*, vol. 18, no. 6, pp. 1605–1612, 2011.
- [22] J. Chen, J. Xu, X. Yao et al., "Experimental investigation on the radial and circular crack propagation of PVB laminated glass subject to dynamic out-of-plane loading," *Engineering Fracture Mechanics*, vol. 112–113, pp. 26–40, 2013.
- [23] J. Chen, J. Xu, X. Yao, X. Xu, B. Liu, and Y. Li, "Different driving mechanisms of in-plane cracking on two brittle layers of laminated glass," *International Journal of Impact Engineering*, vol. 69, pp. 80–85, 2014.
- [24] J. Chen, J. Xu, B. Liu, X. Yao, and Y. Li, "Quantity effect of radial cracks on the cracking propagation behavior and the crack morphology," *PLoS ONE*, vol. 9, no. 7, Article ID e98196, 2014.
- [25] M. Timmel, S. Kolling, P. Osterrieder, and P. A. Du Bois, "A finite element model for impact simulation with laminated glass," *International Journal of Impact Engineering*, vol. 34, no. 8, pp. 1465–1478, 2007.
- [26] H. Hao and X. Zhang, "Analysis and design of glass windows against blast and impact loads," in *Proceedings of the 11th International Conference on Shock & Impact Loads on Structures*, Ottawa, Canada, 2015.
- [27] T. Pyttel, H. Liebertz, and J. Cai, "Failure criterion for laminated glass under impact loading and its application in finite element simulation," *International Journal of Impact Engineering*, vol. 38, no. 4, pp. 252–263, 2011.

- [28] Y. Peng, J. Yang, C. Deck, and R. Willinger, "Finite element modeling of crash test behavior for windshield laminated glass," *International Journal of Impact Engineering*, vol. 57, pp. 27–35, 2013.
- [29] F. W. Flocker and L. R. Dharani, "Modelling fracture in laminated architectural glass subject to low velocity impact," *Journal of Materials Science*, vol. 32, no. 10, pp. 2587–2594, 1997.
- [30] D. Sun, F. Andreiux, and A. Ockewitz, "Modeling of the failure behavior of windscreens and component tests," in *Proceedings of the 4th LS-DYNA Users Conference*, Bamberg, Germany, 2005.
- [31] X. Zhang, H. Hao, and G. Ma, "Parametric study of laminated glass window response to blast loads," *Engineering Structures*, vol. 56, pp. 1707–1717, 2013.
- [32] M. Larcher, M. Teich, N. Gebbeken et al., "Simulation of laminated glass loaded by air blast waves," *Applied Mechanics and Materials*, vol. 82, pp. 69–74, 2011.
- [33] S. J. Bennison, A. Jagota, and C. A. Smith, "Fracture of glass/poly(vinyl butyral) (Butacite®) laminates in biaxial flexure," *Journal of the American Ceramic Society*, vol. 82, no. 7, pp. 1761–1770, 1999.
- [34] J. Xu and Y. Li, "Crack analysis in PVB laminated windshield impacted by pedestrian head in traffic accident," *International Journal of Crashworthiness*, vol. 14, no. 1, pp. 63–71, 2009.
- [35] W. Xu and M. Zang, "Four-point combined DE/FE algorithm for brittle fracture analysis of laminated glass," *International Journal of Solids and Structures*, vol. 51, no. 10, pp. 1890–1900, 2014.
- [36] M. Y. Zang, Z. Lei, and S. F. Wang, "Investigation of impact fracture behavior of automobile laminated glass by 3D discrete element method," *Computational Mechanics*, vol. 41, no. 1, pp. 73–83, 2007.
- [37] W. Gao and M. Zang, "The simulation of laminated glass beam impact problem by developing fracture model of spherical DEM," *Engineering Analysis with Boundary Elements*, vol. 42, pp. 2–7, 2014.
- [38] S. Chen, M. Zang, D. Wang, Z. Zheng, and C. Zhao, "Finite element modelling of impact damage in polyvinyl butyral laminated glass," *Composite Structures*, vol. 138, pp. 1–11, 2016.
- [39] X. Xu, J. Chen, J. Xu, Y. Li, and X. Yao, "Modeling and experimental studies of crack propagation in laminated glass sheets," *SAE International Journal of Materials & Manufacturing*, vol. 7, no. 2, pp. 328–336, 2014.
- [40] J. Xu, Y. Li, X. Chen et al., "Characteristics of windshield cracking upon low-speed impact: numerical simulation based on the extended finite element method," *Computational Materials Science*, vol. 48, no. 3, pp. 582–588, 2010.
- [41] J. Xu, Y. Li, X. Chen et al., "Numerical study of PVB laminated windshield cracking upon human head impact," *Computers, Materials & Continua*, vol. 18, no. 2, pp. 183–211, 2010.
- [42] S. Zhao, L. R. Dharani, L. Chai, and S. D. Barbat, "Analysis of damage in laminated automotive glazing subjected to simulated head impact," *Engineering Failure Analysis*, vol. 13, no. 4, pp. 582–597, 2006.
- [43] J. Dolbow and T. Belytschko, "A finite element method for crack growth without remeshing," *International Journal for Numerical Methods in Engineering*, vol. 46, pp. 131–150, 1999.
- [44] T. Belytschko and T. Black, "Elastic crack growth in finite elements with minimal remeshing," *International Journal for Numerical Methods in Engineering*, vol. 45, no. 5, pp. 601–620, 1999.
- [45] T. Belytschko, N. Moës, S. Usui, and C. Parimi, "Arbitrary discontinuities in finite elements," *International Journal for Numerical Methods in Engineering*, vol. 50, no. 4, pp. 993–1013, 2001.
- [46] ABAQUS 6.13 analysis user's guide, Dassault Systems, 2013.
- [47] J. Lambros and A. J. Rosakis, "Dynamic crack initiation and growth in thick unidirectional graphite/epoxy plates," *Composites Science and Technology*, vol. 57, no. 1, pp. 55–65, 1997.
- [48] X. Zhang, Y. Zou, H. Hao, X. Li, G. Ma, and K. Liu, "Laboratory test on dynamic material properties of annealed float glass," *International Journal of Protective Structures*, vol. 3, no. 4, pp. 407–430, 2012.
- [49] M. Peroni, G. Solomos, V. Pizzinato, and M. Larcher, "Experimental investigation of high strain-rate behaviour of glass," *Applied Mechanics and Materials*, vol. 82, pp. 63–68, 2011.
- [50] L. Freund, *Dynamic Fracture Mechanics*, Cambridge University Press, Cambridge, UK, 1998.

## Research Article

# Influence of Grain Boundary on the Fatigue Crack Growth of 7050-T7451 Aluminum Alloy Based on Small Time Scale Method

**Weihan Wang, Weifang Zhang, Hongxun Wang, Xiaoliang Fang, and Xiaobei Liang**

*Science & Technology on Reliability & Environmental Engineering Laboratory, Beihang University, Beijing 100191, China*

Correspondence should be addressed to Weifang Zhang; 08590@buaa.edu.cn

Received 25 March 2016; Accepted 16 June 2016

Academic Editor: Liviu Marsavina

Copyright © 2016 Weihan Wang et al. This is an open access article distributed under the Creative Commons Attribution License, which permits unrestricted use, distribution, and reproduction in any medium, provided the original work is properly cited.

Based on the small time scale method, the influence of grain boundary on the fatigue crack growth of 7050-T7451 has been investigated. The interaction between fatigue crack and grain boundary was investigated by in situ SEM testing. Results showed that the fatigue crack growth will be retarded by grain boundary when the angle between fatigue crack and grain boundary is greater than 90 degrees. Mechanism analysis showed that the fatigue crack tip would not be able to open until the loading reached the 55% of maximum load, and the fatigue crack had been closed completely before the loading was not reduced to the minimum value, which led to the crack growth retardation. When the 7050-T7451 aluminum alloy suffered from fatigue loading with constant amplitude, a behavior of unstable fatigue crack growth could be observed often, and results indicated that the bridge linked mechanism led to the behavior. The grain boundary was prone to fracture during fatigue loading, and it became the best path for the fatigue crack growth. The fatigue crack tip would be connected with fractured grain boundary eventually, which led to the fast crack growth in different loading stage.

## 1. Introduction

7050-T7451 is a kind of high strength aluminum alloy which has been widely used in aerospace fields for its excellent properties, such as high specific strength, good fracture toughness, and stress corrosion resistance [1, 2]. Due to the fact that the aircraft bears complicated loadings in service, including maneuver loading, gust loading, and ground loading, the accumulation of fatigue damage will appear in the structure of 7050-T7451 aluminum alloy, which may lead to the fatigue fracture and cause disastrous accidents.

In essence, the fatigue fracture of 7050-T7451 aluminum alloy is the process of microdefect's initiation and growth. Microstructure such as grain boundary and second phase play an important role in the fatigue crack growth. Researchers found that the plastic deformation of metallic materials was seriously influenced by the grain boundary. Kamp et al. [3] observed that the transgranular propagation of persistent slip bands was impeded by the grain boundary and the fatigue crack tended to grow along grain boundaries or subgrain boundaries. Scharnweber et al. [4] analyzed the effect of grain boundary on small crack growth in stainless

steel, and results showed that the hindering effect of grain boundary on fatigue crack growth is mainly affected by the plastic area of crack tip. Holzapfel et al. [5] found that the subsurface orientation of grain boundaries is an important factor for interpreting crack growth rate at the surface. Terentyev and Gao [6] demonstrated that both low and high angle grain boundaries exhibit resistance to brittle crack propagation. Wang and Dong [7] indicated that the precipitation of carbide at grain boundary strengthened the grain boundary and decreased the crack growth rate.

At present, the researches for the effect of grain boundary on the fatigue crack growth are mainly focused on the fracture analysis and in situ testing [8–10]. The fracture analysis could be used for analyzing the damage mechanism; however, the deformation process during the loading period is hardly reflected and it limits the recognition of damage mechanism. The in situ testing is able to observe the whole process of fatigue crack growth in real time; however, existing methods mainly focused on the research of damage mechanism between hundreds or thousands of loading cycles, and seldom studies focused on the behavior of fatigue crack growth within one loading cycle. Recently, a method of small time

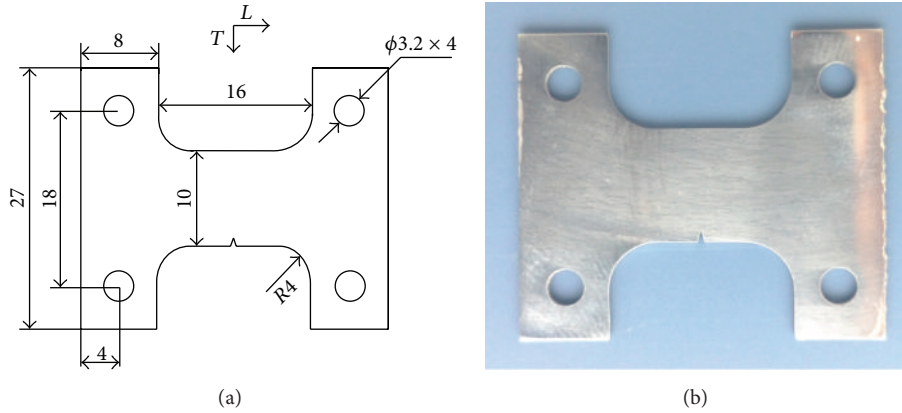


FIGURE 1: Geometry of the sample: (a) the sample design. (b) Manufactured sample (unit: mm).

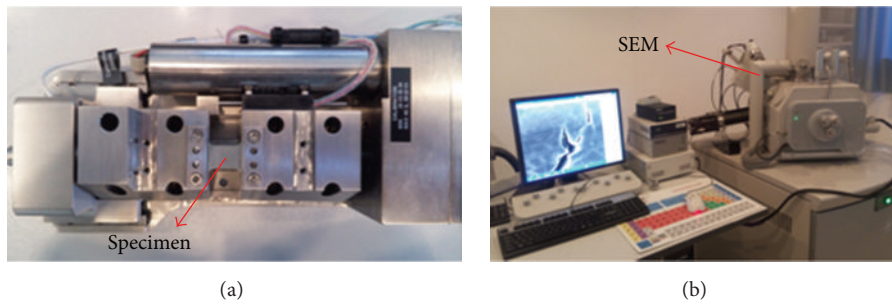


FIGURE 2: Experimental platform: (a) in situ testing stage. (b) Quanta 650 SEM.

scale used for the analysis of fatigue crack growth [11] has been developed, and it is different with existing cycle-based method for improving the accuracy. The advantage of this method [12] is that it could be used for analyzing the crack growth behavior at any time instant during one loading cycle.

With regard to the high strength aluminium alloy, the fatigue fracture is the result of damage accumulation formulated by different loading cycles [13–15], and the behavior of fatigue crack growth within one loading cycle determines the service life of 7050-T7451 aluminum alloy. Therefore, researching the damage deformation in smaller time scale is important for mastering the fracture mechanism of 7050-T7451 aluminum alloy, and it is beneficial for predicting the residual life of the material.

In this paper, the influence of grain boundary on fatigue crack growth of 7050-T7451 aluminum alloy has been investigated based on the small time scale method. The interaction between grain boundary and fatigue crack growth was researched in the experiment, such as retardation effect on the fatigue crack growth, as well as the behavior of unstable fatigue crack growth within one loading cycle; the result could provide the basis for the optimization and life prediction of 7050-T7451 aluminum alloy.

## 2. Experiment

As shown in Figure 1, the in situ sample with width  $W = 27$  mm, length  $L = 32$  mm, and thickness  $T = 0.8$  mm was prepared, and  $L$ - $T$  is the sampling direction.

TABLE 1: Mechanical properties of 7050-T7451 aluminum alloy.

Tensile strength (MPa)	Yield strength (MPa)	Young's modulus (GPa)
541	476	72

The material used in the experiment is 7050-T7451 aluminum alloy, and the material mechanical properties are given in Table 1.

Before the in situ testing, the fatigue precracking was accomplished in the hydraulic testing machine, INSTRON 8801, and the maximum length of precrack is 1 mm. After the precracking testing, the metallographic treatment was applied on the specimen, and the etching agent is Graff Sargent solution (1 mL HF, 16 mL HNO<sub>3</sub>, 3 g CrO<sub>3</sub>, and 83 mL H<sub>2</sub>O).

## 3. Results and Discussion

As shown in Figure 2(a), the sample was clamped in the in situ testing stage (Deben 2000), and the maximum loading of stage is 2 kN. The testing stage was installed in Quanta 650 scanning electron microscope (SEM) as shown in Figure 2(b), and the chamber pressure is less than  $3 \times 10^{-2}$  Pa.

Fatigue loading with constant amplitude was applied on the specimen. The stress ratio ( $R$ ) is 0.1 and the maximum loading is 1750 N. From the SEM, it was observed that the fatigue crack began to grow stably when the loading cycles

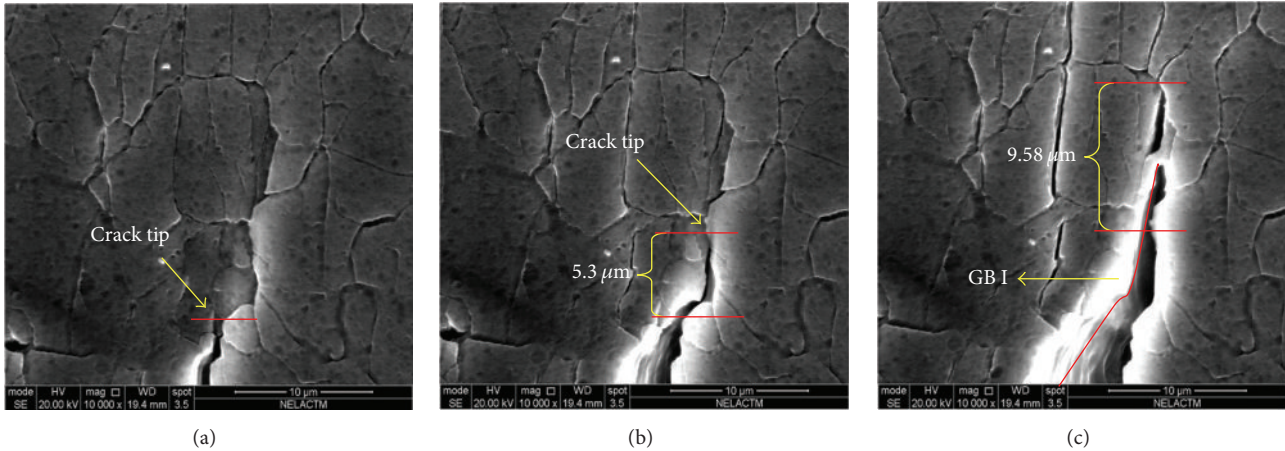


FIGURE 3: Micromorphology of fatigue crack: (a) at 40 cycles, (b) at 50 cycles, and (c) at 65 cycles.

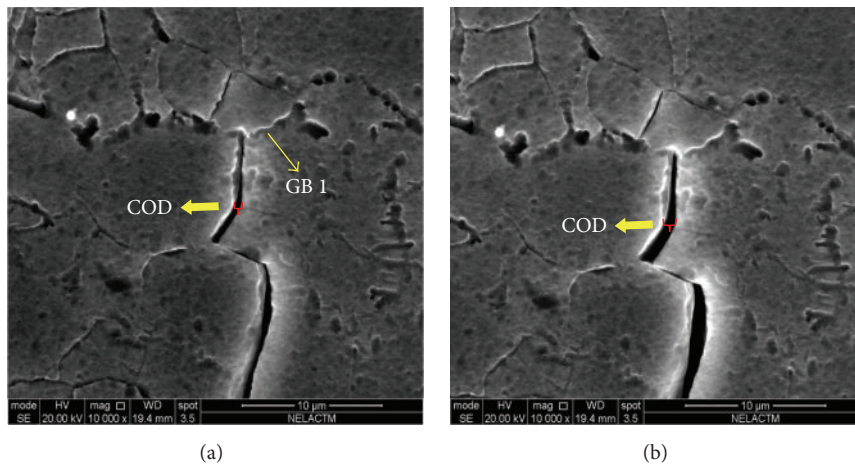


FIGURE 4: Micromorphology of fatigue crack: (a) at 77 cycles and (b) at 99 cycles.

arrived at 40, and the micromorphology of fatigue crack from 40 cycles to 65 cycles is shown in Figure 3.

It can be seen that the fatigue crack kept stable growth from 40 cycles to 65 cycles from Figure 3. When the fatigue crack propagates along grain boundary I (GB I), the mean fatigue crack growth rate is  $5.85 \times 10^{-4}$  mm/N. As shown in Figure 4(a), the fatigue crack tip approached grain boundary I (GB I) at 77 cycles.

From Figure 4(a), it can be seen that the angle between fatigue crack and GB I is more than 90 degrees at 77 cycles. When the loading cycle arrives at 99 cycles, the fatigue crack tip still stayed under GB I as shown in Figure 4(b). From Figure 4(b), it was observed that the crack opening displacement (COD) further increased at 99 cycles, and the retardation effect of GB I on the fatigue crack growth is more obvious.

In the loading stage of 99 cycles, micromorphology of fatigue crack at different loading level is shown in Figure 5.

As shown in Figure 5(a), the fatigue crack tip maintained closure when the loading increased to 540 N. The fatigue crack tip started to open when the loading reached 960 N as

shown in Figure 5(b). From Figures 5(c) and 5(d), it can be seen that the COD increased with the increasing of loading. As shown in Figure 5(d), when the loading reached 1750 N, the COD also achieved the maximum.

From Figure 5, it can be seen that some microcracks appear in front of the main crack, and it mainly initiated in the grain boundary. Under the tensile loading, the front of main crack will become a high stress concentration area. Due to the uncoordinated deformation existing between grain and grain boundary, some grain boundary with weak performance will initiate microcrack in front of the main crack under tensile loading.

In the unloading stage of 99 cycles, micromorphology of fatigue crack at different loading level is shown in Figure 6.

As shown in Figure 6, when the loading decreased from 1380 N to 540 N, the COD also decreased, and the fatigue crack tip recovered from the opening status to the closure status. From Figure 6(d), it can be seen that the fatigue crack tip had been already closed until the loading was decreased to the minimum. It was obtained that the loading value of crack closure is 540 N which is lower than that of crack opening.

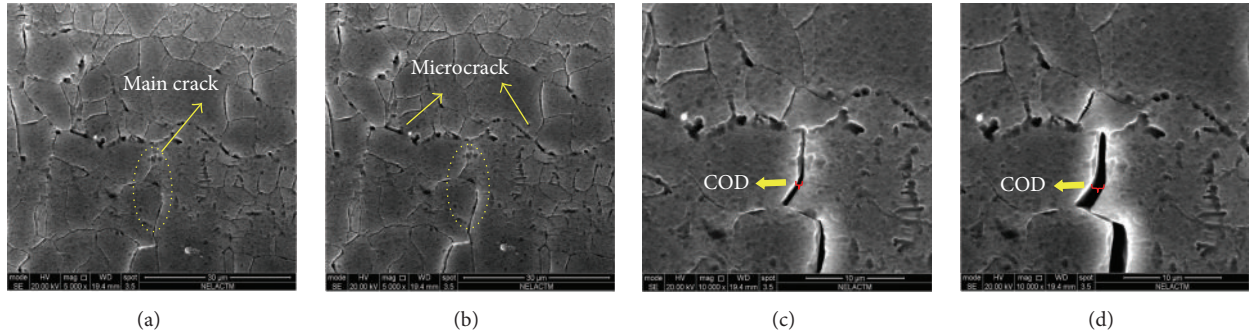


FIGURE 5: In the loading stage of 99 cycles, micromorphology of fatigue crack at different loading level: (a) at 540 N, (b) at 960 N, (c) at 1380 N, and (d) at 1750 N.

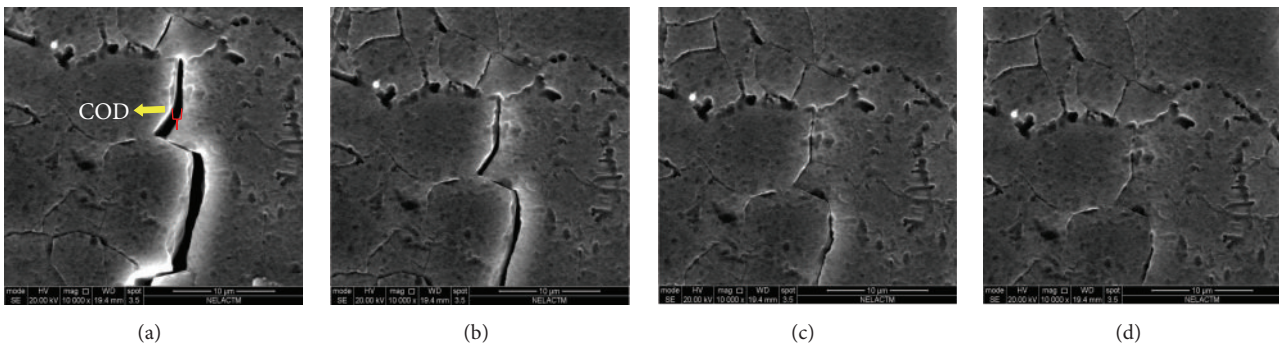


FIGURE 6: In the unloading stage of 99 cycles, micromorphology of fatigue crack at different loading level: (a) at 1380 N, (b) at 960 N, (c) at 750 N, and (d) at 540 N.

When it reached 111 cycles, the fatigue crack had already been grown rapidly along GB 1 as shown in Figure 7. It can be seen that the fatigue crack growth was retarded by GB 1 for 33 cycles since the loading cycles of 77.

As shown in Figure 7, the fatigue crack had been grown along GB 1 and the crack tip approached Grain 1 at 111 cycles. Meanwhile, two new cracking paths had been developed: the first path is the crack grew along GB 2, and the second path is the crack that passed through GB 3 and grew into Grain 1.

Because the fatigue crack had been retarded by GB 1 from 77 cycles for several loading cycles, large amounts of deformation energy were concentrated in front of the crack tip. When the energy reached the maximum, the fatigue crack tip will be suddenly opened and the fatigue crack grew along GB 1 promptly. The fatigue crack was able to pass through GB 3 and grow into Grain 1 by the driving of released energy; meanwhile, the remaining energy drove the fatigue crack to grow along GB 2.

In the loading stage of 112 cycles, micromorphology of fatigue crack at different loading level is shown in Figure 8.

From Figures 8(a) and 8(b), it can be seen that the fatigue crack tip remained closed when the loading value is less than 700 N. As shown in Figure 8(c), when the loading reached 700 N, the fatigue crack tip started to open. From Figures 8(d) and 8(e), it can be seen that the COD increased with the increment of the loading, and the fracture of GB 4 could be observed in front of the crack tip.

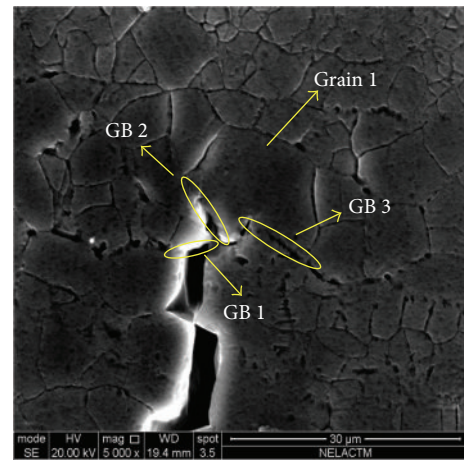


FIGURE 7: Micromorphology of fatigue crack at 111 cycles.

As shown in Figures 8(f) and 8(g), when the loading reached 1225 N, the tendency that the crack would grow along GB 2 and connect with GB 4 is more obvious. From Figure 8(h), it can be seen that the COD had been achieved to the maximum when the loading reached 1750 N, and it presented a tendency that the crack tip would be soon connected with GB 4.

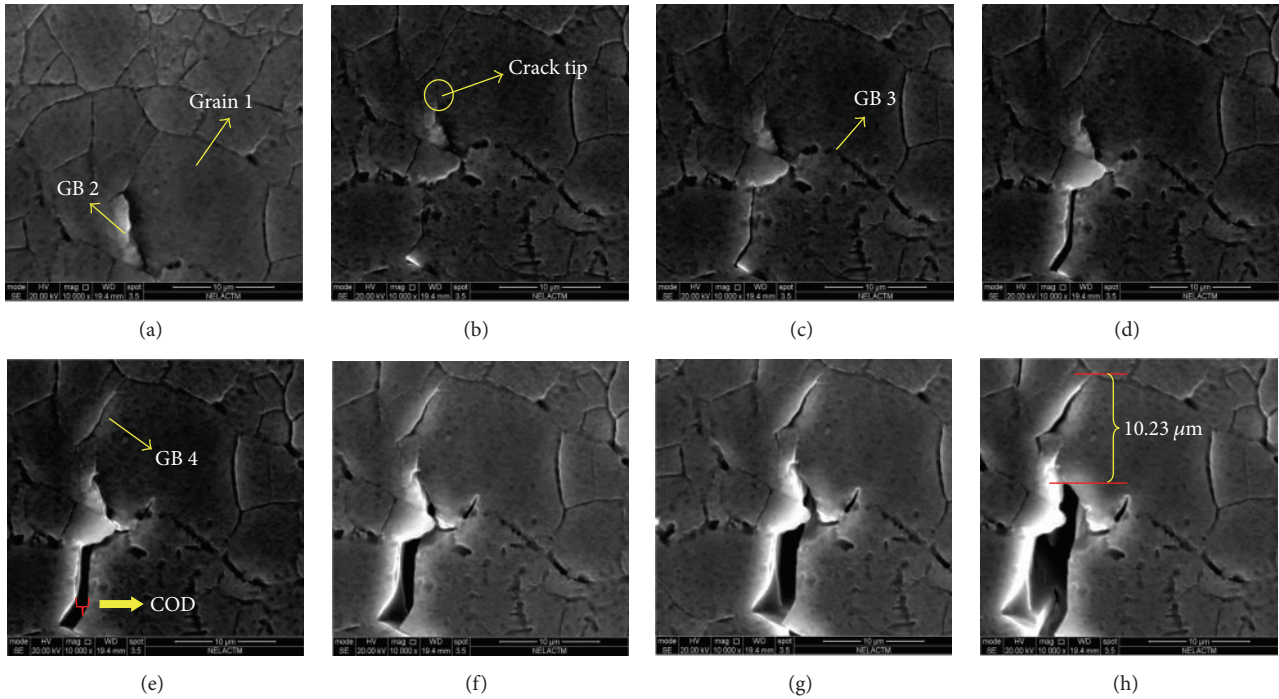


FIGURE 8: In the loading stage of 112 cycles, micromorphology of fatigue crack at different loading level: (a) at 175 N, (b) at 525 N, (c) at 700 N, (d) at 875 N, (e) at 1050 N, (f) at 1225 N, (g) at 1400 N, and (h) at 1750 N.

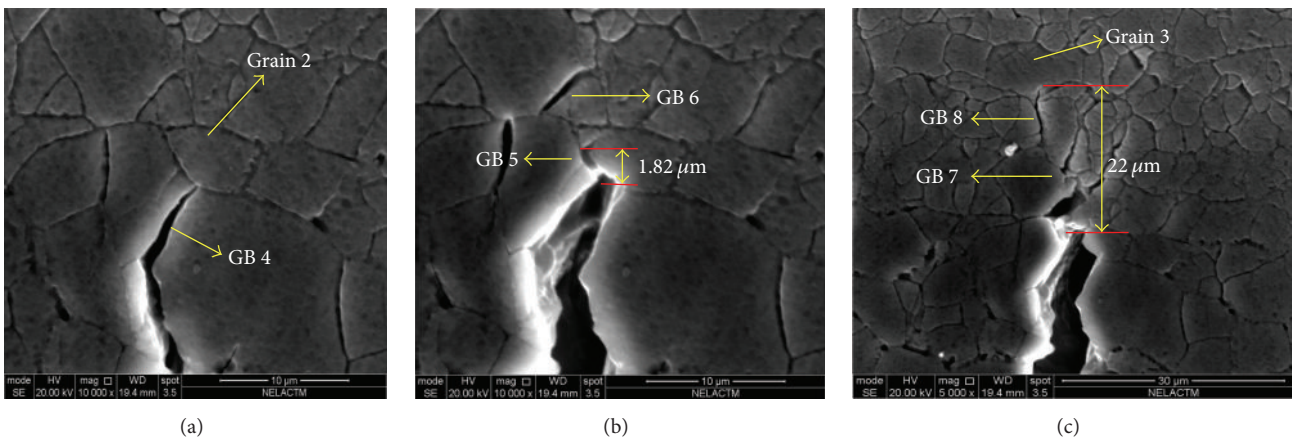


FIGURE 9: Micromorphology of fatigue crack at different loading cycles: (a) at 114 cycles, (b) at 116 cycles, and (c) at 119 cycles.

After two loading cycles, the micromorphology of fatigue crack at 114 cycles is shown in Figure 9(a).

As shown in Figure 9(a), the fatigue crack tip had been connected with GB 4 at 114 cycles, and the crack tip approached Grain 2 at present. It was obtained that the fatigue crack growth rate is  $3.41 \times 10^{-3}$  mm/N when the fatigue crack propagates along GB 4. When it reached 116 cycles, it can be seen that the fatigue crack grew along GB 5 as shown in Figure 9(b). The increment of the length of the fatigue crack is 1.82 μm between 114 and 116 cycles, and the fracture of GB 6 could be observed. It was obtained that the fatigue crack growth rate is  $9.1 \times 10^{-4}$  mm/N when the fatigue crack propagates along GB 5. From Figure 9(c), it can be seen that

the fatigue crack had been connected with GB 6 when the loading cycle reached 119, and the fatigue crack tip entered into Grain 3 at present. It is obvious that from 116 to 119 cycles, the increment of the length of the fatigue crack is 22 μm. It was obtained that the fatigue crack growth rate is  $7.3 \times 10^{-3}$  mm/N when the fatigue crack propagates along GB 6 and GB 8.

Micromorphology of fatigue crack from 126 cycles to 131 cycles is shown in Figure 10.

As shown in Figure 10(a), the increment of fatigue crack is 5 μm in Grain 3 from 119 cycles to 126 cycles. Meanwhile, the fracture of GB 9 could be observed in front of Grain 3. As shown in Figure 10(b), the fatigue crack further grew at 129 cycles, and the fatigue crack tip opening increased.

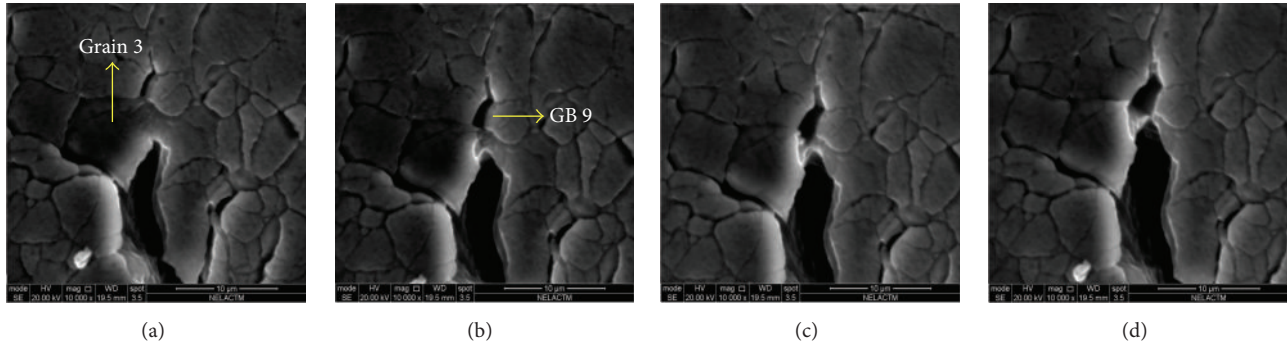


FIGURE 10: Micromorphology of fatigue crack at different loading cycles: (a) at 126 cycles, (b) at 129 cycles, (c) at 130 cycles, and (d) at 131 cycles.

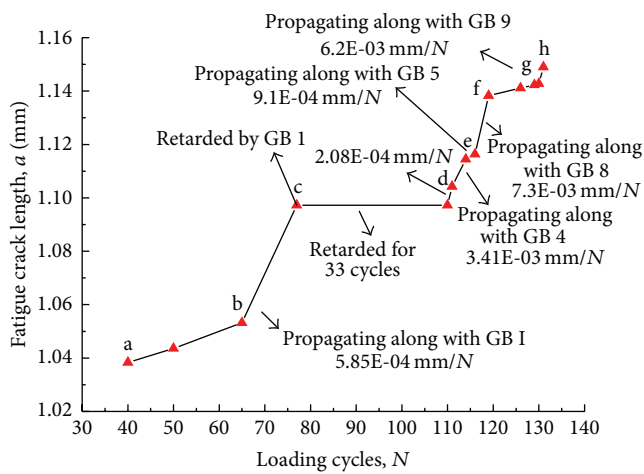


FIGURE 11: Increment of fatigue crack length with the change of loading cycles.

When the loading cycle reached 130, GB 9 was fractured further and the fatigue crack tip approached GB 9. From Figure 10(d), it can be seen that the fatigue crack tip had completely passed through Grain 3 and it was connected with GB 9.

The change of fatigue crack length with the loading cycles from 40 cycles to 131 cycles is shown in Figure 11.

It can be seen that the fatigue crack growth rate is different between different loading cycles. The increment of fatigue crack is the minimum from 77 cycles to 111 cycles in the experiment and the fatigue crack growth rate is  $2.08 \times 10^{-4}$  mm/N. The retardation of fatigue crack growth since 77 cycles is mainly caused by the impediment of grain boundary (GB I). The fatigue crack growth will be retarded by the grain boundary when the angle between fatigue crack and grain boundary is greater than 90 degrees in 7050-T7451 aluminum alloy.

The fatigue crack growth is the fastest from 116 cycles to 119 cycles, and the fatigue crack growth rate is  $7.3 \times 10^{-3}$  mm/N. The following is  $6.2 \times 10^{-3}$  mm/N from 130 cycles to 131 cycles. The rapid growth of fatigue crack is mainly caused by the bridge linked mechanisms between grain boundary and fatigue crack. During the fatigue loading

of 7050-T7451 aluminum alloy, the grain boundary is prone to fracture. When the fatigue crack tip connected with the grain boundary, the fatigue crack presented fast unstable growth, which led to the life reduction of 7050-T7451 aluminum alloy.

## 4. Conclusions

(1) When 7050-T7451 aluminum alloy is under the fatigue loading with constant amplitude, the fatigue crack growth will be retarded by the grain boundary. When the angle between the fatigue crack and the grain boundary is greater than 90 degrees, the retardation phenomenon is more obvious.

(2) The fatigue crack tip is not able to open until the loading reached 55% of the maximum value when the fatigue crack was retarded by the grain boundary. The fatigue crack had been completely closed when the loading is not reduced to the maximum value, and it is observed that the crack opening loading is higher than the crack closure loading.

(3) When the 7050-T7451 aluminum alloy suffered from fatigue loading with constant amplitude, a behavior of unstable fatigue crack growth could be observed in 7050-T7451 aluminum alloy, which related to the bridge linked mechanism of fatigue crack. The grain boundary was prone to fracture during fatigue loading of 7050-T7451 aluminum alloy, and the fractured GB became the best path for the fatigue growth. During the fatigue loading stage, the fatigue crack tends to grow in the direction of cracking grain boundary, and it will be connected with fractured GB eventually, which led to the fast growth of fatigue crack.

## Competing Interests

The authors declare that they have no competing interests.

## Acknowledgments

This research is supported by two National technical infrastructure projects, the first Project no. is JSZL 2014601B001 and the second Project no. is JSZL 2014601B004. Special thanks go to Professor Dai for his assistance in the revision of paper.

## References

- [1] A. W. Mello, A. Nicolas, R. A. Lebensohn, and M. D. Sangid, "Effect of microstructure on strain localization in a 7050 aluminum alloy: comparison of experiments and modeling for various textures," *Materials Science and Engineering: A*, vol. 661, pp. 187–197, 2016.
- [2] D. C. C. Magalhães, M. F. Hupalo, and O. M. Cintho, "Natural aging behavior of AA7050 Al alloy after cryogenic rolling," *Materials Science and Engineering A*, vol. 593, pp. 1–7, 2014.
- [3] N. Kamp, N. Gao, M. J. Starink, and I. Sinclair, "Influence of grain structure and slip planarity on fatigue crack growth in low alloying artificially aged 2xxx aluminium alloys," *International Journal of Fatigue*, vol. 29, no. 5, pp. 869–878, 2007.
- [4] M. Scharnweber, W. Tirschler, V. Mikulich, S. Jacob, C.-G. Oertel, and W. Skrotzki, "Influence of crack length and grain boundaries on the propagation rate of short cracks in austenitic stainless steel," *Scripta Materialia*, vol. 67, no. 7-8, pp. 677–680, 2012.
- [5] C. Holzapfel, W. Schäf, M. Marx, H. Vehoff, and F. Mücklich, "Interaction of cracks with precipitates and grain boundaries: understanding crack growth mechanisms through focused ion beam tomography," *Scripta Materialia*, vol. 56, no. 8, pp. 697–700, 2007.
- [6] D. Terentyev and F. Gao, "Blunting of a brittle crack at grain boundaries: an atomistic study in BCC Iron," *Materials Science and Engineering A*, vol. 576, pp. 231–238, 2013.
- [7] P. Wang and J. X. Dong, "Effect of the grain boundary carbide on the crack propagation rates of GH864 alloy," *Rare Metal Materials and Engineering*, vol. 43, no. 11, pp. 2723–2727, 2014.
- [8] W. Y. Zhang, "Study on the low cycle fatigue fracture in TA5 titanium alloy plates," *Rare Metal Materials and Engineering*, vol. 27, no. 3, pp. 156–160, 1998.
- [9] K. Dám, P. Lejček, and A. Michalcová, "In situ TEM investigation of microstructural behavior of superplastic Al-Mg-Sc alloy," *Materials Characterization*, vol. 76, pp. 69–75, 2013.
- [10] C. Meng, D. Zhang, L. Zhuang, and J. Zhang, "Correlations between stress corrosion cracking, grain boundary precipitates and Zn content of Al-Mg-Zn alloys," *Journal of Alloys and Compounds*, vol. 655, Article ID 35434, pp. 178–187, 2016.
- [11] Z. Lu and Y. Liu, "Small time scale fatigue crack growth analysis," *International Journal of Fatigue*, vol. 32, no. 8, pp. 1306–1321, 2010.
- [12] W. Zhang and Y. Liu, "Investigation of incremental fatigue crack growth mechanisms using in situ SEM testing," *International Journal of Fatigue*, vol. 42, pp. 14–23, 2012.
- [13] A. Pineau, D. L. McDowell, E. P. Busso, and S. D. Antolovich, "Failure of metals II: fatigue," *Acta Materialia*, vol. 107, pp. 484–507, 2015.
- [14] B. Sun, Y.-L. Xu, and Z. Li, "Multi-scale model for linking collective behavior of short and long cracks to continuous average fatigue damage," *Engineering Fracture Mechanics*, vol. 157, pp. 141–153, 2015.
- [15] J. Schijve, "The application of small overloads for fractography of small fatigue cracks initiated under constant-amplitude loading," *International Journal of Fatigue*, vol. 70, pp. 63–72, 2015.

## Research Article

# Prediction Intervals for the Failure Time of Prestressed Concrete Beams

**Sebastian Szugat, Jens Heinrich, Reinhard Maurer, and Christine H. Müller**

*TU Dortmund University, 44227 Dortmund, Germany*

Correspondence should be addressed to Sebastian Szugat; [szugat@statistik.tu-dortmund.de](mailto:szugat@statistik.tu-dortmund.de)

Received 24 March 2016; Accepted 20 July 2016

Academic Editor: Konstantinos I. Tserpes

Copyright © 2016 Sebastian Szugat et al. This is an open access article distributed under the Creative Commons Attribution License, which permits unrestricted use, distribution, and reproduction in any medium, provided the original work is properly cited.

The aim is the prediction of the failure time of prestressed concrete beams under low cyclic load. Since the experiments last long for low load, accelerated failure tests with higher load are conducted. However, the accelerated tests are expensive so that only few tests are available. To obtain a more precise failure time prediction, the additional information of time points of breakage of tension wires is used. These breakage time points are modeled by a nonlinear birth process. This allows not only point prediction of a critical number of broken tension wires but also prediction intervals which express the uncertainty of the prediction.

## 1. Introduction

Actually, the assessment of existing prestressed concrete bridges by means of recalculation in conjunction with rehabilitation and strengthening is gaining more and more importance compared to the construction of new bridges. The current design codes had been developed over decades always adapting new design approaches that are current at that time. Even for this reason the recalculation of older existing structures often leads to deficiencies concerning load-bearing capacity, durability, and resistance against fatigue. The ongoing increase of traffic concerning heavy trucks underlines the importance of assessment and maintenance of the transport networks and particularly the bridge stock, the latter with regard to structural safety.

Beside corrosion effects, the major influence for time dependent losses of load-bearing capacity is the phenomenon of fatigue failure. Fatigue is caused by frequent cyclic loads due to the crossing of heavy trucks on the bridge deck. Beside steel bridges, prestressed concrete bridges are affected as well; see, for example, [1, 2]. For the design of new bridges against fatigue or the assessment of existing bridges by means of recalculation, *S-N* curves are needed. The latter describes the fatigue resistance of the materials. With regard

to the prestressed concrete bridges, this refers especially to the embedded reinforcing and prestressing steel in cracked sections. For the design and assessment of bridges, *S-N* curves are needed in a range up to  $10^8$  load cycles. To obtain values for the whole range and for a better understanding of the fatigue behavior of prestressed concrete bridges, one has to carry out long running tests which are extremely expensive. Hence, there is a great need to optimize these tests procedures.

From historical view, the first documented fatigue tests on prestressed concrete beams will be found in [3]. Larger test series carried out at the University of Texas are described by [4]. Further studies can be found in [5, 6]. A comprehensive survey regarding fatigue tests on prestressing steel in air and embedded in concrete is given in [7]. The latter leads to fatigue strength which is significantly less than studied before.

During the course of the Collaborative Research Center SFB 823 Statistical Modeling of Nonlinear Dynamic Processes, large-scale test series with stress ranges down to 50 MPa and failure times in a range up to  $10^8$  load cycles are carried out at TU Dortmund University. The aim of the ongoing experimental studies described subsequently is to investigate fatigue behavior and to provide characteristic *S-N* curves for prestressing steel in curved steel ducts embedded

in concrete of posttensioned members.  $S-N$  curves belong to the basics which are needed to verify prestressed concrete bridges against fatigue. However, tests under cyclic loading of posttensioned concrete beams may be very time-consuming and expensive. Especially at very low stress ranges with a very high number of cycles, which are of particular interest concerning prestressed concrete bridges, even an optimized test with a realized load frequency of 10 Hz lasts several months. For posttensioned steel, an endurance range in the  $S-N$  curves has not been established by tests up to now. Therefore, the  $S-N$  curve in the range up to  $10^8$  cycles can only hypothetically be guessed, until appropriate test results will be available.

For low loads down to 60 MPa, tests in the research project SFB 823 last nearly 100 days so that most experiments are done under higher loads up to 200 MPa. Hence so-called accelerated failure tests (AFT) were conducted. If there are enough AFT experiments, the lifetime at a small load can be estimated from the  $S-N$  curves; see, for example, [8–10]. However, here also these AFT experiments last long and are expensive so that the results of only few experiments are available, in our project, for example, results of ten experiments. Such small numbers of experiments are too small to estimate the lifetime at low load with enough precision. Nevertheless, the main interest lies in the lifetime at low stress at 50 MPa or even lower.

Hence, we propose here two methods which use additional information beside the failure times of former tests to predict the failure time at low stress. The additional information is given by a degradation measure. Usually the sizes of cracks are used as degradation measures; see, for example, [11–13]. But here we have the advantage that the time points of the breaking of the tension wires in the prestressed concrete beams are available since acoustic signals obtained by a microphone indicate clearly the breakage of a wire. We model the time points of the breaking of the tension wires with a point process where the waiting times for the next breaking of a tension wire follow an exponential distribution depending only on the number of wires which are broken before. Such point processes are also called birth processes (see, e.g., [14]).

Point processes as Poisson processes and renewal processes are often considered in reliability and lifetime analysis; see, for example, [15, 16]. Reference [15] treats also a linear birth process for fatigue accumulation in Chapter 18 and uses birth processes with time-varying intensity for crack growth in Chapter 26. However, our birth process is nonlinear in the number of broken tension wires. The nonlinearity is due to the redistribution of the load on the tension wires. There are several approaches for load sharing systems as those of [17, 18] or [19]. But they assume several systems exposed to the same stress so that accelerated failure tests cannot be treated.

Linking the nonlinear birth process of each experiment with its underlying stress, we provide two types of prediction intervals for the time of a critical number of broken tension wires. The critical number of broken tension wires has a direct relation to the failure time of the concrete beam so that its lifetime can be derived from the time of the critical number of broken tension wires. We use the times between successive

breaks of the accelerated experiments and some optional first breaking times of the concrete beam for which we want to obtain the prediction interval.

Although prediction intervals provide not only a prediction but also its precision, they are often not derived. Most prediction intervals are only derived for the simple situation that all experiments are conducted under the same conditions; see, for example, [8, 9, 20–25]. Only few prediction intervals for accelerated experiments are available as those of [8] for normal distributed lifetimes and [26] for exponential distributed lifetimes while the prediction intervals of [26] are based on simulations. Our prediction intervals are simulation-free and thus faster to calculate.

In Section 2 the description of the experiments with the concrete beams is given. Section 3 provides the statistical model with the birth process and its link to the stress while Section 4 treats the two proposed prediction intervals. The results for our experiments with the concrete beams and some simulations are given in Section 5. At last, Section 6 provides a conclusion.

## 2. Test Setup and Procedure

The tests on prestressed concrete girders (hereinafter SB01–SB05) within the Collaborative Research Center SFB 823 have been carried out at TU Dortmund University. The experimental setup is based on the setup of already conducted experiments, also carried out at TU Dortmund University (see [27]).

The series described in [27] consisted of five concrete girders (TR01–TR05) with tendons for posttensioning. They had been tested with different stress ranges  $\Delta\sigma_p$  from 455 MPa to 98 MPa for the prestressing steel in curved steel ducts. The prestressing steel of the tendons used for these test girders has been taken from an existing bridge which was built in 1957 and demolished in 2007. Each of the taken  $3/8''$  strands consists of seven single wires. Each strand had been consisted of a steel grade St1570/1770 with a diameter of 9.3 mm and a cross-sectional area of  $52 \text{ mm}^2$ . The prestressing steel had been strained at a length of 2 m for the curved tendon with a minimum radius of  $r = 5 \text{ m}$  in a region of the test girder with pure bending without shear. Hence, the influence of fretting corrosion between the tensioned strand and steel duct is included.

The experimental setup consists of steel frames, the concrete girder, and a hydraulic press in a four-column testing machine, which can apply a cyclic load at maximum  $\pm 2500 \text{ kN}$  (see Figures 1 and 2). The overall dimensions of the concrete girder are  $4.00 \text{ m} \times 1.00 \text{ m} \times 0.30 \text{ m}$ . A recess in midspan of the girder in conjunction with a steel contact element ensures the unambiguous definition of the center of the compression zone in the upper cross-sectional part and from this the exact inner lever arm and tension force in the tendon.

The test girders of the second test series SB01–SB05 are very similar to those of the first test series TR01–TR05. A few modifications like a steel-link in the pressure area in the girder's center and the prestressing of the anchoring rods increase the stiffness of the whole test stand and the test

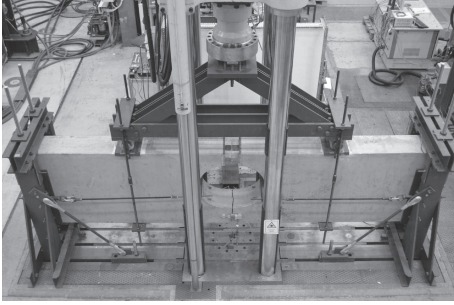


FIGURE 1: Photograph of the experimental setup.

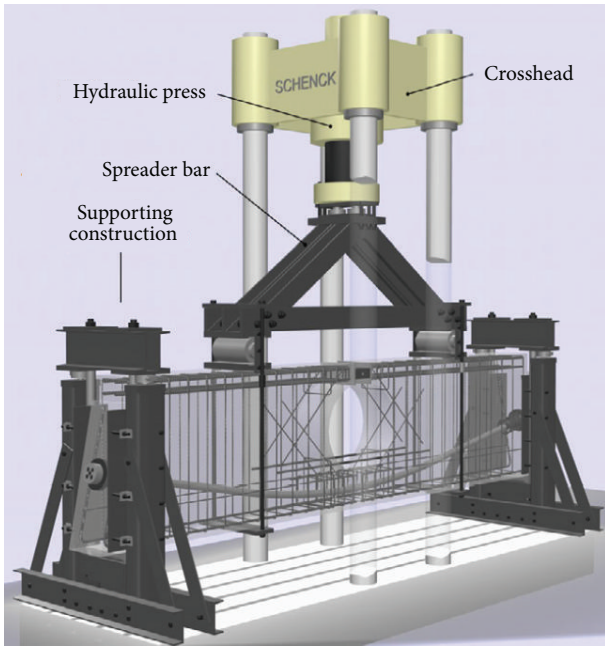


FIGURE 2: 3D CAD model of the test stand.

frequency, whereby the duration could be reduced. The test frequency was set at 1.5–2 Hz for the first test series and was optimized up to 10 Hz for the second test series.

The experimental procedure was the same for both test series and will be described below. Firstly, all the press force was applied to the concrete girder. The load was increased continuously until an initial crack in the tension zone appears and a bearing effect of the concrete in tension could be excluded. Initially the girder has been released in a way, so that the load could be increased up to the respective medium load range. After that, the fatigue strength of the embedded prestressing steel was tested under a constant cyclic loading until a critical number of the wires had broken due to fatigue and the remaining section could no longer withstand the load.

During the experiment runtime, the crack width in midspan of the girder was measured continuously. As soon as a wire has broken due to fatigue, the measurement of the crack width showed a sudden increase. The amount of increase depends on the total number of already broken

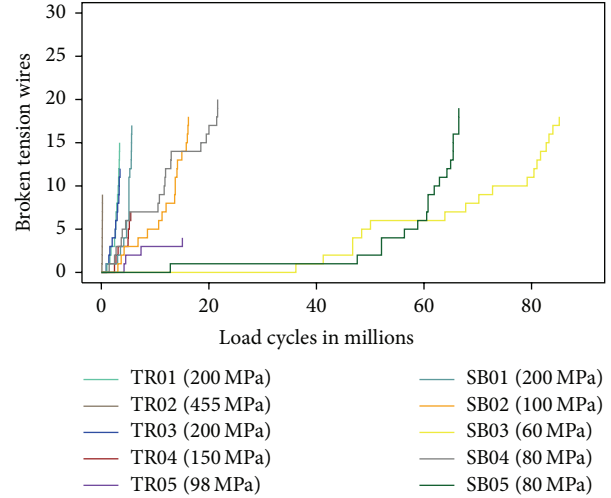


FIGURE 3: Tests results for TR01–TR05 and SB01–SB05.

wires. The more the wires were broken, the greater the sudden increase was (see [7]). Although the time point of the breaking of a tension wire could be determined by the sudden increase of the crack width, a more precise determination of the breaking times was obtained with a microphone since each breaking causes a short load noise.

It could be that more than one tension wire is breaking at a time point. However, this cannot be determined, neither by the crack width nor by microphone. But this should be a rare event so that we neglect this possibility in our model.

The applied stress range  $\Delta\sigma_p$  and the time of every broken wire in each of test girders are shown in Figure 3.

### 3. Statistical Model

Let  $n$  be the time measured in load cycles and  $\mathcal{N}_n$  the number of broken prestressing wires up to time  $n$ . The waiting time between the  $(i-1)$ 'th and the  $i$ 'th broken wire is defined as  $\Delta N_i := \min\{n : \mathcal{N}_n \geq i\} - \min\{n : \mathcal{N}_n \geq i-1\}$ . The exponential distribution is commonly used to model lifetimes. Hence, we assume that

$$\Delta N_i \sim \text{Exp}(\lambda_\theta(i-1, s)), \quad i = 1, \dots, I \leq I_{\max}, \quad (1)$$

where  $\lambda_\theta(i-1, s)$  is the parameter of the exponential distribution, which depends on the number of broken wires  $i$  and the stress range  $s := \Delta\sigma_p$  of the experiment.  $I_{\max}$  denotes the maximum number of possible wire breakages, so that we have  $I_{\max} = 35$  here, because there are five strands with seven wires each embedded in a beam.

Note that  $\mathcal{N}_n$  is the classical Poisson process if  $\lambda_\theta$  does not depend on the number  $i$  of broken tension wires. If it depends on  $i$ , it is birth process; see, for example, [14].

A simple assumption for  $\lambda_\theta(i-1, s)$  in the experiments with prestressed concrete is

$$\lambda_\theta(i, s) := h_\theta \left( s \cdot \frac{I_{\max}}{I_{\max} - i} \right), \quad (2)$$

for a function  $h_\theta$  which depends on  $\theta \in \Theta$ . The term  $I_{\max}/(I_{\max} - i)$  expresses the increase of stress on the remaining  $I_{\max} - i$  wires when  $i$  wires are broken. In particular, when half of the wires are broken ( $i = I_{\max}/2$ ) then the stress is doubled. The function  $h_\theta$  models the dependence of the waiting time for the next breakage on the stress of the remaining tension wires. In this work we choose

$$h_\theta(x) := \exp(-\theta_1 + \theta_2 \log(x)), \quad (3)$$

with  $\theta = (\theta_1, \theta_2)^T \in \Theta = [0, \infty)^2$  so that

$$\begin{aligned} \log(E(\Delta N_i)) &= \log\left(\frac{1}{\lambda_\theta(i-1, s)}\right) \\ &= \theta_1 - \theta_2 \cdot \log\left(s \cdot \frac{I_{\max}}{I_{\max} - i + 1}\right); \end{aligned} \quad (4)$$

that is, it is assumed that the expected time until the next wire break can be modeled in that way. This model for the logarithmized expectation coincides with a well-known and used model in the engineering sciences from [28].

Since we do not only have one experiment with one stress level  $s$  but also have  $J$  experiments with different stress ranges  $s_1, \dots, s_j$ , we observe realizations  $\Delta n_{i,j}$  of

$$\Delta N_{i,j} \sim \text{Exp}(\lambda_\theta(i-1, s_j)) \quad (5)$$

for  $i = 1, \dots, I_j \leq I_{\max}$ ,  $j = 1, \dots, J$ .

For the prediction we have a new beam experiment with realizations  $\Delta n_{i,0}$  of

$$\Delta N_{i,0} \sim \text{Exp}(\lambda_\theta(i-1, s_0)) \quad (6)$$

with  $i = 1, \dots, I_0 \ll I_{\max}$ . We use  $I_0 = 0$  if no observations of broken tension wires are available for this experiment. In particular, our aim is also to make predictions for low stress levels where no experiments were conducted up to now.

Let  $I_{\text{crit}}$  denote a critical number of broken tension wires which is closely related to the lifetime of the concrete beam. Then we want to predict the time of the  $I_{\text{crit}}$ 'th failure ( $I_0 < I_{\text{crit}} < I_{\max}$ ), that is, the time measured in load cycles given by

$$\Delta n_{1,0} + \dots + \Delta n_{I_0,0} + \Delta N_{I_0+1,0} + \dots + \Delta N_{I_{\text{crit}},0}. \quad (7)$$

Since  $\Delta n_{1,0}, \dots, \Delta n_{I_0,0}$  have already been observed, the task reduces to the prediction of the future sum of waiting times:

$$\Delta N_{\text{fut}} := \Delta N_{I_0+1,0} + \dots + \Delta N_{I_{\text{crit}},0}. \quad (8)$$

#### 4. Prediction Intervals

If the parameter  $\theta = (\theta_1, \theta_2)^T$  is known, then the prediction for the expected time (number of load cycles) until the number of broken tension wires attains the critical number  $I_{\text{crit}}$  is

$$\begin{aligned} \Delta n_{1,0} + \dots + \Delta n_{I_0,0} + \frac{1}{\lambda_\theta(I_0, s_0)} + \dots \\ + \frac{1}{\lambda_\theta(I_{\text{crit}} - 1, s_0)}, \end{aligned} \quad (9)$$

since the expectation of random variable  $\Delta N_{i,0}$  with exponential distribution satisfies  $E(\Delta N_{i,0}) = 1/\lambda_\theta(i-1, s_0)$ .

However, such a point prediction will usually fail the true future time. To include the precision of the prediction, a prediction interval for  $\Delta N_{\text{fut}}$  and thus for  $\Delta n_{1,0} + \dots + \Delta n_{I_0,0} + \Delta N_{\text{fut}}$  is needed. A  $(1-\alpha)$ -prediction interval  $\mathbb{P}$  for the future value of  $\Delta N_{\text{fut}}$  should satisfy

$$P(\Delta N_{\text{fut}} \in \mathbb{P}) \geq 1 - \alpha, \quad (10)$$

where  $\alpha$  is usually a small value like  $\alpha = 0.1$ . It means that the future observation  $\Delta N_{\text{fut}}$  lies in the prediction interval  $\mathbb{P}$  with a probability greater than  $1 - \alpha$ , for example, 90% if  $\alpha = 0.1$ . The smaller  $\alpha$  is and thus the larger  $1 - \alpha$  is, the larger and more noninformative the prediction interval is. Therefore  $\alpha = 0.1$  is a good choice since the probability is at least 90% that the prediction interval includes the future observation.

In order to find a prediction interval for  $\Delta N_{\text{fut}}$ , the distribution of  $\Delta N_{\text{fut}}$  in expression (8) is needed. As  $\Delta N_{\text{fut}}$  is the sum of exponential distributions each with a different parameter, it is hypoexponentially distributed (see, e.g., [29, pp. 293]) with cummulative distribution function:

$$\begin{aligned} F_{\Delta N_{\text{fut}}, \theta}(\Delta n_{\text{fut}}) \\ := \sum_{i=I_0+1}^{I_{\text{crit}}} a_i(\theta) (1 - \exp(-\Delta n \lambda_\theta(i-i, s_0))), \end{aligned} \quad (11)$$

where  $a_i(\theta) := \prod_{k=I_0+1, k \neq i}^{I_{\text{crit}}} (\lambda_\theta(k, s_0) / (\lambda_\theta(k, s_0) - \lambda_\theta(i, s_0)))$ . Expression (11) can be numerically instable if it is implemented directly and  $I_{\text{crit}} - I_0$  is large or the parameters  $\lambda_\theta$  of the single exponential distributions do not differ much. In this case [30] provides a more stable implementation based on the matrix exponential (see [31]).

An  $\alpha$ -quantile  $b_\alpha(\theta)$  of the hypoexponential distribution can be computed implicitly by solving

$$F_{\Delta N_{\text{fut}}, \theta}(b_\alpha(\theta)) - \alpha = 0. \quad (12)$$

Hence, if the parameter  $\theta$  is known then

$$\mathbb{P} := [b_{\alpha/2}(\theta), b_{1-\alpha/2}(\theta)] \quad (13)$$

is a prediction interval for  $\Delta N_{\text{fut}}$  since  $P(\Delta N_{\text{fut}} \in \mathbb{P}) = 1 - \alpha$ .

However, the parameter  $\theta = (\theta_1, \theta_2)^T$  is not known in practice and has to be estimated from the data  $\Delta n_{\text{all}} := (\Delta n_{1,0}, \dots, \Delta n_{I_0,0}, \dots, \Delta n_{1,J}, \dots, \Delta n_{I_j,J})$  given by the experiments. A commonly used estimator for  $\theta$  is the maximum likelihood estimator:

$$\hat{\theta} \in \underset{\theta \in \Theta}{\text{argmax}} f_{\theta, \text{all}}(\Delta n_{\text{all}}), \quad (14)$$

where

$$f_{\theta, \text{all}}(\Delta n_{\text{all}}) := \prod_{j=0}^J \prod_{i=1}^{I_j} f_{\lambda_\theta(i, s_j)}(\Delta n_{i,j}) \quad (15)$$

is the density of the distribution of all data and  $f_\lambda(\Delta n) := \lambda \exp(-\lambda \Delta n)$  is the density of the exponential

distribution. The density  $f_{\theta, \text{all}}(\Delta n_{\text{all}})$  is given as the product of the single densities  $f_{\lambda_{\theta}(i, s_j)}(\Delta n_{i, j})$  because  $\Delta N_{1,0}, \dots, \Delta N_{I_0,0}, \dots, \Delta N_{1,J}, \dots, \Delta N_{I,J}$  are stochastically independent.

Having an estimator  $\hat{\theta}$  for  $\theta$ , the prediction of the time of the critical number  $I_{\text{crit}}$  of broken tension wires is

$$\Delta n_{1,0} + \dots + \Delta n_{I_0,0} + \frac{1}{\lambda_{\hat{\theta}}(I_0, s_0)} + \dots + \frac{1}{\lambda_{\hat{\theta}}(I_{\text{crit}} - 1, s_0)}. \quad (16)$$

If  $\theta$  is unknown, then the prediction interval for the future  $\Delta N_{\text{fut}}$  must depend on the available data  $\Delta n_{\text{all}}$  which is a realization of the random vector  $\Delta N_{\text{all}}$ . Hence, it is a function  $\mathbb{P}(\Delta n_{\text{all}})$  of  $\Delta n_{\text{all}}$  and it is an exact prediction interval if  $P_{\theta}(\Delta N_{\text{fut}} \in \mathbb{P}(\Delta N_{\text{all}})) \geq 1 - \alpha$  for all possible  $\theta$ . That means for different realizations  $\Delta n_{\text{all}}$  we get different prediction intervals. A naive prediction interval for  $\Delta N_{\text{fut}}$  is given by (see [9])

$$\mathbb{P} := [b_{\alpha/2}(\hat{\theta}), b_{1-\alpha/2}(\hat{\theta})], \quad (17)$$

where  $\hat{\theta}$  is the maximum likelihood estimator. This is an approximate  $(1 - \alpha)$ -prediction interval only for large sample sizes, because it does not include any information about the uncertainty of the estimation. For a small number of observations the coverage probability may differ drastically from  $1 - \alpha$  (see [9, p. 294]). We will analyze this in a simulation study in Section 5.

To include the uncertainty of the estimator  $\hat{\theta}$ , a confidence interval for  $\theta$  can be used. A  $(1 - \alpha)$ -confidence interval  $\mathbb{C}$  for  $\theta$  depends also on the available observation vector  $\Delta n_{\text{all}}$  and satisfies  $P(\theta \in \mathbb{C}(\Delta N_{\text{all}})) \geq 1 - \alpha$  for all  $\theta \in \Theta$ . A  $(1 - \alpha)$ -confidence set for  $\theta$  can be derived using a likelihood ratio test (see, e.g., [32, pp. 409]). It is given by

$$\hat{\mathbb{C}} := \left\{ \theta : -2 \log \left( \frac{f_{\theta, \text{all}}(\Delta n_{\text{all}})}{f_{\hat{\theta}, \text{all}}(\Delta n_{\text{all}})} \right) \leq \chi_{2, 1-\alpha}^2 \right\}, \quad (18)$$

if  $\chi_{2, 1-\alpha}^2$  is the  $(1 - \alpha)$ -quantile of the  $\chi^2$  distribution with 2 degrees of freedom, because we consider  $\theta = (\theta_1, \theta_2)$ ; that is, two parameters have to be estimated.

It is possible to use the  $(1 - \alpha)$ -confidence set  $\hat{\mathbb{C}}$  in expression (18) to include the uncertainty of the estimation. A  $(1 - 2\alpha)$ -prediction interval which is also valid for smaller sample sizes is then given by

$$\mathbb{P} := \bigcup_{\theta \in \hat{\mathbb{C}}} [b_{\alpha/2}(\theta), b_{1-\alpha/2}(\theta)] \subset \left[ \min_{\theta \in \hat{\mathbb{C}}} b_{\alpha/2}(\theta), \max_{\theta \in \hat{\mathbb{C}}} b_{1-\alpha/2}(\theta) \right]; \quad (19)$$

that is, for all  $\theta \in \hat{\mathbb{C}}$  the corresponding quantiles of the hypoexponential distribution are computed. The minimum over all lower quantiles  $b_{\alpha/2}$  and the maximum over all upper quantiles  $b_{1-\alpha/2}$  are then the desired  $1 - 2\alpha$  prediction interval for  $\Delta N_{\text{fut}}$ .

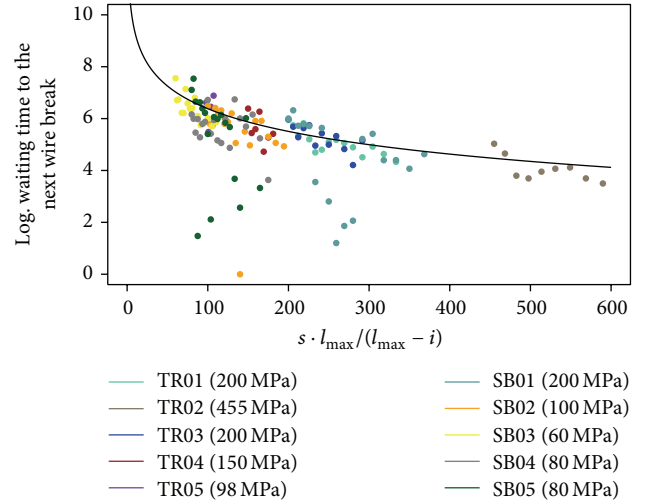


FIGURE 4: Fitted expectation of the logarithmized waiting times using the Basquin link function.

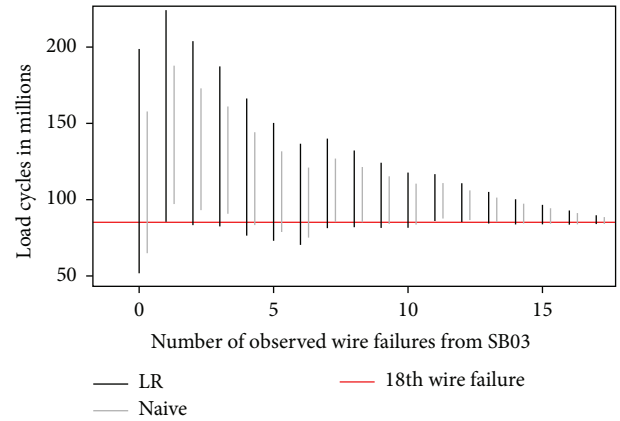


FIGURE 5: 90% prediction intervals based on the likelihood ratio and the naive method for the 18th wire failure of SB03 with different number of used previous failures from the same beam and all data from the other nine experiments.

## 5. Results

We now apply the proposed methods to the data from the ten experiments described in Section 2. Figure 4 shows the fitted expectation of the logarithmized waiting times when the Basquin link function from Section 3 is used. The relation between the increasing stress on the gradually breaking wires and the waiting time is adequately modeled by this function as it tends to infinity for a stress near 0 and fits the majority of observed waiting times. For the comparison of the two prediction methods, we use the beam SB03 as an example, because with an initial stress range of 60 MPa it is the most interesting one for real applications. In this experiment 18 wire breaks could be observed until the complete failure of the beam. The time of this 18th failure can be predicted if the corresponding observation is removed from the dataset.

In Figure 5, 90% prediction intervals for this last wire break are shown where a different number of previous broken

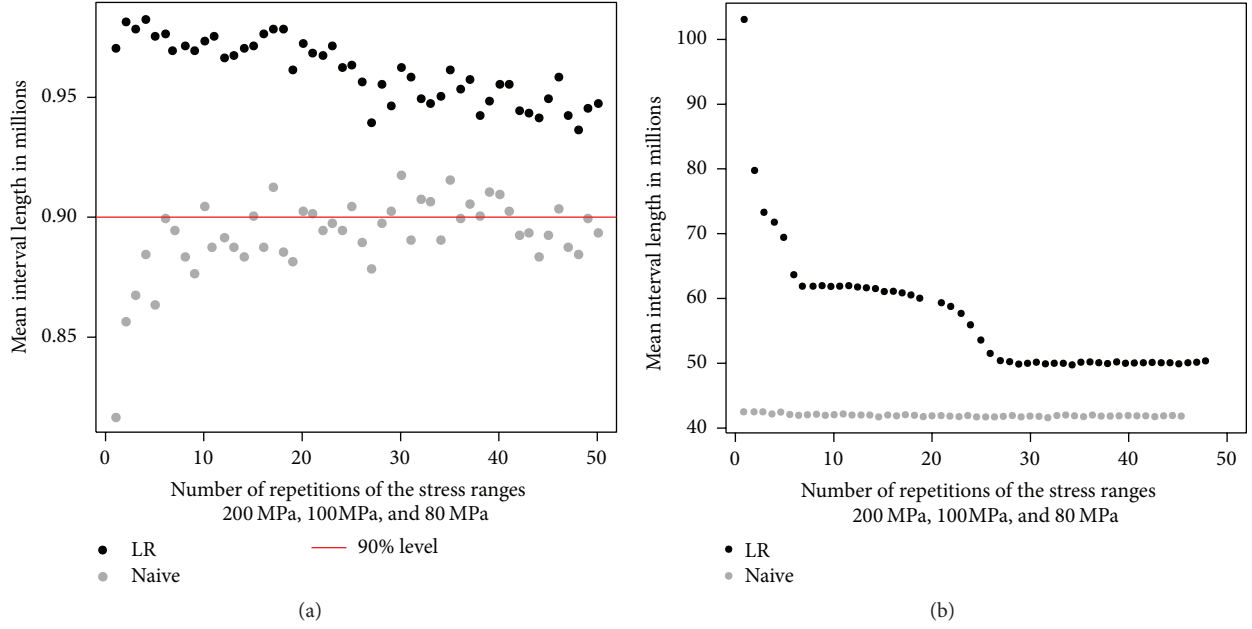


FIGURE 6: Coverage rates (a) and mean interval lengths (b) of the 90% prediction intervals using the likelihood ratio and the naive approach.

wires from the same experiment and all observations from the other experiments are used. The fewer observations from SB03 are used, the more wire failures have to be predicted. Hence, the prediction intervals are larger and get smaller when less breakages are predicted. The naive intervals are always smaller than the ones based on the likelihood ratio approach but the true time of the beam's complete failure is not always covered by the naive intervals, where this is only once the case for the likelihood ratio method. It is obvious that the prediction task is simpler when less wire breaks have to be predicted.

To further check the performance of the two proposed prediction methods, we consider a simulation study. For this, we consider three experiments with initial stress ranges  $s_1 = 200$  MPa,  $s_2 = 100$  MPa, and  $s_3 = 80$  MPa. Six wire breaks are simulated for each of the three experiments by using the Basquin link function:

$$\lambda_{\theta}(i, s) := \exp\left(-\theta_1 + \theta_2 \log\left(s \cdot \frac{I_{\max}}{I_{\max} - i}\right)\right), \quad (20)$$

with  $I_{\max} = 35$  and  $\theta = (28.163551, 2.922285)^{\top}$ , which is the maximum likelihood estimator from the real data of the SFB project.

Furthermore, we generate three wire failures of an additional experiment with  $s_0 = 60$  MPa. For this additional beam, the time of the sixth wire break is predicted using only the first three failure times. This is done with 90% prediction intervals via the naive and the likelihood ratio approach. Hence, in this first scenario there are  $n_1 = 21$  observations to estimate the parameter  $\theta$  and to compute the 95% confidence set based on the likelihood ratio test. The sample size is then subsequently increased by sampling repetitions of the first three experiments, so that all scenarios have  $J_l = l \cdot 18 + 3$

observations for  $l = 1, \dots, 50$ . This results in a maximum considered sample size of  $J_{50} = 903$ .

For each scenario, we check if the simulated time of the sixth breakage which has been removed before the estimation is covered by the two prediction intervals and compare the lengths of the intervals. This procedure is replicated 1000 times for each scenario to get meaningful estimations of the coverage rates and the interval lengths.

Figure 6(a) shows the coverage rate over the 1000 replications. It can be seen that for small sample sizes the naive method does not provide a valid prediction interval as the coverage rate is much lower than 90%. With increasing sample size, the coverage rate is converging to 90% though. The likelihood ratio approach leads to valid prediction intervals even for a very small number of observations but the resulting intervals are conservative and tend towards a 95% coverage rate instead of 90%. The intervals based on the confidence sets are always larger than for the naive method because it uses the quantiles  $b_{0.025}(\tilde{\theta})$  and  $b_{0.975}(\tilde{\theta})$  with  $\tilde{\theta} \in \hat{\mathbb{C}}$ , whereas the naive interval uses the smaller quantiles  $b_{0.05}(\hat{\theta})$  and  $b_{0.95}(\hat{\theta})$  based on the maximum likelihood estimator  $\hat{\theta}$ . With increasing sample size, the  $(1 - \alpha)$ -confidence set  $\hat{\mathbb{C}}$  becomes smaller until it only contains the maximum likelihood estimator. In this case the 90% interval based on the likelihood ratio confidence set coincides with the naive 95% prediction interval.

The average lengths of the 1000 prediction intervals for all considered scenarios are depicted in Figure 6(b). For small sample sizes the prediction intervals based on the confidence sets are much larger than the naive ones but they get smaller when the number of observations is increased. In Scenario  $i = 27$  with 489 observations and all following ones the confidence sets only consist of the maximum likelihood estimator. Hence, the average length of the intervals cannot

decrease further. Since the naive prediction interval only depends on the maximum likelihood estimator, the average lengths do not vary much for this method in the simulation study.

Summarizing the results of the simulation study, it was shown that for small sample sizes the naive method leads to invalid prediction intervals with too low coverage rates. In this situation the approach based on confidence sets using likelihood ratio tests can be used. For moderate and large samples, the naive prediction intervals are valid though. The prediction intervals based on the confidence sets tend to be conservative as their coverage rate was always above the chosen level of 90%. However, in praxis there oftentimes are only a few experiments due to the immense costs in time and material, so that the confidence set based method is nevertheless a plausible choice.

## 6. Conclusion

The two proposed methods for predicting the failure time of prestressed concrete beams are based on predicting the time when a critical number of tension wires is broken. One method is a naive method using only the maximum likelihood estimator. The other method uses confidence sets given by the likelihood ratio test. Both methods are based on the waiting times between successive breakages of wires. This is possible since the time points can be measured quite precisely with a microphone. Using all available waiting times increases the number of observations substantially which is in particular important when only few experiments with concrete beams can be conducted. Since the number of observations is increased, reasonable prediction intervals can be derived which provide the uncertainty of the prediction. Although a quite simple model of the dependence of the waiting times on the number of tension wires is used, it is shown that both methods provide reasonable results using ten experiments with concrete beams. A simulation study however shows that the naive method should be used with caution if the number of observations is low. The simple model which was used does not take into account any damage accumulation. To include damage accumulation, the waiting times should depend on the waiting times observed before and should have a Weibull distribution with increasing hazard rate. However, it is up to now unclear how to get the estimators, predictors, and prediction intervals then, since the independence of the waiting times is not satisfied anymore.

## Competing Interests

The authors declare that there are no competing interests regarding the publication of this paper.

## Acknowledgments

The research was supported by the Collaborative Research Center SFB 823 Statistical Modeling of Nonlinear Dynamic Processes.

## References

- [1] R. Z. Al-Zaid and A. S. Nowak, "Fatigue strength of prestressed concrete girder bridges," *Canadian Journal of Civil Engineering*, vol. 15, no. 2, pp. 199–205, 1988.
- [2] C. Higgins, W. C. Farrow III, B. S. Nicholas, and T. Potisuk, "High-cycle fatigue of diagonally cracked reinforced concrete bridge girders: field tests," *Journal of Bridge Engineering*, vol. 11, no. 6, pp. 699–706, 2006.
- [3] G. Magnel, *Theorie und Praxis des Spann-Betons*, Bauverlag, 3rd edition, 1956.
- [4] T. R. Overman and J. E. Breen, "Fatigue behavior of pretensioned concrete girders," Tech. Rep., University of Texas, Austin, Tex, USA, 1984.
- [5] C. Rao and G. C. Frantz, "Fatigue tests of 27-year-old prestressed concrete bridge box beams," *PCI Journal*, vol. 41, no. 5, pp. 74–83, 1996.
- [6] A. Carpinteri, A. Spagnoli, and S. Vantadori, "Mechanical damage of ordinary or prestressed reinforced concrete beams under cyclic bending," *Engineering Fracture Mechanics*, vol. 72, no. 9, pp. 1313–1328, 2005.
- [7] G. Heeke, *Untersuchung zur Ermüdungsfestigkeit von Betonstahl und Spannstahl im Zeit- und Dauerhaftigkeitsbereich mit sehr hohen Lastwechselzahlen [Ph.D. thesis]*, Technical University of Dortmund, Dortmund, Germany, 2016.
- [8] J. K. Patel, "Prediction intervals—a review," *Communications in Statistics: Theory and Methods*, vol. 18, no. 7, pp. 2393–2465, 1989.
- [9] W. Q. Meeker and L. A. Escobar, *Statistical Methods for Reliability Data*, John Wiley & Sons, New York, NY, USA, 1998.
- [10] H. Goual and N. Seddik-Ameur, "Chi-squared type test for the AFT-generalized inverse Weibull distribution," *Communications in Statistics—Theory and Methods*, vol. 43, no. 13, pp. 2605–2617, 2014.
- [11] W. Q. Meeker, L. A. Escobar, and C. J. Lu, "Accelerated degradation tests: modeling and analysis," *Technometrics*, vol. 40, no. 2, pp. 89–99, 1998.
- [12] V. R. B. De Oliveira and E. A. Colosimo, "Comparison of methods to estimate the time-to-failure distribution in degradation tests," *Quality and Reliability Engineering International*, vol. 20, no. 4, pp. 363–373, 2004.
- [13] X. Wang and D. Xu, "An inverse Gaussian process model for degradation data," *Technometrics*, vol. 52, no. 2, pp. 188–197, 2010.
- [14] D. L. Snyder and M. I. Miller, *Random Point Processes in Time and Space*, Springer, New York, NY, USA, 2nd edition, 1991.
- [15] K. Sobczyk and J. Spencer, *Random Fatigue. From Data to Theory*, Academic Press, Boston, Mass, USA, 1992.
- [16] M. Sánchez-Silva and G.-A. Klutke, *Reliability and Life-Cycle Analysis of Deteriorating Systems*, Springer Series in Reliability Engineering, Springer, Heidelberg, Germany, 2016.
- [17] E. Cramer and U. Kamps, "Sequential order statistics and  $\kappa$ -out-of- $n$  systems with sequentially adjusted failure rates," *Annals of the Institute of Statistical Mathematics*, vol. 48, no. 3, pp. 535–549, 1996.
- [18] M. Burkschat, "Systems with failure-dependent lifetimes of components," *Journal of Applied Probability*, vol. 46, no. 4, pp. 1052–1072, 2009.
- [19] E. A. Peña, E. H. Slate, and J. R. González, "Semiparametric inference for a general class of models for recurrent events," *Journal of Statistical Planning and Inference*, vol. 137, no. 6, pp. 1727–1747, 2007.

- [20] K. W. Fertig, M. E. Meyer, and N. R. Mann, "On constructing prediction intervals for samples from a Weibull or extreme value distribution," *Technometrics*, vol. 22, no. 4, pp. 567–573, 1980.
- [21] M. Engelhardt and L. J. Bain, "Prediction intervals for the weibull process," *Technometrics*, vol. 20, no. 2, pp. 167–169, 1978.
- [22] M. Engelhardt and L. J. Bain, "On prediction limits for samples from a weibull or extreme-value distribution," *Technometrics*, vol. 24, no. 2, pp. 147–150, 1982.
- [23] J. Frey, "Prediction bands for the EDF of a future sample," *Journal of Statistical Planning and Inference*, vol. 142, no. 2, pp. 506–515, 2012.
- [24] J. F. Lawless and M. Fredette, "Frequentist prediction intervals and predictive distributions," *Biometrika*, vol. 92, no. 3, pp. 529–542, 2005.
- [25] K. Krishnamoorthy, Y. Lin, and Y. Xia, "Confidence limits and prediction limits for a Weibull distribution based on the generalized variable approach," *Journal of Statistical Planning and Inference*, vol. 139, no. 8, pp. 2675–2684, 2009.
- [26] C. Xiong and G. A. Milliken, "Prediction for exponential lifetimes based on step-stress testing," *Communications in Statistics—Simulation and Computation*, vol. 31, no. 4, pp. 539–556, 2002.
- [27] R. Maurer, G. Heeke, and G. Marzahn, "Fatigue strength of prestressing steel tendons embedded in concrete of an aged highway bridge/Ermüdungsfestigkeit der Spannstähle einer Autobahnbrücke von 1957 im einbetonierten Zustand," *Bauingenieur*, vol. 87, no. 5, pp. 226–236, 2012.
- [28] O. Basquin, "The exponential law of endurance tests," Tech. Rep., ASTM, Philadelphia, Pa, USA, 1910.
- [29] S. M. Ross, *Introduction to Probability models*, Elsevier/Academic Press, Amsterdam, The Netherlands, 11th edition, 2014.
- [30] I. Gertsbakh, E. Neuman, and R. Vaisman, "Monte Carlo for estimating exponential convolution," *Communications in Statistics. Simulation and Computation*, vol. 44, no. 10, pp. 2696–2704, 2015.
- [31] Z. I. Botev, P. L'Ecuyer, G. Rubino, R. Simard, and B. Tuffin, "Static network reliability estimation via generalized splitting," *INFORMS Journal on Computing*, vol. 25, no. 1, pp. 56–71, 2013.
- [32] A. M. Mood, F. A. Graybill, and D. C. Boes, *Introduction to the Theory of Statistics*, McGraw-Hill, New York, NY, USA, 3rd edition, 1974.

## Research Article

# On the Tensile Strength of Granite at High Strain Rates considering the Influence from Preexisting Cracks

Mahdi Saadati,<sup>1,2</sup> Pascal Forquin,<sup>3</sup> Kenneth Weddfelt,<sup>2</sup> and Per-Lennart Larsson<sup>1</sup>

<sup>1</sup>Department of Solid Mechanics, KTH Royal Institute of Technology, 10044 Stockholm, Sweden

<sup>2</sup>Atlas Copco, 70225 Örebro, Sweden

<sup>3</sup>3SR Laboratory, Grenoble-Alpes University, 38041 Grenoble, France

Correspondence should be addressed to Per-Lennart Larsson; pelle@half.kth.se

Received 4 February 2016; Accepted 14 June 2016

Academic Editor: Konstantinos I. Tserpes

Copyright © 2016 Mahdi Saadati et al. This is an open access article distributed under the Creative Commons Attribution License, which permits unrestricted use, distribution, and reproduction in any medium, provided the original work is properly cited.

The dynamic tensile behavior of granite samples, when some preexisting cracks are introduced artificially, is investigated. Spalling tests using a Hopkinson bar are performed and strain rates of  $\sim 10^2$  1/s are obtained in both specimen types (with and without initial cracks). This experimental technique is employed being of the same order as strain rates in rock materials during percussive drilling, the application of interest here. The dynamic tensile responses of both sample-sets are compared using the velocity profile measured on the free-end of the sample. Furthermore, an anisotropic damage model based on the concept of obscuration probability describes the response without preexisting cracks. Here, a term of cohesive strength in obscuration zones is added to accurately handle the softening behavior of the material in tension. Results from the spalling tests are used to validate the model prediction of the dynamic tensile strength and also to calibrate the cohesive model parameters. Damaged elements are numerically introduced in the finite element calculations simulating the spalling experiments performed on predamaged samples. The results are compared with the experimental ones. Good agreement is obtained showing that a two-scale approach may constitute a suitable method to simulate numerically the tensile response of predamaged granite.

## 1. Introduction

The strain rate dependency of the mechanical response in brittle materials has been widely investigated in the literature. Considerable rate dependency is reported especially in the case of tensile strength [1–4]. There exists a threshold level of strain rate beyond which the tensile strength increases by increasing the strain rate. This threshold level is explained to be connected to the size of heterogeneity in the material [1, 5] and material defects size, population, and distribution [6, 7]. Direct tension test with split-Hopkinson bar (SHB) has been used to study the tensile strength for strain rates between  $10^{-1}$  and  $10^1$  1/s [3, 8]. In some cases, indirect tensile strength is measured by means of a Brazilian disc together with split-Hopkinson pressure bar (SHPB) apparatus [9, 10]. Inspired from the classical SHPB method, spalling test with Hopkinson bar is a suitable technique to measure the tensile strength of brittle materials at strain rates between  $10^1$  and  $10^2$  1/s [2, 4]. The main idea in this test is that the impact of the projectile

induces a compressive wave that propagates through the bar and is mainly transferred to the specimen. This wave is reflected as a tensile wave from the free surface of the specimen that leads to damaging of the material.

There is a wide range of applications pertinent to the dynamic tensile behavior of brittle materials from blasting in open quarries and concrete structures exposed to impact loading to screen rupture of cell phones due to free fall. Percussive drilling, which is the application of interest in this investigation, is just one of them. The main goal in this work is to develop a reliable numerical tool for simulating the rock fragmentation mechanism during percussive drilling. In modeling such problems, a constitutive model is needed to cover both the tensile behavior of the brittle materials at high strain rate, because of the rapid indentation, and also confined compression behavior that occurs underneath the indenter. The Krieg, Swenson, and Taylor- [11, 12] (KST-) Denoual, Forquin, and Hild [6, 7] (DFH) model is adopted to perform such analysis. This material model is composed of a

plasticity model (KST) to simulate the compressive behavior of geomaterials accounting for the effect of hydrostatic and deviatoric parts of the stress tensor. Also the fragmentation process in tensile loading, due to the opening of cracks, is defined by using an anisotropic damage model (DFH). This model is based on a probabilistic approach describing the dynamic fragmentation of the brittle materials. It should be mentioned that the original DFH model (with no cohesion strength in obscuration zones) enables predicting the dynamic tensile strength of the brittle materials, and the main model parameters are obtained from a set of quasi-static experiments [6, 7]. Saadati et al. [13, 14] applied the KST-DFH model on granite and investigated the rock fragmentation process and the force-penetration response at percussive drilling. The KST-DFH model parameters for Bohus granite have been determined based on previously reported experimental results [15]. It was shown that preexisting cracks in granite have a significant effect on its mechanical response and the fracture pattern at impact loading.

Spalling tests are performed to investigate the dynamic tensile behavior of Bohus granite. As the DFH model predicts the dynamic tensile strength of the brittle materials at high strain rates, this work can be seen as a validation step for the model prediction of the granite tensile strength. The strain rate in the rock during the percussive drilling process is in order of  $10^2$  1/s based on previous numerical simulations [13]. This is the same order as the strain rates in the rock material during the spalling tests with Hopkinson bar performed in this investigation and therefore makes the spalling experiment an appropriate tool to verify the rate dependency of the material response at dynamic tensile loading. Furthermore, a cohesive strength is added to the original DFH model [16, 17] to more accurately deal with the postpeak behavior of the material at tensile loading. Hence the results from the spalling tests are used to calibrate the cohesive model parameters in a dynamic situation.

The experimental results from the spalling tests on Bohus granite are presented. The dynamic tensile strength of the material (without preexisting cracks) is measured and compared with the quasi-static results. When there are cracks in the specimens that are introduced in addition to the material default cracks and defects, called structural cracks in this work, the material response changes considerably. The effect of the structural cracks on the mechanical response and the fracture pattern in Edge-On Impact (EOI) tests, that is, impact of an aluminum projectile onto a rock slab, was previously studied [13, 14]. When it comes to drilling application, these cracks can be introduced in the rock during drilling due to either former impact of the drill bit or use of methods such as microwave and laser. It was shown that the preexisting structural cracks facilitate the drilling process regardless of their orientation [14]. In order to investigate the effect of these cracks on the dynamic tensile response of the material, some of the spalling specimens were exposed to coarser mechanical loading during the cutting process in order to introduce new cracks to the material. In the present work spalling tests have been performed also on such specimens with preexisting structural cracks and it is shown that the dynamic tensile behavior changes considerably. Numerical modeling of the

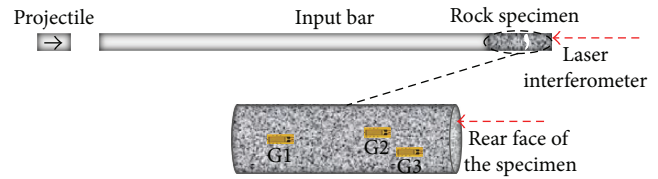


FIGURE 1: Spalling experiment setup with Hopkinson bar.

spalling tests is performed and the results are compared with the experimental ones. The DFH model together with a cohesive strength is used for this purpose. The cohesive model parameters are calibrated based on the experimental results performed on granite without preexisting cracks. In the case of specimens with preexisting structural cracks, these cracks are introduced to the numerical samples by means of sets of predamaged finite elements randomly distributed in the sample. It is shown that the numerical results are in good agreement with the experimental ones.

## 2. Experimental Investigation and Results Pertinent to the Tensile Strength of Granite at High Strain Rates

**2.1. Experimental Setup with Hopkinson Bar.** Spalling test with Hopkinson bar is suggested as a suitable technique to measure the tensile strength of brittle materials at strain rates between  $10^1$  and  $10^2$  1/s [2, 4]. As is stated before, the numerical modeling of percussive drilling that was previously performed in [13] gives the tensile strain rates in the rock in order of  $10^2$  1/s. It should be mentioned that, in order to obtain this tensile strain rate from the numerical simulation of percussive drilling, the maximum positive principal stress was used from the simulation with only the KST plasticity model (in order to evaluate the level of tensile strain rate in a finite element without influence from damage).

Accordingly, the spalling test with Hopkinson bar is an appropriate method to investigate the dynamic tensile behavior of the material in the interesting range of strain rates pertinent to percussive drilling. The experimental setup used in this work is shown in Figure 1. It consists of a Hopkinson bar made of high-strength aluminum, an aluminum projectile with a spherical cap-end, which is optimized to induce more homogenous tensile stress [4], and the rock sample that is well attached to the bar to increase the wave transmission. The rock specimen is instrumented with strain gauges to record the strain data and also a laser interferometer is directed toward the free surface of the specimen to measure the rear face velocity. The main idea is that the impact of the projectile induces a compressive pulse that travels along the bar and is mainly transferred to the rock specimen. When the compressive wave reaches the free surface of the sample, it is reflected as a tensile wave that propagates in the opposite direction and leads to failure if the tensile strength of the material is passed. Using the laser velocity profile, one can obtain the dynamic tensile strength of the material from the

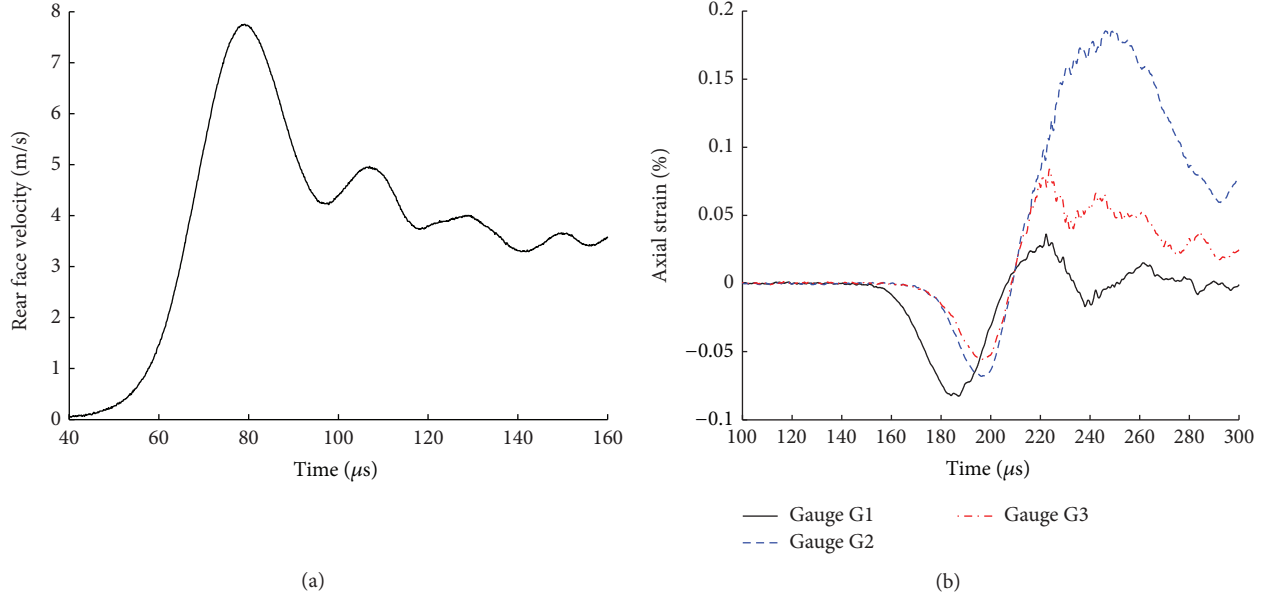


FIGURE 2: Spalling test results for a specimen without preexisting cracks. Rear face velocity profile from the laser (a) and strain data from the three strain gauges (b).

Novikov formula [18] assuming a linear-elastic behavior of the tested material prior to the peak strength.

**2.2. Spalling Test on Granite.** The results from the spalling tests are presented in this section. A typical result for both the rear face velocity (obtained from the laser) and the strain data (obtained from the strain gauges) is shown in Figure 2. Three strain gauges (G1, G2, and G3) of length 20 mm are placed at a distance of 116 mm, 45 mm, and 35 mm from the rear face of the specimen, respectively. The projectile impact velocity in this case was 7.3 m/s. Based on the Novikov et al. [18] approach, one can relate the dynamic tensile strength of the material to the pullback velocity (the difference between the maximum speed and the speed corresponding to rebound; see Figure 2) assuming a linear-elastic behavior of the material before reaching the tensile ultimate strength:

$$\sigma_{\text{dyn}} = \frac{1}{2} \rho C_0 \Delta V_{\text{pb}}, \quad (1)$$

where  $\rho = 2660 \text{ kg/m}^3$  is the density,  $C_0 = 4050 \text{ m/s}$  is the one-dimensional wave velocity in the material, and  $\Delta V_{\text{pb}} = 3.5 \text{ m/s}$  is the pullback velocity. A dynamic tensile strength of 18.9 MPa is obtained (the strain rate is about 70 1/s) in this test using the Novikov et al. [18] approach. The quasi-static tensile strength of the specimen with the same size is reported as about 8 MPa [15].

Furthermore, the nominal stress level ( $E\varepsilon$ ) obtained from the incident wave data at strain gauge G1 is shifted in the time direction and compared to the one from the rear face velocity data using (1); see Figure 3. The results are very close in the prepeak and early postpeak regions which indicate that the assumption of linear-elastic behavior before damage initiation is valid. This assumption can be further validated

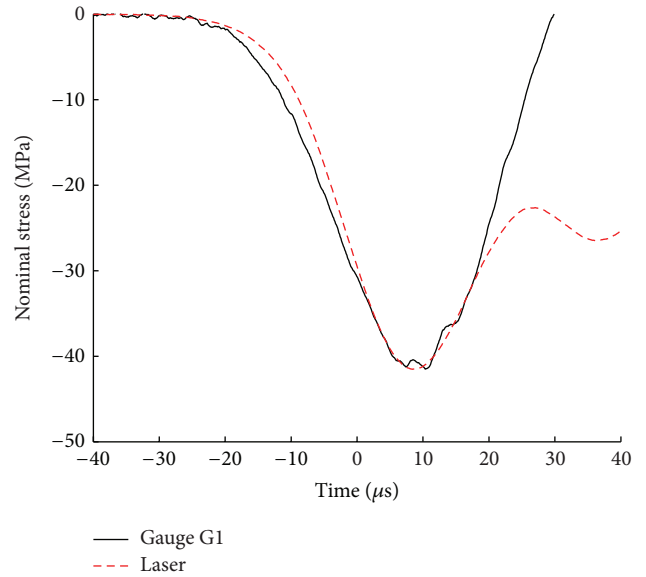


FIGURE 3: Nominal stress obtained from gauge G1 ( $E\varepsilon$ ) and based on rear face velocity ( $(1/2)\rho C_0 V$ ) in a specimen without preexisting cracks.

by looking at the stress-strain data obtained earlier from the flexural test on the material [15].

**2.3. Effect of Preexisting Structural Cracks on the Results.** The effect of the preexisting cracks on the mechanical response and the fracture pattern in Edge-On Impact (EOI) tests, that is, impact of an aluminum projectile onto a rock slab, was previously studied [13, 14]. In order to investigate the effect of these cracks on the dynamic tensile response of the material, some of the spalling specimens were subjected to coarser

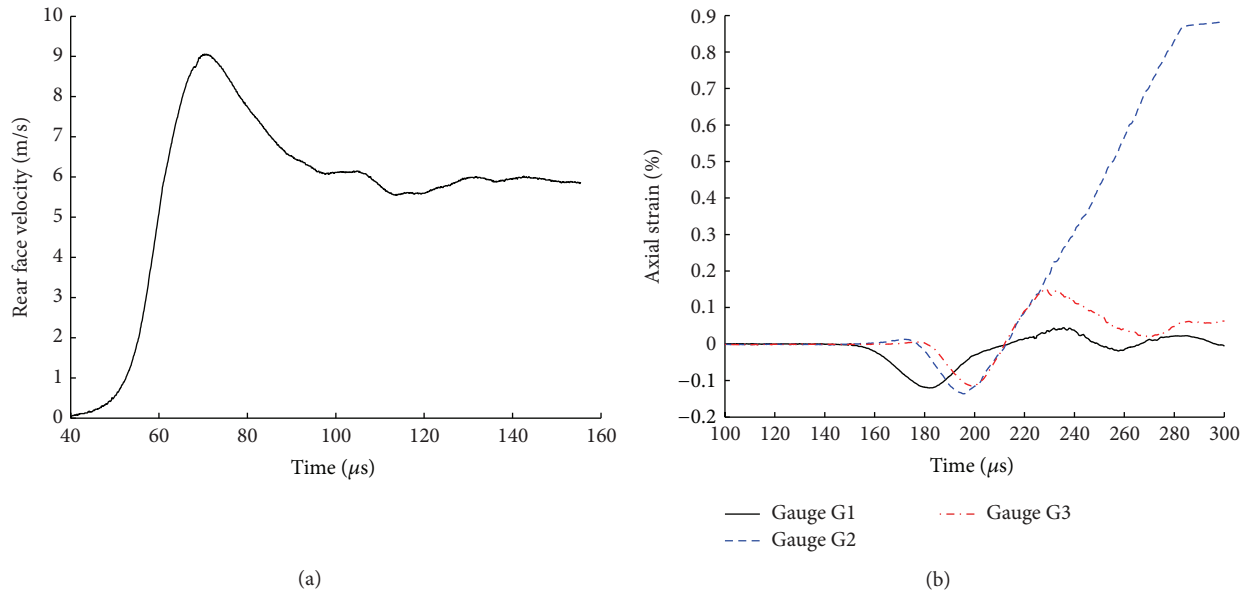


FIGURE 4: Spalling test results for a specimen with preexisting structural cracks. Rear face velocity from the laser (a) and strain data from the three strain gauges (b).

mechanical loading during the cutting process. This introduced new cracks in the specimens in addition to the cracks and defects that are present in the material by default. These newly introduced cracks in the specimen are hereafter called structural cracks as they are not part of an intact material. To quantify the amount of these cracks, one can perform, for example, quasi-static tensile test and measure the effective stiffness reduction of the specimen. Quasi-static tensile tests were performed on some of the samples and average effective stiffness of about 30 GPa was obtained instead of 52 GPa that is the average effective stiffness of the intact specimens.

When preexisting structural cracks are present in the specimen, the dynamic response of the material during a spalling test changes considerably. A typical result of the spalling test with preexisting structural cracks is shown in Figures 4 and 5. Strain gauges G1 ( $L = 20$  mm), G2 ( $L = 30$  mm), and G3 ( $L = 20$  mm) are placed in a distance of 120 mm, 61 mm, and 41 mm from the rear face of the specimen, respectively. The projectile impact velocity in this case was 8.0 m/s and the specimen density and 1D wave speed were  $\rho = 2671$  kg/m<sup>3</sup> and  $C_0 = 4400$  m/s, respectively. There are three main differences in these results compared to the intact specimen presented in the previous section. First, in the prepeak region (see Figure 5, region I), the structural cracks in the material are partly closed when the compressive stress travels through the specimen leading to slightly larger difference between gauge G1 and rear face velocity (converted into stress level in Figure 5) contrary to the case of an intact specimen. This is mainly due to nonlinear material behavior in compression that is related to presence of the structural cracks. Secondly, in the early postpeak region (see Figure 5, region II), the nominal stress level obtained from the incident wave at gauge G1 (calculated as  $E\varepsilon$ ) is not close to the one obtained from the rear face velocity (calculated as  $(1/2)\rho C_0 V$ ). It is most probably due to the fact that

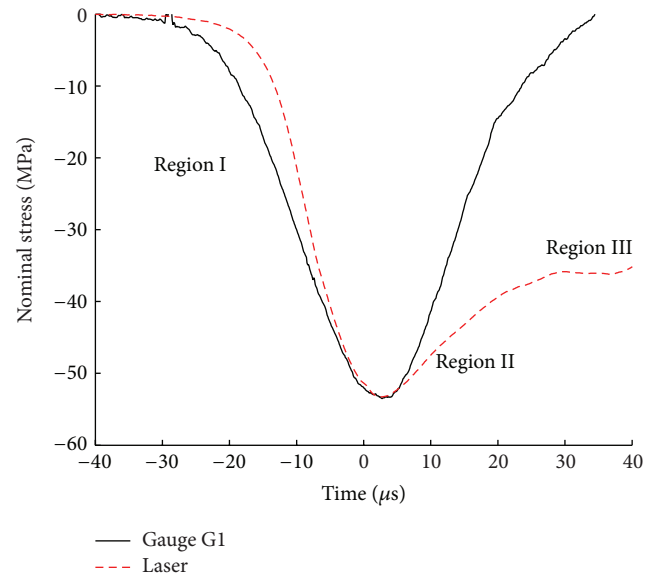


FIGURE 5: Nominal stress obtained from gauge G1 ( $E\varepsilon$ ) and based on rear face velocity ( $(1/2)\rho C_0 V$ ) in a specimen with preexisting structural cracks.

the reflected incident wave from the free surface of the specimen experiences some partial reflection when it reaches the surfaces of the structural cracks. It also indicates that the Novikov linear-elastic assumption is not valid in this case. Thirdly in the postpeak region of rear face velocity (Figures 4(a) and 5, region III), the rebound phenomenon is not seen or is negligible in these specimens and the rear face velocity curve is more plateau-like in this section. This is most probably due to the fact that when rebounding should occur due to generated waves from initiated final fracture

planes, the waves are blocked between the structural cracks and cannot reach the free surface. Accordingly, the structural cracks generate a damping effect in this case that prevents the rebounding phenomenon.

It should be mentioned that the measurement from gauge G2 seems to be extremely high in the tensile part. The reason for this could be that this gauge was glued near one of the structural cracks in which the tensile axial strain gets locally large. The pullback velocity in this test is  $\Delta V_{pb} = 3.0$  m/s and a dynamic tensile strength of 17.4 MPa is obtained (the strain rate is about 100 1/s) if one uses the Novikov et al. approach [18]. However, it should be mentioned that the Novikov et al. approach [18] is invalid in this case as the tensile behavior prior to the ultimate stress is not linear-elastic.

### 3. Numerical Modeling

**3.1. Constitutive Model and Results.** The fragmentation process in brittle materials exposed to dynamic loading, with particular application to percussive drilling, is of most interest in this investigation. The stress state in the material beneath the drilling tool consists of both compressive and tensile stresses. It is well known that brittle materials such as rocks behave differently in compression and tension. Therefore the constitutive model for these materials, to account for such types of phenomena, should include this difference and should be able to distinguish between the two different stress sign dependent responses. For this reason and based on a previous investigation [13], the KST-DFH constitutive model is selected to deal with the fragmentation modeling in brittle materials due to dynamic loading.

The KST-DFH material model is composed of two separate parts in order to deal with both compressive and tensile responses of the material. A plasticity model (KST) is employed to simulate the compressive behavior of geomaterials accounting for the effect of hydrostatic and deviatoric parts of the stress tensor. The fragmentation process, due to the opening of cracks, is defined by using a damage model (DFH), which is explained in detail in [6, 7]. In the spalling test, however, the level of compressive stresses is not high enough to induce any plastic deformation. Therefore the main emphasis in this investigation with spalling tests is to validate the DFH part of the constitutive model that deals with the dynamic tensile behavior of the material.

In the DFH model, defects with different sizes and orientations are assumed to be randomly distributed within the brittle material. Under static loading the weakest defect is triggered leading to a rapid failure of the sample. Consequently the failure stress is a random variable. Accordingly, a probabilistic approach may be employed to explain the material response to tensile loading at high strain rates. The weakest link theory and Weibull model are adopted as a framework for the damage model [7, 19, 20]. The model covers the tensile behavior of brittle materials from low to high loading rates. At low loading rate conditions, the fracture process is generally the consequence of the initiation and growth of a single crack. This single crack is created from the activation and propagation of the weakest defect in the material. Therefore a Weibull model is adopted to explain this probabilistic response at

low loading rates. Using a Poisson point-process framework, the weakest link assumption, and a Weibull model, the failure probability  $P_F$  is given by

$$P_F = 1 - \exp[-Z_{\text{eff}}\lambda_t(\sigma_F)], \quad (2)$$

where  $Z_{\text{eff}}$  is the effective volume [21] and  $\lambda_t$  is the initiation density defined by

$$\lambda_t(\sigma_F) = \lambda_0 \left( \frac{\sigma_F}{S_0} \right)^m, \quad (3)$$

where  $m$  is the Weibull modulus,  $S_0^m/\lambda_0$  is the Weibull scale parameter, and  $\sigma_F$  is the maximum principal stress in the whole domain. The effective volume,  $Z_{\text{eff}}$ , is expressed as

$$Z_{\text{eff}} = ZH_m, \quad (4)$$

where  $Z$  is the size of the whole volume and  $H_m$  the stress heterogeneity factor [22] written as

$$H_m = \frac{1}{Z} \int_{\Omega} \left( \frac{\langle \sigma_1 \rangle}{\sigma_F} \right)^m dZ, \quad \text{when } \sigma_F > 0. \quad (5)$$

In (5),  $\sigma_1$  is the local maximum principal stress and  $\langle \bullet \rangle$  Macaulay's brackets. The stress heterogeneity factor characterizes the effect of the load pattern on the cumulative failure probability. Last, the average failure stress  $\sigma_w$  and the corresponding standard deviation  $\sigma_{sd}$  are written as

$$\sigma_w = S_0 (\lambda_0 ZH_m)^{-1/m} \Gamma\left(1 + \frac{1}{m}\right), \quad (6)$$

$$\sigma_{sd} = S_0 (\lambda_0 ZH_m)^{-1/m} \sqrt{\Gamma\left(1 + \frac{2}{m}\right) - \Gamma^2\left(1 + \frac{1}{m}\right)}, \quad (7)$$

where  $\Gamma$  is the Euler function of the second kind

$$\Gamma(1+x) = \int_0^{\infty} \exp(-u) u^x du. \quad (8)$$

Under high strain rate conditions, such as the situation during a spalling test, several cracks are initiated and propagate from the initial defects leading to multiple fragmentation. In that case, while the weakest defect is activated and the resulting crack propagates, several other cracks are initiated during this time. In contrast to the low loading rate conditions that characterize the fracture process in general (with the consequence of the initiation and growth of a single crack leading to fracture of the whole structure), when the loading rate is high there is enough time for the stress to reach high levels and activate smaller (or stronger) defects. When a crack is propagating at a very high velocity (a portion of the stress wave velocity), it relaxes the stresses in its vicinity. The multiple fragmentation process with multiple cracks growing at the same time stops when the whole structure is covered by these relaxed stress regions (see Figure 6).

The interaction law between cracks already initiated and the critical defects of the material is given by the concept of probability of nonobscuration  $P_{no}$  [6, 7]. In the case of multiple fragmentations, the interaction between the horizon (the

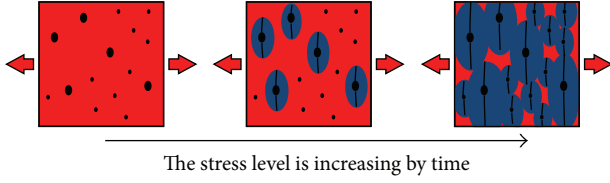


FIGURE 6: Obscuration phenomenon and multiple fragmentation process.

region around a crack where stresses are relaxed due to crack opening) and the boundary of the domain  $\Omega$  is small and if a uniform stress field is assumed, the obscuration probability  $P_o$  is written as [6]

$$\begin{aligned} P_o(T) &= 1 - P_{no}(T) \\ &= 1 - \exp\left(-\int_0^T \frac{d\lambda_t}{dt} [\sigma(t)] Z_o(T-t) dt\right). \end{aligned} \quad (9)$$

In (9),  $Z_o$  is the obscured zone,  $\sigma$  the local eigenstress component,  $T$  the current time, and  $t$  the crack initiation time. The probability of obscuration is defined for each eigendirection  $i$  and the change of  $P_{oi}$  is expressed in differential form, in order to be employed in an FE code using (9), as

$$\begin{aligned} \frac{d^2}{dt^2} \left( \frac{1}{1 - P_{oi}} \frac{dP_{oi}}{dt} \right) &= 3!S(kC_0)^3 \lambda_t [\sigma_i(t)], \\ &\text{when } \frac{d\sigma_i}{dt} > 0, \sigma_i > 0, \end{aligned} \quad (10)$$

where  $\sigma_i$  is the local eigenstress component,  $S$  is a shape parameter (equal to  $4\pi/3$  when the obscuration volume is similar to a sphere in 3D),  $k$  is a constant parameter ( $k = 0.38$  when the crack length becomes significantly larger than the initial size), and  $C_0$  is the 1D wave speed.

More recently, Erzar and Forquin [17] have investigated the postpeak tensile behavior of concrete by means of Monte Carlo calculations and tensile experiments performed on damaged but unbroken spalled samples. An improvement of the modeling was proposed based on the following statement: despite the propagation of the unstable cracks in the specimen, there is still a cohesive stress in the vicinity of these triggered cracks that controls the whole softening behavior of the material. Therefore a cohesive model is combined with the DFH model to describe the cohesive stress in the obscured zone and the softening behavior of geomaterials in dynamic tension [19, 20]. In the cohesive model, an extra term is added to the macroscopic stress  $\Sigma_i$  as

$$\Sigma_i = (1 - P_{oi}) \sigma_i + (P_{oi})^{\alpha_D} \sigma_{coh}(\epsilon) = (1 - D_i) \sigma_i, \quad (11)$$

where  $\sigma_{coh}$  is the residual strength in the obscuration zone yielding

$$\sigma_{coh} = \sigma_o^d \exp\left(-\left(\frac{\epsilon}{\epsilon_0^d}\right)^{n_d}\right). \quad (12)$$

TABLE 1: Material parameters used in the DFH material model.

Mechanical parameters	
$\nu$	0.15
DFH model parameters	
Weibull parameters	
$m$	23
$\sigma_w$ (MPa)	18.7
$\sigma_{sd}$ (MPa)	1.0
$Z_{eff}$ (mm <sup>3</sup> )	195
Obscuration volume parameters	
$S$	3.74
$k$	0.38

In (12)  $\alpha_D$ ,  $\sigma_o^d$ ,  $\epsilon_0^d$ , and  $n_d$  are material-dependent parameters and  $D_i$  is the damage variable defined for each principal direction. The cohesive term can be seen as an extra contribution related to the fracture energy of the material. It enforces the final failure of an element to occur when the dissipated energy due to the damage process reaches the fracture energy of the material.

In the eigenstress frame, the compliance tensor is defined by

$$\begin{bmatrix} \epsilon_1 \\ \epsilon_2 \\ \epsilon_3 \end{bmatrix} = \frac{1}{E} \begin{bmatrix} \frac{1}{1-D_1} & -\nu & -\nu \\ -\nu & \frac{1}{1-D_2} & -\nu \\ -\nu & -\nu & \frac{1}{1-D_3} \end{bmatrix} \begin{bmatrix} \Sigma_1 \\ \Sigma_2 \\ \Sigma_3 \end{bmatrix}, \quad (13)$$

where  $\epsilon_1$ ,  $\epsilon_2$ , and  $\epsilon_3$  are the principal strains and  $E$  and  $\nu$  are Young's modulus and Poisson's ratio of the undamaged material, respectively.

In the numerical analysis discussed below, the Bohus granite rock characterized in [15] is considered. Explicit values of the material parameters are presented in Table 1. The cohesion model parameters are calibrated based on the results of the spalling tests and are reported later in the next section.

At high strain rates, the ultimate strength is deterministic and is obtained from the DFH model as a function of the Weibull parameters as

$$\Sigma^u = \sigma_c \left( \frac{1}{e} \frac{(m+n-1)!}{m!n!} \right)^{1/(m+n)}, \quad (14)$$

where  $n$  is the medium dimension ( $n = 3$  in 3D) and  $\sigma_c$  a characteristic stress as

$$\sigma_c = (S_0 \lambda_0^{-1/m})^{m/(m+n)} (\dot{\sigma})^{m/(m+n)} (S^{1/n} k C)^{-n/(m+n)}. \quad (15)$$

It should be mentioned that the DFH model predicts the granite tensile strength at the strain rate of 70 1/s (the same strain rate as in the spalling test discussed earlier) as 19.5 MPa which is fairly close to the experimental result, 18.9 MPa. The material parameters used for this calculation are taken from Table 1. It should also be mentioned that the effective volume in this calculation is the volume of the cylindrical specimen

that is used in the spalling tests and therefore the average failure stress and the standard deviation should be scaled based on the Weibull size effect.

The material strain rate sensitivity can be described by the DFH model using a multiscale description that is probabilistic at low strain rates and deterministic at high strain rates [7]. Equation (10) is valid for a multiple fragmentation phenomenon at a high stress rate. In order to cover both single and multiple fragmentation processes using the same finite element (FE) code, the defect density function is modified as [6, 7]

$$\hat{\lambda}_t [\sigma_i(t)] = \begin{cases} 0, & \text{if } \sigma_F(t) \leq \sigma_k, \\ \lambda_0 \left( \frac{\sigma_i(t)}{S_0} \right)^m, & \text{otherwise,} \end{cases} \quad (16)$$

where  $\sigma_k$  is the random stress generated for each finite element according to Weibull law. A more detailed description of the multiscale model can be found in [7]. To show the prediction of the model in the whole range of strain rates, three values of  $\sigma_k$  are considered and the model prediction is plotted in Figure 7.

**3.2. Modeling of the Spalling Test and Determining the Cohesive Model Parameters.** The equation of motion is discretized using the FE method and the explicit time integration scheme is employed. The numerical simulation of the spalling tests is carried through with the DFH material model implemented as a VUMAT subroutine in the ABAQUS/Explicit software [23]. The finite element mesh used in the simulation of spalling tests is shown in Figure 8 using 8-node linear elements with reduced integration.

First the original DFH model with no cohesion is employed and the results are compared with the experiments. Later on, a cohesive strength is added to the original model to more realistically deal with the softening behavior of the material at dynamic loading. A parameter study is performed to obtain the cohesive model parameters that forms a best fit to the experimental results. It can be seen that adding the cohesive model makes the results more realistic and closer to the experimental results (see Figure 9). The cohesive model parameters are summarized in Table 2. Furthermore, the axial strain from the numerical model is compared with the gauges measurement and good agreement is obtained (see Figure 10).

**3.3. Modeling of the Spalling Test with Preexisting Structural Cracks.** The numerical modeling of the spalling tests with preexisting structural cracks is performed. As the state of the initial damage in each specimen is not completely clear, a set of numerical analyses is needed to define this state for each test. This calibration stage mainly includes changing the amount of the preexisting cracks to obtain the similar stiffness reduction as the specimen that reflects itself mainly in the postpeak part in the rear face velocity profile.

Figure 11 shows the initial damage state used in the numerical simulation of the specimen with preexisting cracks (the corresponding experimental results for this specimen are discussed in Section 2.3). The initial cracks in the numerical

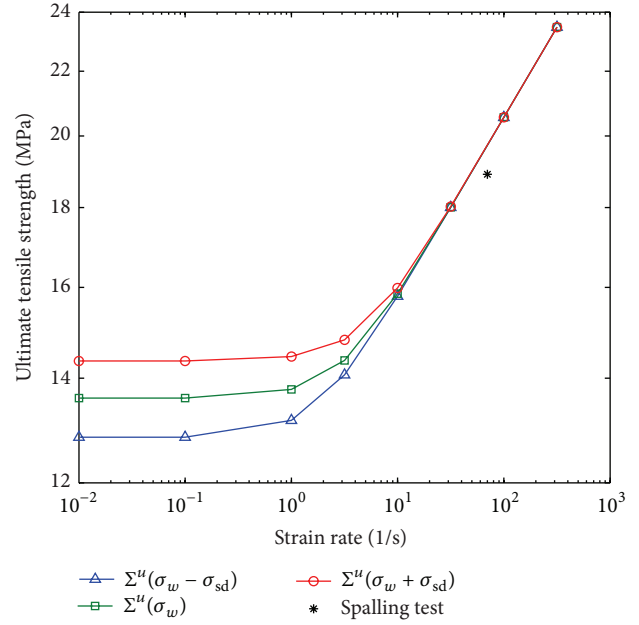


FIGURE 7: Ultimate strength in granite as a function of the strain rate in logarithmic scale based on the DFH model using the multiscale description and three values of random stress  $\sigma_k$ .

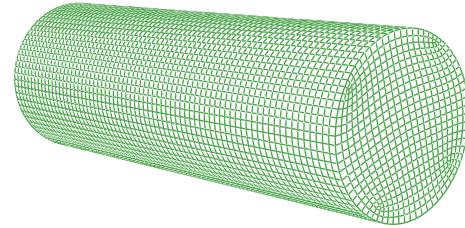


FIGURE 8: FE mesh used in the simulations of spalling tests with 38,000 8-noded elements.

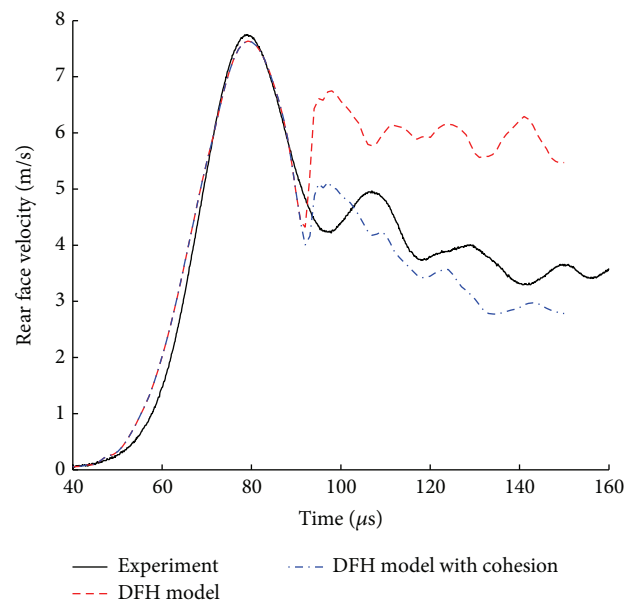


FIGURE 9: Finite element and experimental results from the spalling test for rear face velocity.

TABLE 2: Material parameters used in the cohesion model.

Cohesion model parameters	
$\alpha_D$	1.5
$\sigma_o^d$ (MPa)	12
$\varepsilon_0^d$	0.01
$n_d$	1

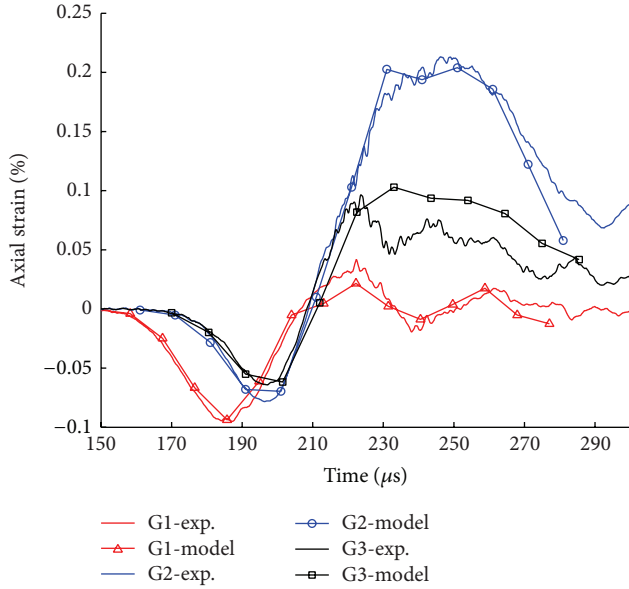


FIGURE 10: Finite element and experimental results from the spalling test for axial strain.

model consist of sets of elements with negligible tensile strength that leads to their immediate failure (the damage value becomes unity) when loaded in tension. They can still carry compressive loads when crack closure occurs due to compressive stresses. The numerical approach is described in detail in [14]. It should be mentioned that the quantity and length of these structural cracks do not necessarily correspond to the real situation in the specimen. Therefore only the total initial damage is calibrated based on the stiffness reduction occurring in the experimental results. The comparison between the experimental and numerical results is shown in Figure 12. The results with the preexisting cracks are in a better agreement with the experimental ones.

Furthermore, a numerical (FEM) quasi-static tensile test is performed on the specimen with initial damage state according to Figure 11 and an effective stiffness of about 35 GPa is obtained. This is fairly close to the average stiffness from the quasi-static tensile tests that is performed on some of the specimens with preexisting cracks as discussed earlier. This further indicates that the state of initial damage in the numerical simulation is of the correct order.

#### 4. Conclusions

The rate dependency of tensile strength in granite with and without preexisting cracks is investigated by means of spalling

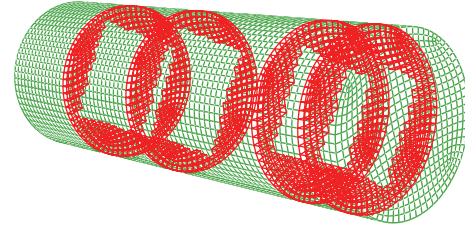


FIGURE 11: Preexisting structural cracks in the analyzed specimen. The finite element mesh is also shown.

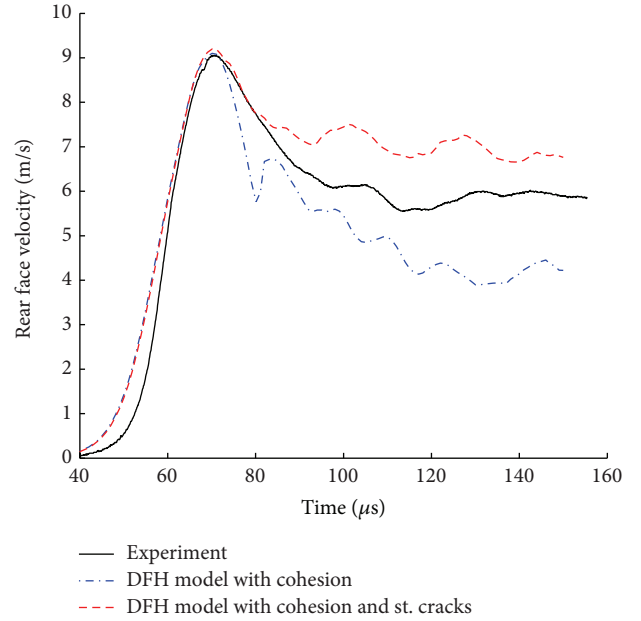


FIGURE 12: Finite element and experimental spalling test results. Preexisting structural cracks are present in the simulations.

experiments. Considerable strain rate dependency of the tensile strength is obtained at strain rates of about  $10^2$  1/s, this loading rate being pertinent to the situation of rock materials at percussive drilling, which is the application of interest in this investigation. For instance, a dynamic tensile strength of 18.9 MPa is obtained at a strain rate of 70 1/s in a sample without preexisting cracks. This is more than twice the tensile strength of the specimen (with the same size) at quasi-static conditions, which is 8 MPa.

The DFH anisotropic damage model is used to explain the material response at dynamic loading. The DFH model allows predicting the dynamic tensile strength at strain rate of 70 1/s of 19.5 MPa which is fairly close to the experimental results.

Some specimens are exposed to coarser mechanical loading during the cutting process and new cracks, called structural cracks in this work, are introduced in addition to the default material cracks and defects. It is shown that the mechanical response of the material changes dramatically during spalling test due to such preexisting cracks. The lower effective stiffness of these specimens, in tension, reflects itself in the asymmetric postpeak part in the rear face velocity profile. Also the rebounding phenomenon is not seen or is

negligible in these specimens and the rear face velocity curve is more plateau-like in the postpeak section.

Numerical modeling (finite element modeling) of the spalling tests is performed. First the original DFH model with no cohesion is employed and the results are compared with the experiments. Later on, a cohesive strength is added to the original model to more realistically deal with the softening behavior of the material at dynamic loading. It is shown that adding the cohesive strength makes the results more realistic and closer to the experimental results.

Furthermore, two-scale numerical modeling (FEM) of the spalling tests accounting for preexisting structural cracks is performed. As the state of the initial damage in each specimen is not completely clear, a first set of numerical analyses is conducted to define this state for each test. The initial cracks are introduced in the numerical model by selecting sets of elements and allocating them negligible tensile strength that leads to their immediate failure when loaded in tension. They can still carry compressive loads when crack closure occurs due to compressive stresses. It is shown that adding such cracks leads to results more similar to the experimental ones.

## Competing Interests

The authors declare that there are no competing interests regarding the publication of this paper.

## References

- [1] J. Weerheijm, *Concrete under impact tensile loading and lateral compression [Ph.D. thesis]*, Delft University, 1992.
- [2] J. R. Klepaczko and A. Brara, "An experimental method for dynamic tensile testing of concrete by spalling," *International Journal of Impact Engineering*, vol. 25, no. 4, pp. 387–409, 2001.
- [3] H. Schuler, C. Mayrhofer, and K. Thoma, "Spall experiments for the measurement of the tensile strength and fracture energy of concrete at high strain rates," *International Journal of Impact Engineering*, vol. 32, no. 10, pp. 1635–1650, 2006.
- [4] B. Erzar and P. Forquin, "An experimental method to determine the tensile strength of concrete at high rates of strain," *Experimental Mechanics*, vol. 50, no. 7, pp. 941–955, 2010.
- [5] J. Weerheijm and J. C. A. M. Van Doormaal, "Tensile failure of concrete at high loading rates: new test data on strength and fracture energy from instrumented spalling tests," *International Journal of Impact Engineering*, vol. 34, no. 3, pp. 609–626, 2007.
- [6] C. Denoual and F. Hild, "A damage model for the dynamic fragmentation of brittle solids," *Computer Methods in Applied Mechanics and Engineering*, vol. 183, no. 3-4, pp. 247–258, 2000.
- [7] P. Forquin and F. Hild, "A probabilistic damage model of the dynamic fragmentation process in brittle materials," *Advances in Applied Mechanics*, vol. 44, pp. 1–72, 2010.
- [8] A. J. Zielinski, *Fracture of Concrete and Mortar Under Uniaxial Impact Tensile Loading*, 1982.
- [9] O. K. Mahabadi, B. E. Cottrell, and G. Grasselli, "An example of realistic modelling of rock dynamics problems: FEM/DEM simulation of dynamic Brazilian test on barre granite," *Rock Mechanics and Rock Engineering*, vol. 43, no. 6, pp. 707–716, 2010.
- [10] T. Saksala, M. Hokka, V.-T. Kuokkala, and J. Mäkinen, "Numerical modeling and experimentation of dynamic Brazilian disc test on Kuru granite," *International Journal of Rock Mechanics and Mining Sciences*, vol. 59, pp. 128–138, 2013.
- [11] R. D. Krieg, "A simple constitutive description for soils and crushable foams," Report SC-DR-7260883, Sandia National Laboratories, Albuquerque, NM, USA, 1978.
- [12] D. V. Swenson and L. M. Taylor, "A finite element model for the analysis of tailored pulse stimulation of boreholes," *International Journal for Numerical and Analytical Methods in Geomechanics*, vol. 7, no. 4, pp. 469–484, 1983.
- [13] M. Saadati, P. Forquin, K. Weddfelt, P. L. Larsson, and F. Hild, "Granite rock fragmentation at percussive drilling—experimental and numerical investigation," *International Journal for Numerical and Analytical Methods in Geomechanics*, vol. 38, no. 8, pp. 828–843, 2014.
- [14] M. Saadati, P. Forquin, K. Weddfelt, P.-L. Larsson, and F. Hild, "A numerical study of the influence from pre-existing cracks on granite rock fragmentation at percussive drilling," *International Journal for Numerical and Analytical Methods in Geomechanics*, vol. 39, no. 5, pp. 558–570, 2015.
- [15] M. Saadati, *On the mechanical behavior of granite: constitutive modeling and application to percussive drilling [Doctoral thesis]*, Department of Solid Mechanics, KTH, Stockholm, Sweden.
- [16] L. Sallier and P. Forquin, "Influence of the confined behaviour and the tensile strength of concrete slabs under projectile-impact," in *Dynamic Behavior of Materials*, vol. 1, pp. 567–571, Springer, Berlin, Germany, 2013.
- [17] B. Erzar and P. Forquin, "Analysis and modelling of the cohesion strength of concrete at high strain-rates," *International Journal of Solids and Structures*, vol. 51, no. 14, pp. 2559–2574, 2014.
- [18] S. A. Novikov, I. I. Divnov, and A. G. Ivanov, "Investigation of the fracture of steel, aluminum and copper under explosive loading," *Fizika Metallov i Metallovedenie*, vol. 21, pp. 608–615, 1966.
- [19] W. Weibull, "A statistical theory of the strength of materials," Report 151, Royal Institute of Technology, Stockholm, Sweden, 1939.
- [20] W. Weibull, "A statistical distribution function of wide applicability," *Journal of Applied Mechanics*, vol. 18, no. 3, pp. 293–297, 1951.
- [21] D. G. S. Davies, "The Statistical Approach to Engineering Design in Ceramics," *Proceedings of the British Ceramic Society*, vol. 22, no. 6, pp. 429–452, 1973.
- [22] F. Hild, R. Billardon, and D. Marquis, "Hétérogénéité des contraintes et rupture des matériaux fragiles," *Comptes Rendus de l'Académie des Sciences. Série 2, Mécanique, Physique, Chimie, Sciences de l'Univers, Sciences de la Terre*, vol. 315, no. 11, pp. 1293–1298, 1992.
- [23] *Abaqus 6.11*, Dassault Systèmes Simulia, Providence, RI, USA, 2011.

## Research Article

# Modelling Thermal Shock in Functionally Graded Plates with Finite Element Method

**Vyacheslav N. Burlayenko**

*Department of Applied Mathematics, National Technical University "KhPI", 21 Frunze Street, Kharkiv 61002, Ukraine*

Correspondence should be addressed to Vyacheslav N. Burlayenko; [burlayenko@yahoo.com](mailto:burlayenko@yahoo.com)

Received 15 April 2016; Revised 24 May 2016; Accepted 2 June 2016

Academic Editor: Sergei V. Panin

Copyright © 2016 Vyacheslav N. Burlayenko. This is an open access article distributed under the Creative Commons Attribution License, which permits unrestricted use, distribution, and reproduction in any medium, provided the original work is properly cited.

Thermomechanical behavior and crack propagation in a functionally graded metal/ceramic plate undergoing thermal shock are analyzed by using the finite element method. A two-dimensional plane strain functionally graded finite element has been developed within the ABAQUS software environment for this purpose. An actual material gradation has been accomplished by sampling material quantities directly at the Gauss points of the element via programming appropriate user-defined subroutines. The virtual crack closure technique is used to model a crack growth under thermal loading. Contact possible between crack lips during the crack advance is taken into account in thermomechanical simulations as well. The paper shows that the presented finite element model can be applied to provide an insight into the thermomechanical response and failure of the metal/ceramic plate.

## 1. Introduction

The discovery of functionally gradient materials (FGMs) in the 1980s designed originally for an improvement of temperature resistance of constructive elements in nuclear reactors and chemical plants has stimulated a broad research activity for studying their behavior. An overview on mechanics of FGMs and their exploitation in modern engineering applications can be found in [1]. In general, FGMs are a new type of composite materials, which combine two or more constituent material phases. Unlike layered composite materials, FGMs are microscopically inhomogeneous with smoothly varying mechanical properties along one or more defined directions. Their structure is achieved by a gradual changing of the volume fraction of constituent materials [2].

The concept of FGMs allows one to establish the superior material properties compared with the constituent materials themselves. For instance, a typical metal/ceramic FGM possesses the mechanical strength of metal, but thermal resistance properties resemble ceramics [3]. These materials have been commonly used as thermal barrier coatings in engineering applications, undergoing a high temperature in-service environment. Moreover, they quite often experience

an exposure to a very high temperature change in a very short period of time that is known as a thermal shock. Such severe loading conditions result in high thermally induced stresses, which may very likely initiate a crack appearance in coatings. Therefore the primary interest of an analyst is to predict accurately a temperature field and is related to its temperature stresses at a design stage, since the latter have a critical relevance to trigger fracture mechanisms in FGM structures [4]. Hence, the goal of this research is to develop an efficient and reliable tool for studying thermal and mechanical response of a functionally graded metal/ceramic plate subjected to thermal shock.

A closed-form solution of the problem under consideration is very complicated and, in essence, it is possible in few one-dimensional cases with the simplest geometry, boundary conditions, and exponential gradation profiles for volume fractions, for example, [5–7]. While numerical techniques permit a look at more complex tasks under various boundary and loading conditions, material variations, including bidirectional FGMs, allow us to perform the crack growth analysis in FGM structures [8]. In this respect, the finite element method (FEM) is the most powerful tool [9]. So, we are going to use the FEM within the commercial engineering package ABAQUS [10] for carrying out thermomechanical

and crack propagation analyses in a FGM plate under thermal shock.

The main issue encountered when applying the FEM to analyze graded materials is concerned with modelling their spatially dependent properties. The simplest way to do it involves the use of conventional homogeneous elements in successive layers of the mesh, where each layer contains its own material characteristics. This approach leads to a stepwise change in material properties in the direction of the material gradient. Those models have been already employed by a number of researchers and have enabled acquiring reasonable results, for example, [11–13]. However, this approach requires a fine mesh to achieve the accuracy; in turn it leads to an excessive computational cost. To overcome this disadvantage of homogeneous finite elements, gradient finite elements allowing the implementation of a gradient of material properties into a model at the element level so that the accuracy can be retained at a coarse mesh have been proposed in the literature. In [14], the authors have developed a two-dimensional (2D) graded finite element with material properties evaluated directly at the Gauss points of the element. An alternative graded element using a fully isoparametric element formulation with the shape functions the same as for displacement interpolations has been elaborated in [15].

In the present work, we use a two-dimensional plane strain graded finite element to model thermomechanical behavior and crack analysis of a metal/ceramic FGM plate. The element has been developed by programming appropriate user-defined subroutines within the ABAQUS software environment. An actual material gradation has been accomplished by sampling material quantities directly at the Gauss points of the element [15]. Moreover, for the sake of completeness of the study the finite element formulation underlying the coupled thermomechanical problem in 2D FGM structures is stated first. The virtual crack closure technique, used for modelling a crack growth under thermal loading, is incorporated into the finite element statement. A possible contact between crack lips during the crack advance is taken into account as well. Finally, the presented finite element framework is applied to provide an insight into the thermomechanical response and failure of a metal/ceramic FGM plate.

## 2. Governing Equations

Naturally the study of a structure behavior under temperature loading has to be conducted using a theory of thermomechanical problems. Here we assume that a plate is a 2D body made of an isotropic graded metal/ceramic material with the volume fraction varying along one selected direction as shown in Figure 1. Note that we neglect the crack existence inside the plate at the beginning of consideration.

Let the plate undergo small displacements and deformations, and it is under a plane strain state. Also we assume that the material behavior of the plate satisfies a linear elastic law. Thus, using a Lagrangian description, a thermoelasticity problem of an inhomogeneous 2D body  $\mathcal{A} \in \mathbb{R}^2$  with boundary  $\mathcal{T} \in \mathbb{R}^1$  at every point  $\mathbf{x} = \mathbf{x}(x, y)$  at a time instant

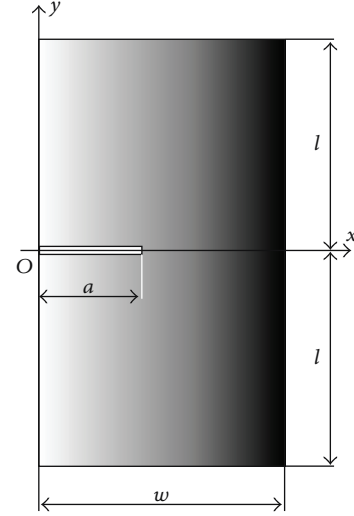


FIGURE 1: A functionally graded plate.

$t \in [0, t_*]$  can be stated as the following system of equations [16]:

$$\sigma_{ji,j} + b_i = \rho \ddot{u}_i, \quad \text{in } \mathcal{A} \times [0, t_*], \quad (1)$$

$$-q_{i,i} = c_v \dot{\theta} + T_0 \beta \dot{u}_{k,k} - \mathcal{R}, \quad \text{in } \mathcal{A} \times [0, t_*]. \quad (2)$$

Here, we use notations usual in continuum mechanics and, in what follows, the subscript “,” represents the partial differentiation, and the superscript “ $\dot{\phantom{x}}$ ” denotes the time derivative. The symbol  $\sigma_{ij}$  stands for the components of Cauchy stress tensor,  $u_i$  represents the displacements,  $\theta(\mathbf{x}, t) = T - T_0$  is a temperature change, where  $T(\mathbf{x}, t)$  is an absolute temperature, while  $T_0$  is a reference temperature at which the stress free state of the body takes place,  $b_i$  are body forces,  $q_i$  are the components of a surface heat flux, and  $\mathcal{R}$  are internal heat generation sources. The material parameters such as the mass density  $\rho(\mathbf{x})$ , the specific heat coefficient  $c_v(\mathbf{x})$ , and the stress-temperature modulus  $\beta(\mathbf{x})$  are functions of a spatial position in the Cartesian coordinate system.

In the equations of motion (1), the stress tensor satisfies the constitutive equations of thermoelasticity known as Duhamel-Neumann relations:

$$\sigma_{ij} = \lambda \varepsilon_{kk} \delta_{ij} + 2\mu \varepsilon_{ij} - \beta \delta_{ij} \theta, \quad (3)$$

where  $\lambda(\mathbf{x})$  and  $\mu(\mathbf{x})$  are the position dependent Lamé constants and the linear relations between the strains  $\varepsilon_{ij}$  and the displacements  $u_i$  are as follows:

$$\varepsilon_{ij} = \frac{1}{2} (u_{i,j} + u_{j,i}). \quad (4)$$

Solving (3) for strains, we get

$$\varepsilon_{ij} = \left\{ \hat{\lambda} \delta_{ij} \delta_{kl} + \hat{\mu} [\delta_{ik} \delta_{jl} + \delta_{il} \delta_{jk}] \right\} \sigma_{kl} + \alpha \delta_{ij} \theta, \quad (5)$$

where  $\alpha(\mathbf{x})$  is the coefficient of thermal expansion such that  $\beta(\mathbf{x}) = (3\lambda + 2\mu)\alpha$  and  $\hat{\lambda} = -\lambda/2\mu(3\lambda + 2\mu)$  and  $\hat{\mu} = 1/4\mu$ . The

last term in (5) can be referred to as the thermal deformation which is the linear function of the temperature change  $\theta$ .

In the heat transfer equation (2), the heat flux is governed by the Fourier conduction law:

$$q_i = -\kappa\theta_{,i}, \quad (6)$$

where  $\kappa(\mathbf{x})$  is the coefficient of thermal conduction depending on the coordinates  $\mathbf{x}$ .

To complete the initial-boundary value problem of thermoelasticity stated above, appropriate boundary and initial conditions have to be imposed. Given prescribed displacements  $\bar{u}_i$  and surface loading  $\bar{t}_i$ , define the mechanical boundary conditions on the boundary  $\mathcal{T}$  as follows:

$$\begin{aligned} u_i &= \bar{u}_i \quad \text{on } \mathcal{T}_u \times [0, t_*], \\ \sigma_{ij}n_j &= \bar{t}_i \quad \text{on } \mathcal{T}_\sigma \times [0, t_*], \end{aligned} \quad (7)$$

where the corresponding boundary surfaces are such that  $\mathcal{T}_u \cup \mathcal{T}_\sigma = \mathcal{T}$  and  $\mathcal{T}_u \cap \mathcal{T}_\sigma = \emptyset$ , and  $n_j$  is a unit outward normal to the surface  $\mathcal{T}$ .

The thermal boundary conditions can be specified as a prescribed temperature  $\bar{T}$  and a prescribed heat flux involving a given surface heat flux  $\bar{q}$ , volumetric heat flux  $\mathcal{R}$ , and surface convection flux on appropriate nonoverlapping parts of the boundary  $\mathcal{T}$  as follows:

$$\begin{aligned} T &= \bar{T} \quad \text{on } \mathcal{T}_T \times [0, t_*], \\ q_i n_i &= \bar{q} \quad \text{on } \mathcal{T}_{q_1} \times [0, t_*], \\ q_i n_i &= \mathcal{R} \quad \text{on } \mathcal{T}_{q_2} \times [0, t_*], \\ q_i n_i &= h(T - T_\infty) \quad \text{on } \mathcal{T}_{q_3} \times [0, t_*], \end{aligned} \quad (8)$$

where  $h(\mathbf{x})$  is the heat film transfer coefficient and  $T_\infty$  is an ambient temperature.

The initial conditions at  $t = 0$  are assumed such that displacements  $u_i$ , velocities  $\dot{u}_i$ , and a temperature change  $\theta$  are known functions:

$$\begin{aligned} u_i(\mathbf{x}, 0) &= \bar{u}_i^0 \quad \text{in } \mathcal{A} \cup \mathcal{T}, \\ \dot{u}_i(\mathbf{x}, 0) &= \dot{u}_i^0 \quad \text{in } \mathcal{A} \cup \mathcal{T}, \\ \theta(\mathbf{x}, 0) &= \theta^0 \quad \text{in } \mathcal{A} \cup \mathcal{T}. \end{aligned} \quad (9)$$

The system of (1)–(6) with boundary and initial conditions (7)–(16) are coupled because the equations of motion (1) contain a term defined by the temperature field through the thermal deformation (5), while the energy equation (2) is supplemented by a term corresponding to a rate of the dilatation of strains. Thereby, to find the solution, the system formulated above has to be solved for the displacements  $u_i$  and the temperature field  $\theta$  simultaneously.

Note that the dilatation term in the energy equation is important only for some type materials like rubber materials and it vanishes for most other materials when the external forces and heating are stationary. Besides, one can see that all material parameters involved in the constitutive laws depend on the coordinates. The latter feature considerably distinguishes the analysis of FGMs from the case of homogeneous materials.

### 3. Crack Modelling

If nonlinearities other than a crack propagation condition can be neglected, methods based on Linear Fracture Mechanics have been proven to be effective for crack modelling. In this respect, the virtual crack closure technique (VCCT) in conjunction with the FEM is one of the most commonly used approaches for determining the components of strain energy release rate (SERR) along the crack front [17]. This approach has been already successfully used for analyzing a crack propagation in layered composites, for example, in [18, 19], and has been considered as a suitable method for predicting a crack growth in FGMs, for example, [20, 21], because no assumptions of isotropy or homogeneity around the crack are necessary in the method.

The VCCT requires the introduction into a model of a predefined geometrical discontinuity. Let the crack of length  $a$  exist in the FGM plate as shown in Figure 1. In accordance with the Griffiths crack growth criterion, we assume that crack starts its advance, when the SERR  $G$  at the crack tip exceeds the critical strain energy release rate known as fracture toughness  $G_C$  at any point of the material. Using a 2D finite element model of the plate discretized with four-node elements, the work needed to extend (or that is equivalent to close) a crack along one element length can be defined with the VCCT as follows:

$$\Delta W = \frac{1}{2} (Y_1^i \Delta u_1^i + Y_2^i \Delta u_2^i). \quad (10)$$

Here as shown in Figure 2(a),  $Y_1^i$  and  $Y_2^i$  are the shear and normal forces at the  $i$ th node, and  $\Delta u_1^i$  and  $\Delta u_2^i$  refer to the shear and opening displacements at the  $j$ th node. This work done by the reactive forces and, consequently, the SERR  $G = \Delta W / \Delta A$ , where  $\Delta A = \Delta a \cdot b$  is an area of a new surface created by a crack extension  $\Delta a$ , can be calculated in one-step finite element analysis. Then the separation of individual components of the mixed-mode SERR in (10) can be found via the following equations [19]:

$$G_I = -\frac{1}{2bd} Y_2^i (u_2^{i''} - u_2^{i'}), \quad (11)$$

$$G_{II} = -\frac{1}{2bd} Y_1^i (u_1^{i''} - u_1^{i'}), \quad (12)$$

where  $b$  is the plane strain/stress thickness and  $d$  is the length of the 2D element in the mesh at the crack front. This value coincides with the crack extension  $\Delta a$ . Then, the crack will propagate due to mode I loading conditions, if the force and displacement are achieved critical values as illustrated in Figure 2(b).

In the case of mixed-mode loading, the node at the crack tip is released, if the criterion of the equivalent SERR such as  $G_{\text{eq}} \geq G_{\text{eq}}^{\text{cr}}$  was met. The total SERR  $G_T = G_I + G_{II} + G_{III}$ , where  $G_{III} = 0$  in the 2D case, is often considered for this purpose. In the forthcoming calculations, we will use the power mixity law as follows [10]:

$$\left( \frac{G_I}{G_{IC}} \right)^{k_1} + \left( \frac{G_{II}}{G_{IIC}} \right)^{k_2} + \left( \frac{G_{III}}{G_{IIIC}} \right)^{k_3} = \frac{G_{\text{eq}}}{G_{\text{eq}}^{\text{cr}}}. \quad (13)$$

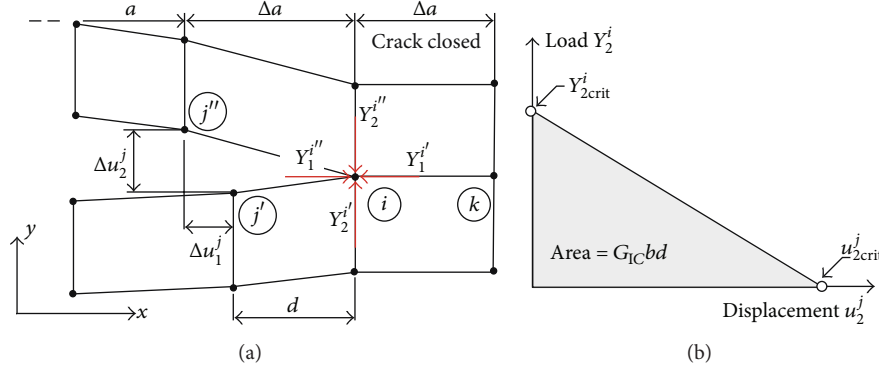


FIGURE 2: The VCCT: (a) for four-node elements and (b) with a crack growth criterion.

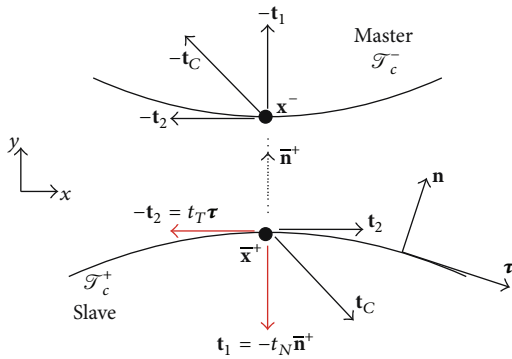


FIGURE 3: Two-dimensional contact constraints.

Thereby, the finite element model should be provided by the test data such as fracture toughness modes  $G_{IC}$ ,  $G_{IIC}$ , and  $G_{IIIC}$ , and the fitting coefficients  $k_1$ ,  $k_2$ , and  $k_3$ .

If contact between crack lips occurs, appropriate contact conditions along the interface of their interactions  $\mathcal{F}_c \in \mathcal{A}$  should be defined. Then the impenetrability and friction constraints can be imposed by establishing the Karush-Kuhn-Tucker conditions on  $\mathcal{F}_c = \mathcal{F}_c^- \cup \mathcal{F}_c^+$  in terms of displacements and tractions in the following form [22]:

$$\begin{aligned}
 t_N &\leq 0, \\
 g_N &\geq 0, \\
 t_N g_N &= 0 \\
 &\text{on } \mathcal{F}_c \times [0, t_*], \\
 |t_T| &\leq \tau_{cr}, \\
 |g_T| &\geq 0, \\
 (|t_T| - \tau_{cr}) |g_T| &= 0 \\
 &\text{on } \mathcal{F}_c \times [0, t_*].
 \end{aligned} \tag{14}$$

In the equations above we denote as in [22, 23] that  $g_N = \min_{\bar{\mathbf{x}} \in \mathcal{F}_c^-} \llbracket u_2 \rrbracket_{\mathbf{n}}$  is a gap function defining minimal distance between a point of the slave surface  $\mathbf{x} \in \mathcal{F}_c^-$  and its orthogonal projection on the master surface  $\bar{\mathbf{x}} \in \mathcal{F}_c^+$  with a unit normal

$\bar{\mathbf{n}}^+$ . Similarly,  $g_T = \llbracket u_1 \rrbracket_{\boldsymbol{\tau}}$  is a slip function describing a relative movement of those points on the contacting lines in the tangential direction  $\boldsymbol{\tau} = \mathbf{e}_3 \times \bar{\mathbf{n}}^+$  in Figure 3. Also  $t_N$  and  $t_T$  are normal and shear scalar parameters of the contact traction vector  $\mathbf{t}_c = t_N \bar{\mathbf{n}}^+ + t_T \boldsymbol{\tau}$ , whereas  $\tau_{cr}$  is a threshold of the tangential contact traction up to which the lines are retained together; otherwise the slip between the lines is governed by Coulomb's law of friction as  $\tau_{cr} = \gamma t_N$  with a given coefficient of friction  $\gamma$ .

#### 4. Weak Form of the IBVP

To obtain a numerical solution of the initial-boundary value problem (IBVP) formulated in the previous sections, its weak or variational form should be stated. The weak form of the IBVP can be obtained by applying Hamilton's principle to the body under consideration. Then, the coupled thermoelastic problem of the cracked FGM body in the current configuration corresponds to the following variational equalities:

$$\begin{aligned}
 \int_{\mathcal{A}} \frac{\partial(\delta u_i)}{\partial x_j} \sigma_{ij} d\mathcal{A} - \int_{\mathcal{F}_\sigma} \delta u_i \bar{t}_i d\mathcal{F} - \int_{\mathcal{A}} \delta u_i b_i d\mathcal{A} \\
 + \int_{\mathcal{A}} \delta u_i \rho(\mathbf{x}) \ddot{u}_i d\mathcal{A} \\
 + \int_{\mathcal{F}_c} (\delta g_N t_N + \delta g_T t_T) d\mathcal{F} = 0, \quad \forall \delta u_i \in \mathcal{U}, \\
 \int_{\mathcal{A}} \delta \theta \rho(\mathbf{x}) c_v(\mathbf{x}) \frac{\partial \theta}{\partial t} d\mathcal{A} - \int_{\mathcal{F}_q} \delta \theta \bar{q} d\mathcal{F} \\
 - \int_{\mathcal{A}} \frac{\partial(\delta \theta)}{\partial x_i} q_i d\mathcal{A} + \int_{\mathcal{A}} \delta \theta T_0 \beta(\mathbf{x}) \frac{\partial u_{k,k}}{\partial t} d\mathcal{A} \\
 + \int_{\mathcal{A}} \delta \theta \mathcal{R} d\mathcal{A} = 0, \quad \forall \delta \theta \in \mathcal{V},
 \end{aligned} \tag{15}$$

$$\begin{aligned}
 - \int_{\mathcal{A}} \frac{\partial(\delta \theta)}{\partial x_i} q_i d\mathcal{A} + \int_{\mathcal{A}} \delta \theta T_0 \beta(\mathbf{x}) \frac{\partial u_{k,k}}{\partial t} d\mathcal{A} \\
 + \int_{\mathcal{A}} \delta \theta \mathcal{R} d\mathcal{A} = 0, \quad \forall \delta \theta \in \mathcal{V},
 \end{aligned} \tag{16}$$

where the test functions  $\delta u_i$  and  $\delta \theta$  reside in appropriate vector spaces of kinematically admissible displacements  $\mathcal{U}$  and the admissible temperature field  $\mathcal{V}$  such that

$$\delta u_i \in \mathcal{U},$$

$$\mathcal{U} = \left\{ \delta u_i \mid \delta u_i \in \mathcal{C}^0(\mathcal{A}), \delta u_i = 0 \text{ on } \mathcal{T}_u \right\}, \quad (17)$$

$$\delta \theta \in \mathcal{V},$$

$$\mathcal{V} = \left\{ \delta \theta \mid \delta \theta \in \mathcal{C}^0(\mathcal{A}), \delta \theta = 0 \text{ on } \mathcal{T}_T \right\}.$$

Note that in (15) the last term comes from the contribution of the contact traction caused by the discontinuity in the displacement fields given on the boundary  $\mathcal{T}_c$ . If the contact conditions (14) are satisfied exactly, the contact term in (15) adds nothing to the total energy. However, it is possible only by a true solution, but it is not necessary by the arbitrary test functions. Because the impenetrability dictates fulfilling the inequality  $\delta g_N t_N \geq 0$ , whence, the variational equality (15) can be reorganized into a variational inequality as in [22]:

$$\begin{aligned} & \int_{\mathcal{A}} \frac{\partial(\delta u_i)}{\partial x_j} \sigma_{ij} d\mathcal{A} + \int_{\mathcal{A}} \delta u_i \rho(\mathbf{x}) \ddot{u}_i d\mathcal{A} \\ & \geq \int_{\mathcal{T}_\sigma} \delta u_i \bar{t}_i d\mathcal{T} + \int_{\mathcal{A}} \delta u_i b_i d\mathcal{A}, \quad \forall \delta u_i \in \mathcal{U}, \end{aligned} \quad (18)$$

subject to constraints (14). The final form of the functional (15) depends on the method which is used to impose the contact constraints. For this purpose, several different techniques are available in the literature such as Lagrange multipliers and penalty method [22]. Also the contact integral provides additional conditions to which the stress-strain state of the body has to obey. In doing so, at each moment of time, the stress state (or reaction forces), recovered from the calculated displacement solutions, is checked on the fulfilling the fracture criterion (13). Here we assume that the existing crack does not cause a discontinuity in the temperature field. Thus, functional (16) is not affected by the contact conditions anyhow.

## 5. Finite Element Formulation

The variational problem (15)-(16) can be solved using the FEM. So, the plate domain  $\mathcal{A}$  is discretized by a number of nonoverlapping elements  $\mathcal{A}^{(e)}$  such that the union of the elements comprises the total domain; that is,  $\mathcal{A} = \bigcup_{e=1}^{N_e} \mathcal{A}^{(e)}$ . For each finite element, unknown displacements and temperature field can be approximated by functions residing in the finite dimensional counterparts of the infinite vector spaces  $\mathcal{U}$  and  $\mathcal{V}$  as follows:

$$\begin{aligned} u_i^{(e)} &= N^I(\mathbf{x}) U_i^I(t), \\ \theta^{(e)} &= \tilde{N}^P(\mathbf{x}) \Theta^P(t), \end{aligned} \quad (19)$$

where  $I, P = 1, 2, \dots, n^{(e)}$  are nodal points and  $n^{(e)}$  is a number of nodes in the basic element,  $N^I(\mathbf{x})$  and  $\tilde{N}^P(\mathbf{x})$  are shape functions associated with nodes  $I$  and  $P$ , and  $U_i^I(t)$  and  $\Theta^P(t)$  are nodal unknown displacements and nodal unknown temperature field, respectively. The summation over the repeated index  $I$  and  $P$  is used.

Using the standard Galerkin approach, the finite element equation can be formulated by substituting interpolations (19) and their variations into the system of variational equations (15) and (16). Then, the system of semidiscrete finite element equations can be expressed as follows:

$$\begin{aligned} & \begin{bmatrix} \mathbf{M}_{uu} & \mathbf{0} \\ \mathbf{0} & \mathbf{0} \end{bmatrix} \begin{Bmatrix} \ddot{\mathbf{U}} \\ \ddot{\Theta} \end{Bmatrix} + \begin{bmatrix} \mathbf{0} & \mathbf{0} \\ \mathbf{C}_{\theta u} & \mathbf{C}_{\theta\theta} \end{bmatrix} \begin{Bmatrix} \dot{\mathbf{U}} \\ \dot{\Theta} \end{Bmatrix} \\ & + \begin{bmatrix} \mathbf{K}_{uu} & \mathbf{K}_{u\theta} \\ \mathbf{0} & \mathbf{K}_{\theta\theta} \end{bmatrix} \begin{Bmatrix} \mathbf{U} \\ \Theta \end{Bmatrix} = \begin{Bmatrix} \mathbf{F}_u - \mathbf{F}_{\text{cont}} \\ \mathbf{F}_\theta \end{Bmatrix}, \end{aligned} \quad (20)$$

where  $\mathbf{M}_{uu}$ ,  $\mathbf{K}_{uu}$ ,  $\mathbf{K}_{\theta\theta}$ , and  $\mathbf{C}_{\theta\theta}$  are global mass, stiffness, conductivity, and capacity matrices,  $\mathbf{K}_{u\theta}$  and  $\mathbf{C}_{\theta u}$  are coupled matrices,  $\mathbf{U}$  and  $\Theta$  are global vectors of unknown displacements and temperature and their appropriate time derivatives, and  $\mathbf{F}_u$ ,  $\mathbf{F}_\theta$ , and  $\mathbf{F}_{\text{cont}}$  are global vectors of external mechanical, thermal, and contact forces. Herein an explicit form of the vector of nodal contact forces  $\mathbf{F}_{\text{cont}}$  is constructed depending on the method chosen to implement the contact constraints into (15). It needs also to note that in (20) both the vector of unknowns and the contact forces should be found. Moreover, contact surfaces, on which contact constraints are enforced, are not known *a priori* as well. Thus (20) is a system of high nonlinear partial differential equations.

Discretizing a time domain  $t = \bigcup_{n=0}^{N-1} [t^n, t^{n+1}]$ , where it is assumed that a solution of (20) exists, and assuming an implicit time integration scheme to step forward the solution from a time instant  $t = t^n$  to an instant  $t + \Delta t = t^{n+1}$ , we come to a nonlinear system of algebraic equations expressed as [22]

$$\mathbf{M}\dot{\mathbf{d}}^{t+\Delta t} + \mathbf{C}\dot{\mathbf{d}}^{t+\Delta t} + \mathbf{K}^{t+\Delta t} \mathbf{d}^{t+\Delta t} = \mathbf{F}^{t+\Delta t} - \mathbf{F}_{\text{cont}}^{t+\Delta t}, \quad (21)$$

where  $\mathbf{M}$ ,  $\mathbf{C}$ , and  $\mathbf{K}$  are partitioned matrices conditionally referring mass, damping, and stiffness matrices, respectively, combining respective matrices of mechanical and thermal parts;  $\mathbf{d} = \{\mathbf{U}_u, \mathbf{U}_\theta\}^T$  is a combined vector of global nodal displacements and temperatures and the dots over this vector denote its appropriate time derivatives;  $\mathbf{F}$  is a global thermal-mechanical force vector and  $\mathbf{F}_{\text{cont}}$  is a global vector of contact forces.

The Newton-Raphson method reduces (21) to a linearized form, which at each time step  $\Delta t$  has the following form:

$$\begin{bmatrix} \check{\mathbf{K}}_{uu} & \check{\mathbf{K}}_{u\theta} \\ \check{\mathbf{K}}_{\theta u} & \check{\mathbf{K}}_{\theta\theta} \end{bmatrix} \begin{Bmatrix} \Delta \mathbf{U}_u \\ \Delta \mathbf{U}_\theta \end{Bmatrix} = \begin{Bmatrix} \mathbf{R}_u \\ \mathbf{R}_\theta \end{Bmatrix}. \quad (22)$$

In (22),  $\check{\mathbf{K}}_{IJ}$  are submatrices of the coupled Jacobian matrix,  $\Delta \mathbf{U}_u$  and  $\Delta \mathbf{U}_\theta$  are corrections referring to the solution vectors  $\mathbf{U}_u$  and  $\mathbf{U}_\theta$ , accordingly, and  $\mathbf{R}_u$  and  $\mathbf{R}_\theta$  are components of the residual force vector  $\mathbf{R}$  which is defined from (21) as follows [9]:

$$\begin{aligned} \mathbf{R}(\mathbf{d}_i^{n+1}, t^{n+1}) &= \frac{1}{\gamma_1 \Delta t^2} \mathbf{M} \mathbf{d}^{n+1} + \frac{1}{\gamma_2 \Delta t} \mathbf{C} \mathbf{d}^{n+1} \\ &+ \mathbf{K}(\mathbf{d}^{n+1}, t^{n+1}) \mathbf{d}^{n+1} \\ &- \mathbf{F}(\mathbf{d}^{n+1}, \mathbf{t}_c^{n+1}, t^{n+1}), \end{aligned} \quad (23)$$

where the superscript “ $n$ ” represents a discrete time instant and the subscript “ $i$ ” denotes an iteration.

It is important to notice that the system Jacobian matrix is nonsymmetric. Therefore, the system of linear algebraic equations (22) should be solved using a nonsymmetric matrix storage and a nonsymmetric solution scheme at each iteration within each time step.

## 6. Finite Element Modelling

The finite element formulation stated in previous sections is employed to develop the model of a cracked FGM plate, shown in Figure 1 within the engineering FEM package ABAQUS/Standard. As said earlier, one of basic issues referring to the use of the FEM in simulations of structures made of inhomogeneous materials is to model a gradient of material properties. In the present paper, we provide an effective way for implementing the continuous variation of thermal and mechanical properties into the model of FGM plate by developing a graded finite element. This is achieved by programming appropriate user-defined subroutines for finite elements available in the ABAQUS library. As a base element, a quadratic eight-node plane strain temperature-displacement element (CPE8T) is chosen. The element assumes a biquadratic displacement interpolation but a bilinear temperature interpolation. Either full or reduced integration over the element area is allowed.

The material subroutine UMAT is used to incorporate gradients into the element’s Young’s modulus, Poisson’s ratio, and coefficient of thermal expansion, whereas the subroutine UMATHT is applied to assign a spatial variation to the other element’s parameters such as conductivity and specific heat. The gradient of the element mass density is defined by the subroutine USDFLD. It should be noticed that all the subroutines specify the given material properties by sampling them directly at the Gauss points of the element.

A sequential temperature-stress analysis is carried out to model steady distributions of the temperature field and the related thermal stresses. In this analysis, the temperature field is firstly calculated by solving the heat equation and, then, the known temperature is inputted into the mechanical equation to compute thermally induced stresses. Thus, the mechanical and thermal equations in (20) are solved consequently and independently of each other. This procedure is numerically inexpensive. Once the steady thermomechanical solution is known, a transient heat transfer in conjunction with fracture analysis should be undertaken for examining the crack growth. A fully coupled temperature-stress analysis is carried out in this case. This means that both the heat equation and the motion equation in (20) are solved simultaneously with the same size of the time increment. Moreover, thermally induced stresses calculated in the transient analysis are used as driving forces for advancing the existing crack. Hence, the fracture criterion (13) is checked at each time step of the analysis. If the fracture criterion was met, the algorithm of the VCCT runs and crack is growing at this time instant. Herewith, a contact algorithm tracks a contact status and if contact occurs, the impenetrability of crack lips into each other is provided by the algorithm. The frictionless contact

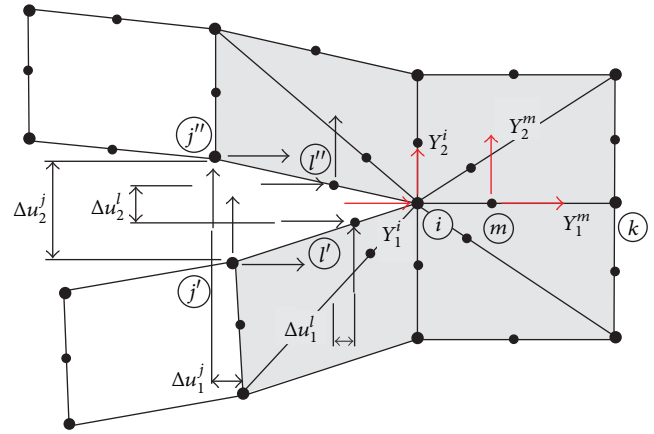


FIGURE 4: A crack tip rosette of singular quarter-point finite elements.

conditions are realized in ABAQUS by using the general contact scheme. The surface-to-surface contact behavior is governed by the “hard contact” model within the small displacement tracking algorithm [10]. The contact constraints are implemented via the penalty algorithm. Another contact model suitable for the crack propagation analysis can be found, for example, in [24, 25].

The VCCT does not require any assumptions of the form of the stresses and displacements around the crack tip [17]. Therefore, any singularity elements are not required to be embedded into the crack tip area. However, special crack tip elements have been proposed in the literature [18]. This allows one to minimize computer efforts for inducing accurately  $1/\sqrt{r}$ -singularity of the stress field at the crack tip because of mesh refinement only in a local small region. Thus, in the fracture analysis to calculate the static thermal stress intensity factor (TSIF), we employ a crack tip two-dimensional element with quarter-point nodes obtained by collapsing one side of the rectangular element [26]. A typical crack tip rosette of singular quarter-point finite elements used to induce the required singularity is illustrated in Figure 4.

The radius of ring of the singular elements around the crack tip is taken as  $0.05a$  in the calculations. The TSIFs are computed by using the  $J$ -integral analysis employing the domain integral method [10]. For the sake of comparisons we applied the VCCT with and without the singular element to calculate the TSIFs as well. In this case the node release option of the VCCT was suppressed in the calculations. Herewith the equations for the eight-node singular elements given in [27] have been used for evaluating mode I and mode II components of the SERR instead of formulae (11) and (12), as shown in Figure 4. From these results, the element size producing the required singularity in the mesh with regular elements only was found.

In fracture propagation analysis with the VCCT, we do not use the singular elements in the mesh to avoid a very time consuming procedure of remeshing for tracking a crack growth. However, to keep the required singularity properties which follow from the TSIF analysis with the singular elements, the functionally graded elements used in

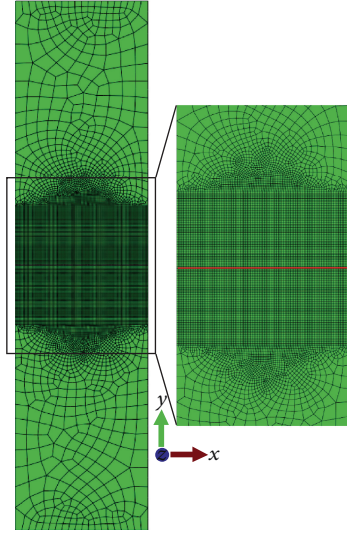


FIGURE 5: A finite element mesh used in the crack propagation analysis.

TABLE 1: Material properties of Rene-41 and ZrO<sub>2</sub> [6].

Property	Constituents	
	Rene-41	ZrO <sub>2</sub>
Young's modulus $E$ , GPa	219.7	151
Mass density $\rho$ , kg/m <sup>3</sup>	8250	5680
Poisson's ratio $\nu$	0.33	0.33
Coefficient of thermal expansion $\alpha$ , $\times 10^{-6}$ 1/K	16.7	10.0
Thermal conductivity $\kappa$ , W/mK	25.53	2.09

the analysis were refined up to a characteristic length of  $0.01a$  in a small region containing the predefined crack path. The size of remaining elements in the mesh was gradually increasing toward the top and bottom edges of the plate, keeping the symmetry, as shown in Figure 5.

Although the crack propagation is, in essence, a dynamic phenomenon itself [28] and the dynamic solution of the problem is more appropriate, we assume a quasi-static character of the crack growth in all forthcoming predictions. This was done to simplify the solution procedure of the complex elastodynamic task stated as a coupled thermomechanical problem in the previous sections. Thereby, we will neglect the inertia effect on the crack evolution in the calculations. Besides, the strain dilatation term is not taken into account in the calculations as well. It means that the coupling between thermal and mechanical parts is assumed to be through the temperature field only. Moreover, for the sake of simplicity, we suppose that there is no variation of fracture toughness along the material gradation in thermal cracking. The value of fracture toughness is spatially independent and is defined by toughness of ceramics. It can be interpreted as a lower bound of the thermal cracking resistance of the FGM plate.

## 7. Numerical Results

In this section, the results of two simulations of the FGM plate shown in Figure 1 are presented. The first analysis concerns a steady state heat transfer problem in the FGM plate of the dimensionless width  $w$  of 1 and length  $2l$  of 2 under quasi-static thermal loading. It is assumed that the plate is made of a functional graded super alloy (Rene-41)/zirconia material. The thermal and mechanical properties of the constituents of the material are given in Table 1 as those in [6]. There, the mechanical parameters are the following functions of the  $x$ -coordinate:

$$E(x) = E_c e^{\gamma x}, \quad \text{where } \gamma = \frac{1}{w} \ln \left( \frac{E_m}{E_c} \right),$$

$$\alpha(x) = \alpha_c e^{\eta x}, \quad \text{where } \eta = \frac{1}{w} \ln \left( \frac{\alpha_m}{\alpha_c} \right), \quad (24)$$

$$\kappa(x) = \kappa_c e^{\zeta x}, \quad \text{where } \zeta = \frac{1}{w} \ln \left( \frac{\kappa_m}{\kappa_c} \right),$$

where the subscripts “ $c$ ” and “ $m$ ” refer to ceramic and metal components, respectively.

It is supposed that the plate is under a stress-free state at the reference temperature  $T_0$  and is subjected to the surface temperatures  $T_1$  and  $T_2$  at  $x = 0$  and  $x = w$ , respectively. Because of the symmetry, a half plate is modelled only. The crack of length  $a/w = 0.2$  is embedded into the plate as shown in Figure 6(a). The radius of ring of the singular elements around the crack tip is taken as  $0.05a$  in the following calculations and is illustrated in Figure 6(b). Two conditions of thermal loading and groups of material parameters are considered in this analysis.

Figure 7(a) shows comparisons of the TSIFs normalized by  $\sigma_0 = E_c \alpha_c T_0 / (1 - \nu)$  between the analytical solutions in [29] and results calculated numerically with the graded elements in the cracked FGM Rene-41/zirconia plate. The material properties of the plate are taken as  $E_m/E_c = 5$ ,  $\alpha_m/\alpha_c = 2$ , and  $\kappa_m/\kappa_c = 1$ . The plate undergoes a uniform dimensionless temperature  $T_1 = T_2$ , which is less than  $T_0 = 10$  and corresponds to a variety of values  $T_1/T_0$  such as 0.5, 0.2, 0.1, and 0.005.

Analogously, the normalized TSIFs found analytically in [29] and calculated numerically with the graded elements are compared in Figure 7(b) for the cracked FGM Rene-41/zirconia plate with the material properties as  $E_m/E_c = 10$ ,  $\alpha_m/\alpha_c = 2$ , and  $\kappa_m/\kappa_c = 10$ , which is undergoing a uniform dimensionless temperature  $T_2 = 0.5T_0$ , where  $T_0 = 10$  and the ratio  $T_1/T_0$  is equal to 0.5, 0.2, 0.1, and 0.005. In Figure 7, the lines refer to the analytic solutions, whereas the markers indicate the numerical results. One can see an excellent agreement between both solutions for two cases of thermal loading and material parameters.

In the other analysis, a plate of width  $w$  of 10 mm and length  $2l$  of 40 mm made of metal/ceramic functionally graded material is modelled. It is assumed that the material of the plate consists of particles of titanium alloy Ti-6Al-4V and zirconium dioxide ZrO<sub>2</sub> ceramic. Mechanical properties

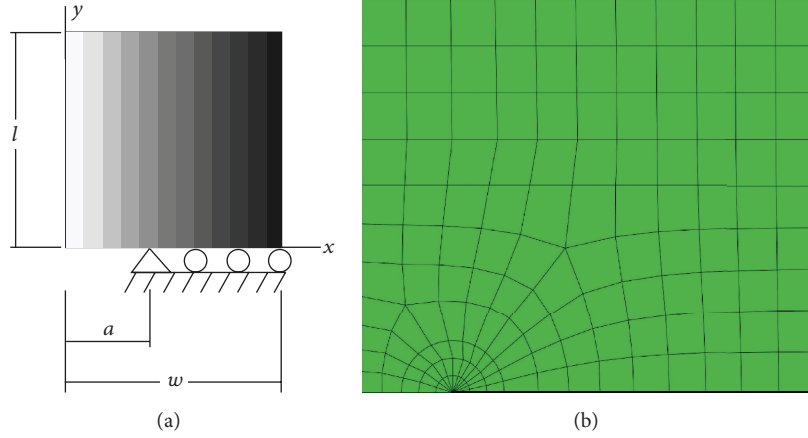
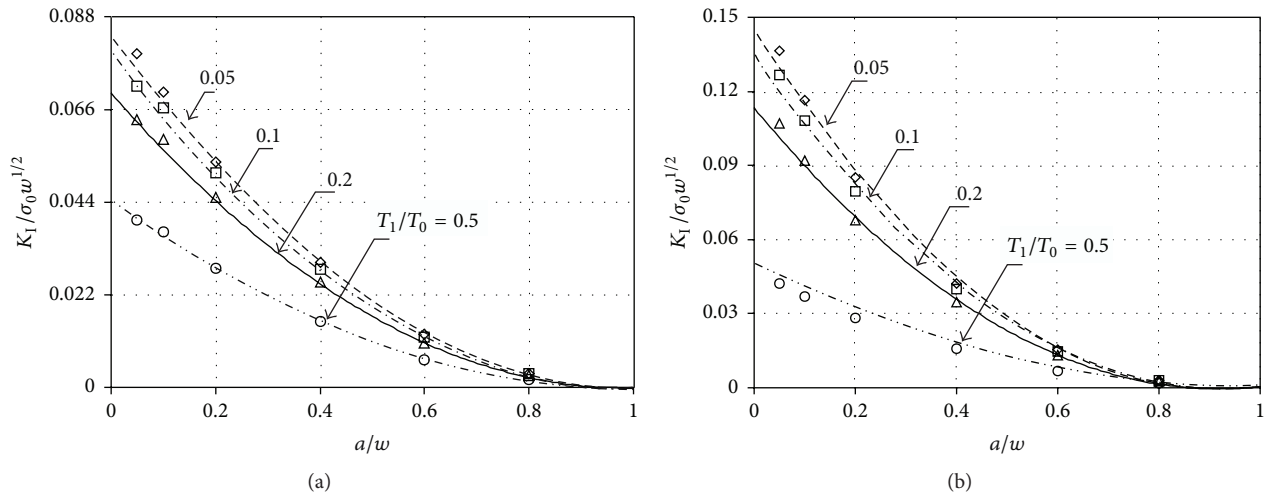


FIGURE 6: A model of the cracked plate.

FIGURE 7: Comparison of the normalized TSIF for the cracked FGM plate under thermal loading: (a)  $T_1 = T_2 = T$  and  $T < T_0$ ; and (b)  $T_2 = 0.5T_0$ .TABLE 2: Material properties of Ti-6Al-4V and ZrO<sub>2</sub> [28].

Property	Constituents	
	Ti-6Al-4V	ZrO <sub>2</sub>
Young's modulus $E$ , GPa	66.2	117
Poisson's ratio $\nu$	0.32	0.333
Mass density $\rho$ , kg/m <sup>3</sup>	4420	5600
Coefficient of thermal expansion $\alpha$ , $\times 10^{-6}$ 1/K	10.3	7.11
Thermal conductivity $\kappa$ , W/mK	18.1	2.036
Specific heat $c_v$ , J/kgK	808.3	615.6
Fracture toughness $K_{IC}$	60	6

of the constituent materials are listed in Table 2 and are those as given in [30].

Also the authors there supposed that the volume fraction of the metal phase in the direction of  $x$ -coordinate, as shown in Figure 1, varies in accordance with a power function:

$$V_m = \left(\frac{x}{w}\right)^p. \quad (25)$$

From (25), it follows that the FGM is rich in ceramic when the parameter  $p > 1$  and rich in metal when the parameter  $p < 1$ . The effective properties of the metal/ceramic Ti-6Al-4V/ZrO<sub>2</sub> plate with negligible porosity have been estimated by means of the rule of mixtures of a two-phase material as follows:

$$E = E_c \left\{ \frac{E_c + (E_m - E_c)V_m^{2/3}}{E_c + (E_m - E_c)(V_m^{2/3} - V_m)} \right\},$$

$$\nu = \nu_m V_m + \nu_c V_c,$$

$$\rho = \rho_m V_m + \rho_c V_c,$$

$$c_v = \frac{c_m V_m \rho_m + c_c V_c \rho_c}{V_m \rho_m + V_c \rho_c}, \quad (26)$$

$$\alpha = \frac{\alpha_m (V_m E_m / (1 - \nu_m)) + \alpha_c (V_c E_c / (1 - \nu_c))}{(V_m E_m / (1 - \nu_m)) + (V_c E_c / (1 - \nu_c))},$$

$$\kappa = \kappa_c \left\{ \frac{1 + 3(\kappa_m - \kappa_c)V_m}{3\kappa_c + (\kappa_m - \kappa_c)V_c} \right\}.$$

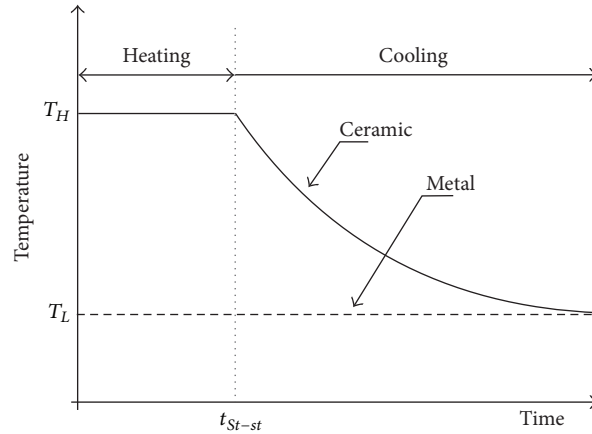


FIGURE 8: A scheme of thermal shock.

It is worth noticing that the rule of mixtures similar to (26) is only the simplest approximation of the effective properties of a nonhomogeneous material. The reasons of inaccuracy of this approach have been widely discussed earlier, for example, in [31, 32]. Instead, homogenization techniques based on microstructural analysis and empirical observations should be used for more accurate predictions in material properties of FGMs as shown in [2]. However, this discussion is out of the scope of the present paper. Only material parameters known in the literature are used in the calculations below.

As a thermal load, one cycle of thermal shock is applied to the metal/ceramic FGM plate, as shown in Figure 8. The plate is initially assumed to be stress-free at the temperature  $T_0$ ; then the plate is heated on the ceramic surface by a high temperature  $T_H$ , while the metallic surface remains at a low temperature  $T_L$  equal to  $T_0$ . After that, when the temperature field within the plate reaches a steady state, the ceramic surface undergoes a fast cooling due to an intensive forced convection. The temperature of the ceramic surface quickly decreases to  $T_L$ . As known this cooling step promotes a propagation of an existing crack that we are aiming to investigate numerically herein.

In the analysis, we assume that  $T_0 = 300$  K,  $T_H = 1300$  K, and  $T_L = 300$  K. The film convection coefficient is  $h = 2000$  W/mm<sup>2</sup> K and the temperature of a surrounding medium is  $T_\infty = 300$  K. The mesh contains a total of 2047 two-dimensional graded finite elements with 14730 numbers of degrees of freedom in the model (Figure 5). A preexistence crack of the relative length  $a/w$  of 0.2 is modelled by an actual small gap between the finite elements located along the crack lips. The fracture criterion (13) with the input parameters taken as  $G_{IC} = G_{IIC} = G_{IIIC} = 0.19$  N/mm<sup>2</sup> and  $k_1 = k_2 = k_3 = 1$  is exploited in the fracture analysis.

The loading conditions dictate the types of analyses that should be performed in this study. First a steady-state thermomechanical analysis will be used to simulate a heating phase. Second, a transient thermomechanical analysis, which is accompanied by estimations of crack onset and propagation, will be applied to describe cooling. The

contact analysis is performed in both cases once contact is detected.

The contour plots of the distributions of steady state and transient temperatures in the cracked FGM plate with  $p = 0.5$  are illustrated in Figures 9(a) and 9(b), respectively. One can see that due to heating the highest temperature is achieved on the ceramic surface of the plate. However, as a result of cooling, the temperature is redistributed with time such that its highest value is reached in the central region of the plate. Hence, an initial high level of thermally induced stresses in the ceramic surface arising during heating will be followed by their fast redistributions within the plate width under cooling.

For the sake of demonstration of a stress state induced by the corresponding temperature fields due to heating and cooling phases shown in Figure 9, the distributions of Mises stresses are displayed in Figure 10. One can see that the stress state under heating phase is more uniform than that in cooling. The fast temperature dropping gives rise to stress redistribution inside the plate; as a result a pronounced nonuniformity of the Mises stress occurs. This clearly proves a dangerous character of cooling from the standpoint of strength and the need to examine a fracture resistance of FGM plates under thermal shock conditions.

To provide a deeper insight into the thermal cracking behavior in the FGM plate, the stresses caused by the transient temperature distributions under cooling are further examined. The series of contour plots of the distributions of transient thermal stress  $\sigma_{yy}$  at different nondimensional moment of time  $\tau$  equal to a ratio of a current simulation time to a total analysis time are presented in Figure 11. From the calculations carried out with the proposed finite element model, one can conclude that crack opening due to cooling occurs because the regions of compressive stresses inside the plate appear. These compressive stresses act as a bending moment ahead of a crack tip resulting in tensile stresses in a small region near the crack lips. If these stresses are high enough to keep driving the crack, then the crack can become self-driven. Hence, as soon as the TSIF induced by the temperature field exceeds the critical stress intensity

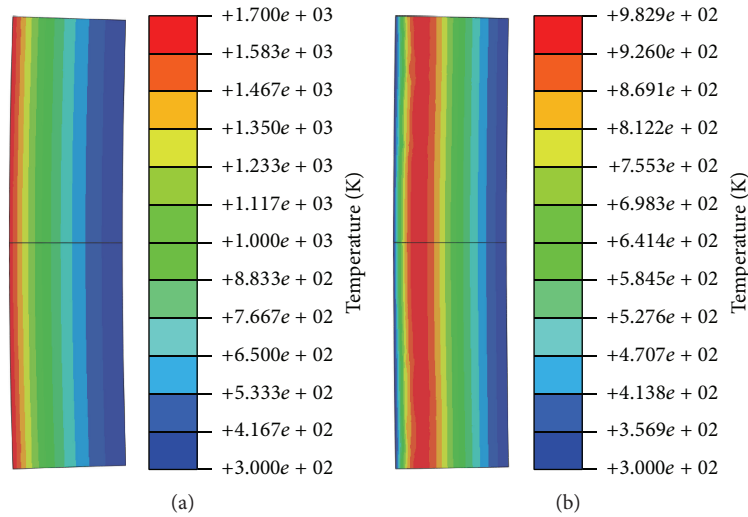


FIGURE 9: Contour plots of the temperature distributions: (a) steady state under heating and (b) transient state due to cooling at the end of analysis.

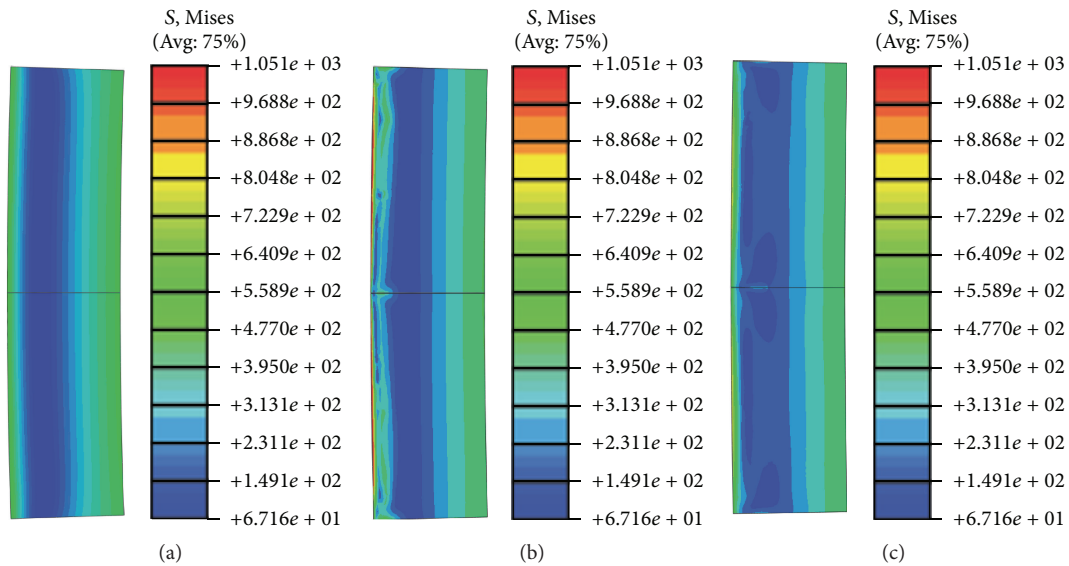


FIGURE 10: Contour plots of the distributions of Mises stress: (a) under heating and ((b) and (c)) due to cooling at a moment of a small period of time after the beginning and at the end of transient analysis.

factor of the FGM, the crack grows. The crack stops because compressive stresses appear in the domain of the plate behind the crack tip.

## 8. Conclusions

A finite element formulation of the coupled thermomechanical problem in a functionally graded plate undergoing plane strain conditions is presented. A fully coupled thermal stress analysis in conjunction with the VCCT is used to examine the thermal crack growth in the FGM plate with a preexistence crack. The finite element analysis is carried out using a graded finite element developed within the ABAQUS code via the combination of user-defined subroutines. With the graded element, a material gradation of mechanical and

thermal properties of the FGM is incorporated into the finite element model. Both the sequential thermomechanical analysis and the coupled thermomechanical analysis associated with crack extension procedure and contact conditions are carried out. The obtained results showed that the proposed finite element model based on the graded finite element is effective in thermomechanical simulations of FGM plates and enables performing accurate predictions of thermal and mechanical behavior of FGM plates under thermal shock.

## Competing Interests

The author declares that he has no competing interests.

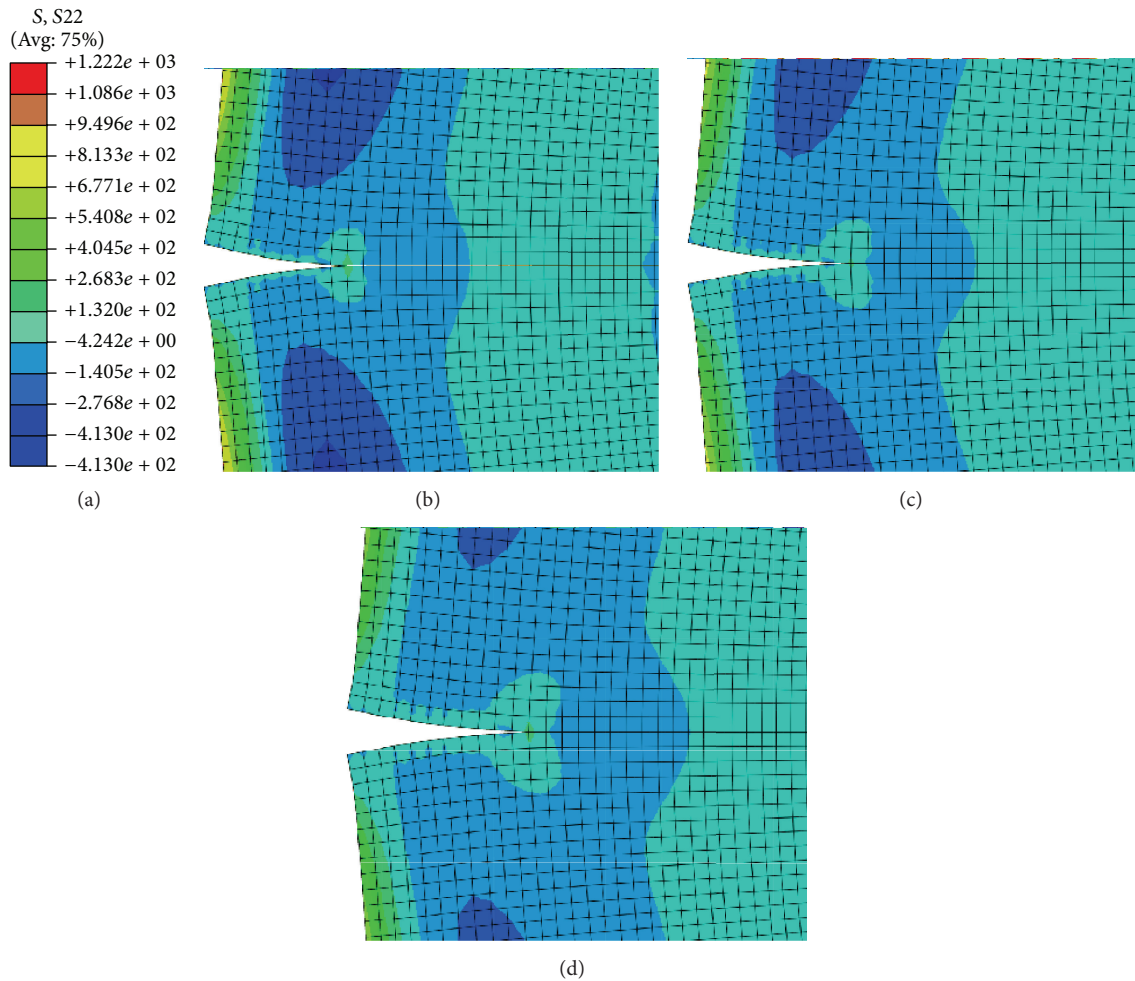


FIGURE 11: Contour plots of transient stress  $\sigma_{yy}$  at different moments of time: (a) scale level, (b)  $\tau = 0.1$  (c)  $\tau = 0.5$ , and (d)  $\tau = 1.0$ .

## Acknowledgments

The author acknowledges the Erasmus Mundus exchange program ACTIVE (Grant no. AC/TG2/SOTON/PD/23/2015) for the support of his stay in the University of Southampton. Also he would like to thank Professor Atul Bhaskar for fruitful discussions.

## References

- [1] V. Birman and L. W. Byrd, "Modeling and analysis of functionally graded materials and structures," *Applied Mechanics Reviews*, vol. 60, no. 1-6, pp. 195-216, 2007.
- [2] Y. Miyamoto, W. A. Kaysser, B. H. Rabin, A. Kawasaki, and R. G. Ford, *Functionally Graded Materials: Design, Processing and Applications*, Springer, New York, NY, USA, 1999.
- [3] M. S. El-Wazery and A. R. El-Desouky, "A review on functionally graded ceramic-metal materials," *Journal of Materials and Environmental Science*, vol. 6, no. 5, pp. 1369-1376, 2015.
- [4] T. Sadowski, "Non-symmetric thermal shock in ceramic matrix composite (CMC) materials," *Solid Mechanics and Its Applications*, vol. 154, pp. 99-148, 2009.
- [5] Y.-D. Lee and F. Erdogan, "Residual/thermal stresses in FGM and laminated thermal barrier coatings," *International Journal of Fracture*, vol. 69, no. 2, pp. 145-165, 1994.
- [6] F. Erdogan and B. H. Wu, "Crack problems in FGM layers under thermal stresses," *Journal of Thermal Stresses*, vol. 19, no. 3, pp. 237-265, 1996.
- [7] Z.-H. Jin and G. H. Paulino, "Transient thermal stress analysis of an edge crack in a functionally graded material," *International Journal of Fracture*, vol. 107, no. 1, pp. 73-98, 2001.
- [8] I. V. Ivanov, T. Sadowski, and D. Pietras, "Crack propagation in functionally graded strip under thermal shock," *The European Physical Journal: Special Topics*, vol. 222, no. 7, pp. 1587-1595, 2013.
- [9] T. Belytschko, W. K. Liu, and B. Morgan, *Nonlinear Finite Elements for Continua and Structures*, John Wiley & Sons, Chester, UK, 2000.
- [10] *ABAQUS 6.12 User's Manuals*, Dassault Systèmes Simulia Corp., Providence, RI, USA, 2012.
- [11] R. L. Williamson, B. H. Rabin, and J. T. Drake, "Finite element analysis of thermal residual stresses at graded ceramic-metal interfaces. Part I. Model description and geometrical effects," *Journal of Applied Physics*, vol. 74, no. 2, pp. 1310-1320, 1993.

- [12] G. Anlas, M. H. Santare, and J. Lambros, "Numerical calculation of stress intensity factors in functionally graded materials," *International Journal of Fracture*, vol. 104, no. 2, pp. 131–143, 2000.
- [13] J. C. Lee, J. H. Park, S. H. Ryu et al., "Reduction of functionally graded material layers for  $\text{Si}_3\text{N}_4$ - $\text{Al}_2\text{O}_3$  system using three-dimensional finite element modeling," *Materials Transactions*, vol. 49, no. 4, pp. 829–834, 2008.
- [14] M. H. Santare and J. Lambros, "Use of graded finite elements to model the behavior of nonhomogeneous materials," *Journal of Applied Mechanics*, vol. 67, no. 4, pp. 819–822, 2000.
- [15] J.-H. Kim and G. H. Paulino, "Isoparametric graded finite elements for nonhomogeneous isotropic and orthotropic materials," *Journal of Applied Mechanics, Transactions ASME*, vol. 69, no. 4, pp. 502–514, 2002.
- [16] R. B. Hetnarski and M. R. Eslami, *Thermal Stresses—Advanced Theory and Applications*, Springer Science & Business Media, 2009.
- [17] E. F. Rybicki and M. F. Kanninen, "A finite element calculation of stress intensity factors by a modified crack closure integral," *Engineering Fracture Mechanics*, vol. 9, no. 4, pp. 931–938, 1977.
- [18] R. Krueger, "Virtual crack closure technique: history, approach, and applications," *Applied Mechanics Reviews*, vol. 57, no. 2, pp. 109–143, 2004.
- [19] V. N. Burlayenko and T. Sadowski, "FE modeling of delamination growth in interlaminar fracture specimens," *Budownictwo i Architektura*, vol. 2, no. 1, pp. 95–109, 2008.
- [20] H. L. Zhou, "Implementation of crack problem of functionally graded materials with ABAQUS™," *Advanced Materials Research*, vol. 284–286, pp. 297–300, 2011.
- [21] V. N. Burlayenko, H. Altenbach, T. Sadowski, and S. D. Dimitrova, "Computational simulations of thermal shock cracking by the virtual crack closure technique in a functionally graded plate," *Computational Materials Science*, vol. 116, pp. 11–21, 2016.
- [22] T. A. Laursen, *Computational Contact and Impact Mechanics: Fundamentals of Modeling Interfacial Phenomena in Nonlinear Finite Element Analysis*, Springer, Berlin, Germany, 2002.
- [23] V. N. Burlayenko and T. Sadowski, "Finite element nonlinear dynamic analysis of sandwich plates with partially detached facesheet and core," *Finite Elements in Analysis and Design*, vol. 62, pp. 49–64, 2012.
- [24] V. N. Burlayenko and T. Sadowski, "Modeling the dynamic debonding growth of sandwich plate," in *Proceedings of the 4th International Conference on Nonlinear Dynamics*, Yu. V. Mikhlin and M. V. Perepelkin, Eds., pp. 225–230, Tochka, Sevastopol, Ukraine, June 2013.
- [25] V. N. Burlayenko and T. Sadowski, "Simulations of post-impact skin/core debond growth in sandwich plates under impulsive loading," *Journal of Applied Nonlinear Dynamics*, vol. 3, no. 4, pp. 369–379, 2014.
- [26] R. S. Barsoum, "Triangular quarter-point elements as elastic and perfectly-plastic crack tip elements," *International Journal for Numerical Methods in Engineering*, vol. 11, no. 1, pp. 85–98, 1977.
- [27] I. S. Raju, "Calculation of strain-energy release rates with higher order and singular finite elements," *Engineering Fracture Mechanics*, vol. 28, no. 3, pp. 251–274, 1987.
- [28] L. B. Freund, *Dynamic Fracture Mechanics*, Cambridge Monographs on Mechanics and Applied Mathematics, Cambridge University Press, 1990.
- [29] J.-H. Kim and G. H. Paulino, "Mixed-mode fracture of orthotropic functionally graded materials using finite elements and the modified crack closure method," *Engineering Fracture Mechanics*, vol. 69, no. 14–16, pp. 1557–1586, 2002.
- [30] T. Fujimoto and N. Noda, "Influence of the compositional profile of functionally graded material on the crack path under thermal shock," *Journal of the American Ceramic Society*, vol. 84, no. 7, pp. 1480–1486, 2001.
- [31] R. Hill, "Elastic properties of reinforced solids: some theoretical principles," *Journal of the Mechanics and Physics of Solids*, vol. 11, no. 5, pp. 357–372, 1963.
- [32] L. J. Walpole, "On bounds for the overall elastic moduli of inhomogeneous systems—I," *Journal of the Mechanics and Physics of Solids*, vol. 14, no. 3, pp. 151–162, 1966.

## Research Article

# Quasi-Brittle Fracture Modeling of Preflawned Bitumen Using a Diffuse Interface Model

Yue Hou,<sup>1</sup> Fengyan Sun,<sup>1</sup> Wenjuan Sun,<sup>2</sup> Meng Guo,<sup>1</sup> Chao Xing,<sup>3</sup> and Jiangfeng Wu<sup>1</sup>

<sup>1</sup>National Center for Materials Service Safety, University of Science and Technology Beijing, Beijing 100083, China

<sup>2</sup>The Via Department of Civil and Environmental Engineering, Virginia Polytechnic Institute and State University, Blacksburg, VA 24061, USA

<sup>3</sup>School of Transportation Science and Engineering, Harbin Institute of Technology, Harbin 150001, China

Correspondence should be addressed to Fengyan Sun; [fysun@ustb.edu.cn](mailto:fysun@ustb.edu.cn)

Received 21 March 2016; Accepted 11 April 2016

Academic Editor: Liviu Marsavina

Copyright © 2016 Yue Hou et al. This is an open access article distributed under the Creative Commons Attribution License, which permits unrestricted use, distribution, and reproduction in any medium, provided the original work is properly cited.

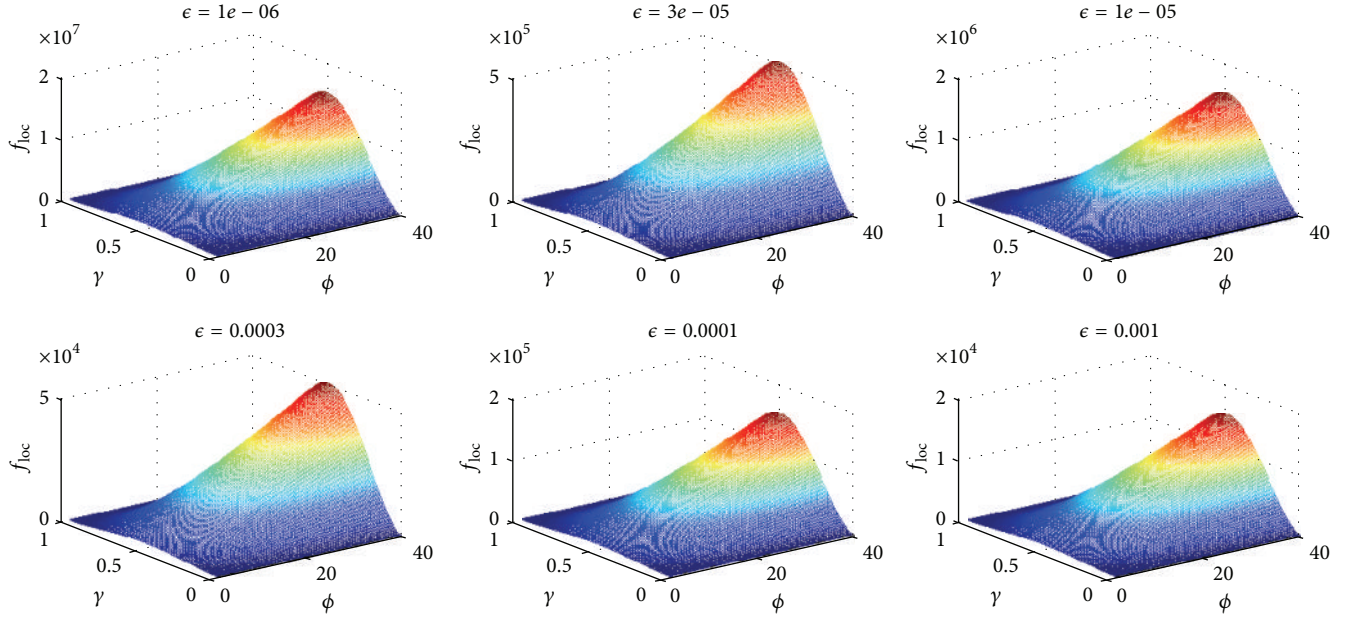
Fundamental understandings on the bitumen fracture mechanism are vital to improve the mixture design of asphalt concrete. In this paper, a diffuse interface model, namely, phase-field method is used for modeling the quasi-brittle fracture in bitumen. This method describes the microstructure using a phase-field variable which assumes one in the intact solid and negative one in the crack region. Only the elastic energy will directly contribute to cracking. To account for the growth of cracks, a nonconserved Allen-Cahn equation is adopted to evolve the phase-field variable. Numerical simulations of fracture are performed in bituminous materials with the consideration of quasi-brittle properties. It is found that the simulation results agree well with classic fracture mechanics.

## 1. Introduction

One of the most serious distresses in pavement structure is brittle cracking in bitumen [1, 2]. The Strategic Highway Research Program (SHRP) realized the importance of the cracking properties of bitumen for the first time [3]. Aya-tollahi and Pirmohammad (2013) studied the temperature effects on brittle fracture in cracked asphalt concrete [4]. Rowe et al. (2014) conducted researches on the influence of binder rheology on the cracking of asphalt mixes in airport and highway projects [5]. Dave et al. (2007) studied the thermal reflective cracking of asphalt concrete overlays [6]. Birgisson et al. (2002) predicted quasi-brittle response and crack growth in asphalt mixture with the Boundary Element Method [7]. Ameri et al. (2011) calculated the stress intensity factor in cracked asphalt pavement under traffic loading using 3D finite element analysis [8]. Tan and Guo (2014) studied the interfacial interaction between asphalt and mineral fillers and the influence on asphalt cracking [9]. Hou et al. (2014) conducted researches on the mixed mode fracture failure of asphalt binder at low temperature using the phase-field approach [10]. Feng et al. (2007) studied the anticracking

performance of the ATB30 asphalt treated base [11]. Mun and Lee (2011) modeled quasi-brittle crack growth in hot-mix asphaltic concrete mixtures using a disk-shaped compact tension test [12]. Zhao and Zhang (2010) conducted research on low temperature cracking of asphalt pavement based on Cohesive Zone Model [13]. Almost all these analyses are based on classic fracture mechanics first proposed by Griffith [14], which needs to clearly depict the crack front conditions, and thus may be very complicated. In order to consider the quasi-brittle properties of bitumen concisely, phase-field method is used in this paper. Besides, although the authors have previously analyzed the asphalt cracking using phase-field method [15], there still have been two limits: (1) the previous research is focused on the asphalt linear behavior and does not consider the quasi-brittle behavior; (2) there lacks analytical solutions on the stress during cracking.

The phase-field method (PFM) was originally proposed by Cahn and Hilliard [16]. In this model, a phase-field variable is introduced to identify different phases. In this paper, the development of an Allen-Cahn phase-field model is implemented in the finite element software COMSOL. The model was validated using the two-dimensional simulations

FIGURE 1: Local free energy density with respect to different  $\epsilon$ .

of model I quasi-brittle fracture at one fixed temperature and comparison with Griffith's theory.

## 2. Theoretical Analysis

**2.1. Free Energy in Quasi-Brittle Materials.** In the simulation of preflawed bitumen cracking, the phase-field variable is set as  $\phi = -1$  for the broken part and  $\phi = +1$  for the unbroken part. The total free energy in the cracking system is

$$F = \int_{\Omega} (f_{gr} + f_{loc} + f_{el}) dV, \quad (1)$$

where  $f_{el}$  is the elastic energy density,  $f_{gr} = 3\gamma\epsilon(\nabla\phi)^2/2$  is the gradient energy density, and  $f_{loc} = 6\gamma\phi^2(1-\phi)^2/\epsilon$  is the local free energy density (double well potential). The rationale of free energy composition in asphalt material is well explained in Hou et al. (2014) [10].  $\gamma$  is the surface free energy; and  $\epsilon$  the interface coefficient.

Figure 1 shows the double well potential function with respect to different  $\epsilon$ . It is observed that the smaller the interface coefficient  $\epsilon$  is, the larger the peak value of  $f_{loc}$  is. Also, note that curvature is significantly larger for a large surface free energy  $\gamma$ , which indicates that bitumen has more cracking resistance for a large  $\gamma$ .

Figure 2 shows the double well potential function with respect to different  $\gamma$ . It is observed that the larger the surface free energy  $\gamma$  is, the larger the peak value of  $f_{loc}$  is. Also note for a fixed  $\gamma$  value, there exist two minima at  $\phi = 0$  and  $\phi = 1$ , which indicates only these two states are metastable.

Figure 3 shows the double well potential function with respect to different  $\phi$ . Note that there are three important states:  $\phi = 0$  represents the cracking state,  $\phi = 0.5$  represents the interface state, and  $\phi = 1$  represents the unbroken state.

For these three states, the system is metastable; that is,  $f_{loc} = 0$ . Other than these states, the system is unstable.

Actually, for bitumen and bituminous materials, the materials are quasi-brittle since the visco- and plastic properties cannot be neglected no matter how small their magnitudes are. The cracking process is always initiated by the local plastic deformation at the crack tip. The plastic work needs to be done first before crack can advance to create new surfaces. The total stress is thus considered as the sum of the elastic part, the viscous part and, the plastic part as

$$\sigma_{ik}^{total} = \sigma_{ik}^{el}(\epsilon_{ik}) + \sigma_{ik}^{vis}(\dot{\epsilon}_{ik}) + \sigma_{ik}^{pl}. \quad (2)$$

For low temperature cracking on bitumen and bituminous materials, the latter two terms in (2) can be neglected for approximation.

The elastic part can be obtained according to Hooke's law as

$$\sigma_{ik}^{el} = \frac{E}{1+\nu} \left( \epsilon_{ik} + \frac{1}{1-2\nu} \delta_{ik} \epsilon_{ii} \right), \quad (3)$$

where  $\delta_{ik}$  is Kronecker delta.

The viscous part could similarly be obtained as [17]

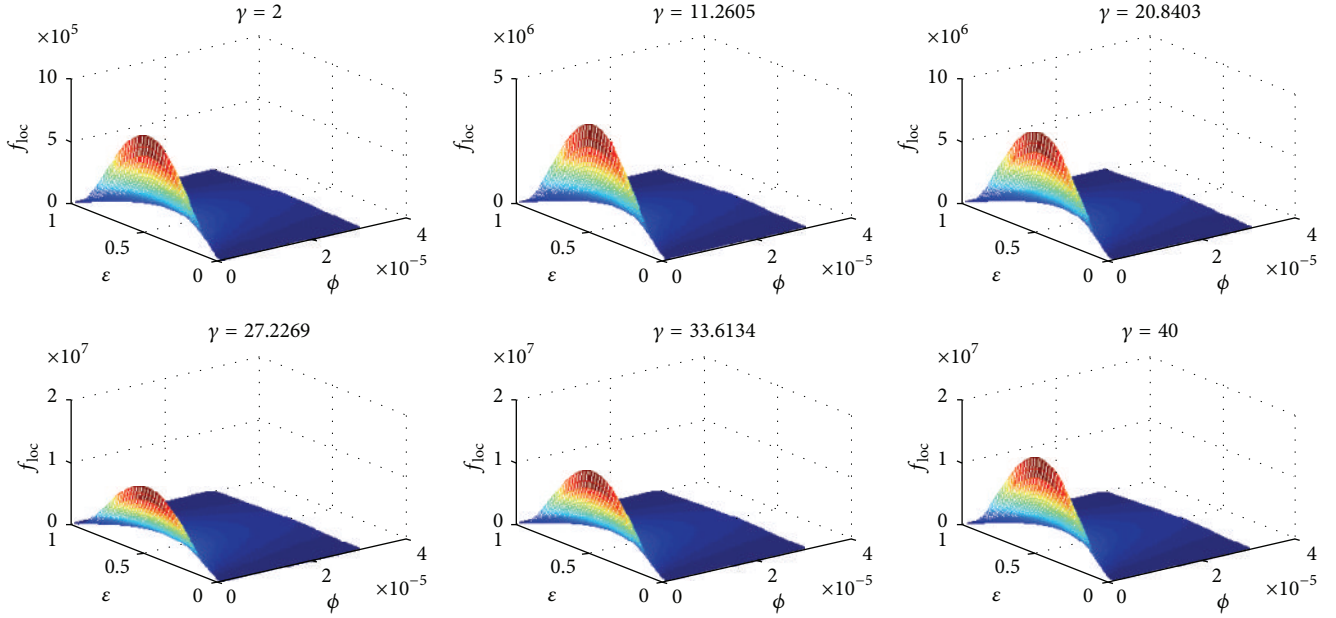
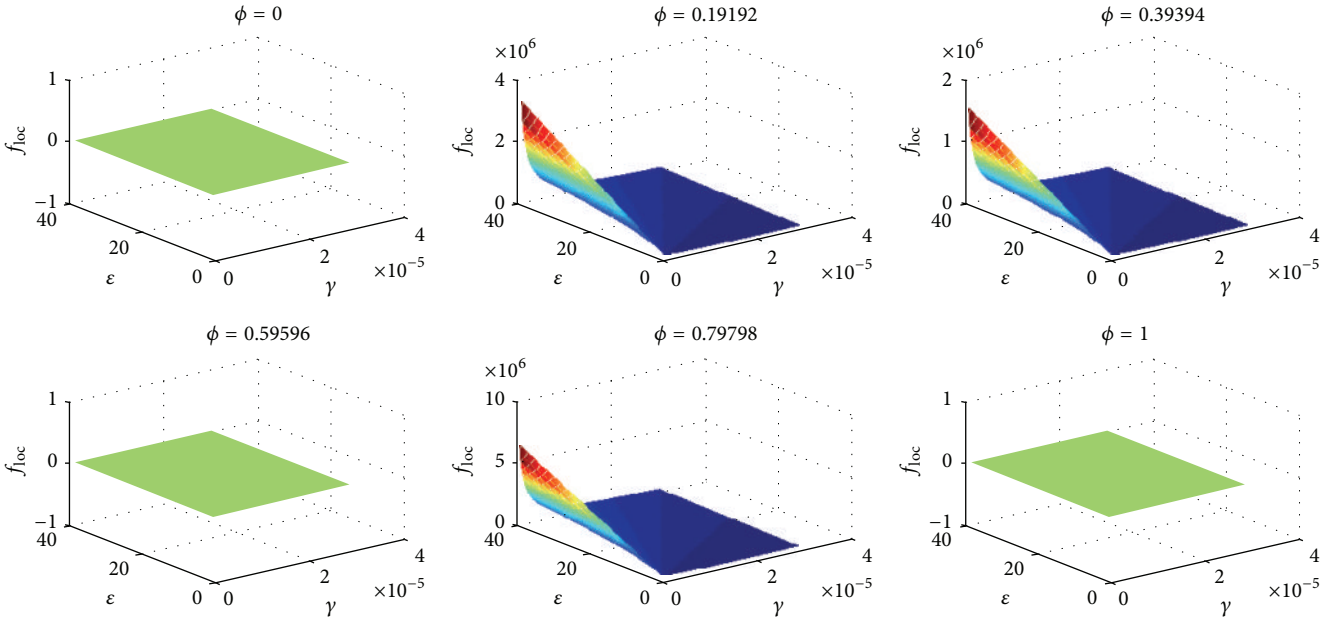
$$\sigma_{ik}^{vis} = \frac{\eta}{1+\zeta} \left( \dot{\epsilon}_{ik} + \frac{1}{1-2\zeta} \delta_{ik} \dot{\epsilon}_{ii} \right), \quad (4)$$

where  $\eta$  and  $\zeta$  are two viscosity constants defined similar to the elastic constants in (3).

The plastic stress is obtained as

$$\sigma_{ik}^{pl} = \sqrt{\frac{1}{2} \left[ (\sigma_x - \sigma_y)^2 + (\sigma_x - \sigma_z)^2 + (\sigma_y - \sigma_z)^2 \right]}, \quad (5)$$

where  $\sigma_x$ ,  $\sigma_y$ , and  $\sigma_z$  are the localized stress.


 FIGURE 2: Local free energy density with respect to different  $\gamma$ .

 FIGURE 3: Local free energy density with respect to different  $\phi$ .

2.2. *Momentum Equations.* The evolution of the stress fields is determined by the principle of momentum conservation:

$$\rho \ddot{u}_i = \frac{\partial}{\partial x_i} (\sigma_{ik}^{\text{el}} + \sigma_{ik}^{\text{vis}} + \sigma_{ik}^{\text{pl}}). \quad (6)$$

In order to implement phase-field in the stress field, the elastic modulus should be modified as

$$\sigma_{ik} = \frac{E(\phi)}{1 + \nu} \left( \varepsilon_{ik} + \frac{1}{1 - 2\nu} \delta_{ik} \varepsilon_{ii} \right), \quad (7)$$

where  $E(\phi)$  is the elastic modulus and  $\nu$  is Poisson's ratio. And  $E(\phi) = E + (E - E_0)(-(1/4)\phi^3 + (3/4)\phi + (1/2))$ , where  $E$  and  $E_0$  are the elastic moduli of the bitumen and the broken part, respectively.

Note that the viscous part and plastic part almost have no contributions to quasi-brittle cracking. Allen-Cahn equation is implemented as the governing equation:

$$\frac{\partial \phi}{\partial t} = -\frac{D}{3\gamma\epsilon} \psi, \quad (8)$$

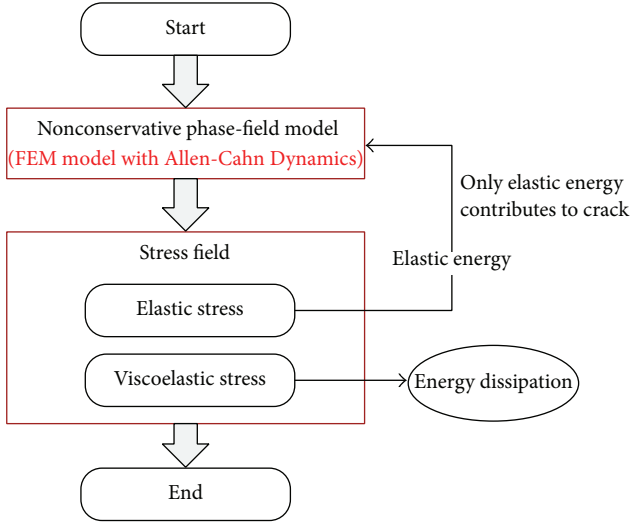


FIGURE 4: Quasi-brittle cracking calculation flowchart.



FIGURE 5: Asphalt mixture with coarse aggregates.

where  $D$  corresponds to the kinetic coefficient and  $\psi$  is the chemical potential:

$$\psi = \frac{\delta F}{\delta \phi} = -\nabla \cdot \lambda \nabla \phi + \frac{\lambda}{\epsilon^2} (\phi^2 - 1) \phi + \frac{\partial f_{el}}{\partial \phi}. \quad (9)$$

Figure 4 shows the whole computation scheme.

### 3. Results

**3.1. Applicability.** The derivations of our previous theoretical analysis based on PFM lies in that bituminous material can be considered isotropic and homogenous. However, in reality, there will exist large coarse aggregates in asphalt mixture, as shown in Figure 5. In this case, the accuracy of PFM will be reduced. Nevertheless, if the asphalt concrete could be approximately considered as isotropic and the crack goes through the bitumen part other than through the aggregate, the PFM theory can still be used for approximation.

The cracking simulation using the diffuse interface approach used in this paper could be not only good for preflawed bitumen quasi-brittle cracking but also good for bituminous mixture using fine aggregates (Figure 6(a)). This method will not have high accuracy for bituminous mixture using coarse aggregates (Figure 6(b)).

**3.2. Theoretical Stress Analysis.** The authors have previously analyzed the asphalt binder cracking using phase-field method at low temperature [15]. However, there still have been two limits: (1) the previous research is focused on the asphalt linear behavior and does not consider the quasi-brittle behavior; (2) there lacks analytical solutions on the stress during cracking. To solve the second problem, the following equations are derived.

Consider the preflaw in bitumen specimen as a rectangular crack with depth  $w$  and width  $d$ . The analytical expressions for stress are first obtained. For brittle cracking, Akono et al. (2011) suggested the specific  $J$ -integral expression for a rectangular crack propagation as [18]

$$J = \frac{1}{p} \int_A \left( W n_x - t_i \frac{\partial u_i}{\partial x} \right) dA, \quad (10)$$

where  $p = w + 2d$  is the perimeter edge of the crack.  $w$  is the crack width and  $d$  is crack depth. Figure 7 shows the cracking contour. Note that in our research  $\sigma_{xx} = 0$ , and all of the elastic strain energy is contributed by  $\sigma_{yy}$  which is different from Akono et al.'s previous work [18].

Based on Hooke's law, we further have elastic strain energy density as  $W = (\kappa/2E)\sigma_{yy}^2$ ;  $dA = (w + 2d)ds$ , and  $ds = wdz$ . Since the  $J$ -integral only has physical meaning when crack begins to propagate, we substitute the critical value  $F = F_0$  into (11) and we have  $\sigma_{yy} = F_0/(S - l_0d)$ .

Since there is no traction on the fracture surface, we thus have

$$J = \frac{1}{w + 2d} \int_0^d W w dz = \frac{\kappa w d \sigma_{yy}^2}{2E(w + 2d)}, \quad (11)$$

where  $\kappa = 1 - \nu^2$  for plane stress and  $\kappa = 1$  for plane strain.

Also, note that, during the linear elastic cracking process, the elastic strain energy will be totally transformed to the fracture energy  $G$ ; that is,

$$J = G = \frac{\kappa K_C^2}{E}. \quad (12)$$

Compare (11) and (12), we now have

$$\sigma_{yy} = \sqrt{2} K_C \sqrt{\frac{1}{d} + \frac{2}{w}}, \quad (13)$$

$$\sigma_{yy} = k\sigma = \frac{kF}{S}, \quad (14)$$

where  $k$  is the stress concentration factor due to the existence of visco- and plastic properties in bitumen.

Equation (14) indicates the relationship between the pre-made crack dimensions and stress based on the assumption of linear fracture mechanics, which needs to be further modified if the bitumen cracking is not quasi-brittle. It is observed that, for a given  $K_C$ , the smaller the initial crack is, the larger the stress is.

**3.3. Numerical Simulations.** A two-dimensional finite element model is established in COMSOL to simulate the quasi-brittle cracking process of bitumen under tension loading.



FIGURE 6: (a) Fine aggregates and (b) coarse aggregates.

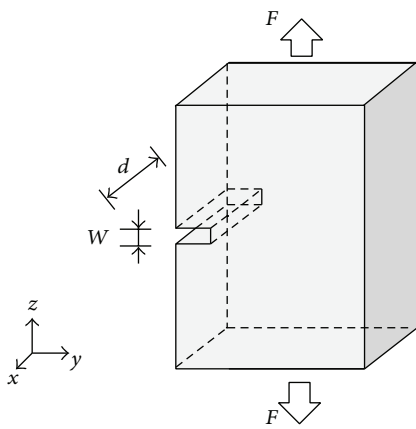


FIGURE 7: Cracking contour.

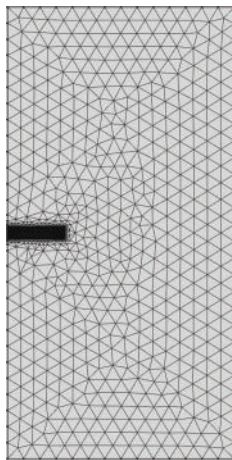


FIGURE 8: Fixed Eulerian mesh in preflawed bitumen model.

A fixed Eulerian mesh is used to describe the internal interfaces between the intact solid and crack void, as shown in Figure 8.

Actually the overall cracking process in preflawed bitumen should be simulated in three dimensions. However, it will be very costly to do such simulation. Previous researches

[10, 19] show that two-dimensional simplification, that is, plain strain or plain stress, will have sufficient accuracy for small size bitumen specimen. In our case, consider that the strain on the  $z$  direction almost remains the same during cracking, and the plain strain assumption is used for simplification and the computational domain is a rectangular with dimensions  $0.04 \times 0.02$  m. The thickness of the preflawed bitumen model is set as  $0.01$  m. The interfacial thickness is  $\epsilon = 0.001$  m and the initial crack length is  $a = 0.005$  m. The finite crack width is  $W = 0.001$  m. The six-node triangular elements (P2 element) are used in the finite element calculations. 78,061 elements are used in the initial mesh. To solve the phase-field variable  $\phi$  across the interface conveniently, the self-adaptive meshing is employed. The whole computation is conducted on a PC with Intel Core i7-4702HQ CPU, which takes about 2 hours computational time. It is expected that the smaller the interface coefficient is and the more the meshing is used, the more accurate the results will be.

Pure tension loading is applied on top and bottom boundaries, which is set as  $\sigma(t) = (\sigma_0/t_0) \cdot t$  where  $\sigma_0/t_0 = 2 \times 10^6$  N/m<sup>2</sup>s. The time step  $\Delta t$  is set as 0.1 s, considering our computational ability.

To study the quasi-brittle cracking behavior and viscoelastic cracking behavior on bitumen, two simulations are conducted simultaneously. The first is to consider the bitumen as linear elastic, while the second is to consider bitumen as viscoelastic plastic.

*Case 1.* Quasi-brittle cracking: the following material properties are used:  $\gamma = 183.77$  J/m<sup>2</sup>,  $E = 5.8$  MPa, and Poisson's ratio  $\nu = 0.3$ .

*Case 2.* Viscoelastic cracking is used to reflect the viscoelastic property of bitumen.

In order to study the differences between quasi-brittle cracking and viscoelastic cracking in our phase-field model on bitumen, the fracture results are first calculated and compared to classic fracture mechanics, where the Griffith criterion is  $K_I \geq K_{IC}$ ,  $K_I$  is the mode I stress intensity factor and  $K_{IC}$  is the mode I fracture toughness which is a material parameter.

For bitumen at low temperature,  $K_{IC} = 48 \text{ kNm}^{-3/2}$  by Ponniah et al. [20] is selected as fracture toughness. The elastic modulus of bitumen specimen is 5.8 MPa, which corresponds to a fracture energy  $G_C = 368 \text{ J/m}^2$ .

The critical load calculation based on the classic fracture mechanics without considering viscous property can be calculated as 313310.96 Pa. In phase-field method, the load value at the time instant when  $\phi$  reaches  $-1$  is considered to be the critical load.

For Case 1, where bitumen brittle-cracking occurs, our simulation results show that at time step = 16 $\Delta t$  critical load happens, which corresponds to a load as 320000 Pa.

For Case 2, where bitumen brittle-cracking occurs, our simulation results show that at time step = 31 $\Delta t$  critical load happens, which corresponds to a load as 620000 Pa.

The reason why the critical load in quasi-brittle phase-field model is much smaller than that in the viscoelastic model is that only the elastic stress part will contribute to fracture rather than the total stress (including elastic stress, viscous stress, and plastic stress) during brittle-cracking. It means bitumen has more resistance to fracture when considering viscoelastic properties than pure brittle linear elastic.

For infinitesimal deformation during bitumen brittle cracking, Cauchy stress is the same as Piola-Kirchhoff stress, which indicates the pure brittle cracking. However, considering the “quasi-brittle” property, finite deformations will occur at crack tip, and the second Piola-Kirchhoff stress is used to express the stress with Gauss-point evaluation. For the  $x$  component of second Piola-Kirchhoff stress at  $t = 1.6 \text{ s}$  at the crack tip, the calculation result is  $1.7 \times 10^6 \text{ pa}$ , which is very large compared with other regions.

#### 4. Summary

In this paper, we present a phase-field model to analyze the quasi-brittle fracture in bitumen subject to tension loading. In phase-field model, only the elastic stress will contribute to the fracture. Overall, compared with the classic fracture mechanics, the phase-field model does not need to explicitly treat the crack surface and can easily solve the quasi-brittle cracking of preflawed bitumen specimen.

#### Competing Interests

The authors declare that they have no competing interests.

#### Acknowledgments

The research performed in this paper is supported by National Natural Science Foundation of China (no. 51308042 and no. 41372320), Natural Science Foundation of Shandong Province (ZR2015EQ009), and the Fundamental Research Funds for the Central Universities (06500036).

#### References

- [1] C. Peterson, W. Buttlar, and A. Braham, “Mixed-mode cracking in asphaltic concrete,” *Advanced Testing and Characterization of Bituminous Materials*, vol. 2, pp. 785–795, 2009.
- [2] E. V. Dave and W. G. Buttlar, “Thermal reflective cracking of asphalt concrete overlays,” *International Journal of Pavement Engineering*, vol. 11, no. 6, pp. 477–488, 2010.
- [3] D. A. Anderson, D. W. Christensen, H. U. Bahia, M. G. Sharma, C. E. Antle, and J. Button, “Binder characterization and evaluation,” Strategic Highway Research Program (SHRP) A-369, National Research Council, 1994.
- [4] M.-R. Ayatollahi and S. Pirmohammad, “Temperature effects on brittle fracture in cracked asphalt concretes,” *Structural Engineering and Mechanics*, vol. 45, no. 1, pp. 19–32, 2013.
- [5] G. M. Rowe, G. King, and M. Anderson, “The influence of binder rheology on the cracking of asphalt mixes in airport and highway projects,” *Journal of Testing and Evaluation*, vol. 42, no. 5, pp. 1063–1072, 2014.
- [6] E. V. Dave, S. H. Song, W. G. Buttlar, and G. H. Paulino, “Reflective and thermal cracking modeling of asphaltic concrete overlays,” *Advanced Testing and Characterization of Bituminous Materials*, vol. 2, pp. 1241–1252, 2007.
- [7] B. Birgisson, B. Sangpetngam, and R. Roque, “Predicting viscoelastic response and crack growth in asphalt mixtures with the boundary element method,” *Transportation Research Record*, vol. 1789, pp. 129–135, 2002.
- [8] M. Ameri, A. Mansourian, M. Khavas, M. Aliha, and M. Ayatollahi, “Cracked asphalt pavement under traffic loading—a 3D finite element analysis,” *Engineering Fracture Mechanics*, vol. 78, no. 8, pp. 1817–1826, 2011.
- [9] Y. Tan and M. Guo, “Interfacial thickness and interaction between asphalt and mineral fillers,” *Materials and Structures*, vol. 47, no. 4, pp. 605–614, 2014.
- [10] Y. Hou, P. Yue, Q. Xin, T. Pauli, W. Sun, and L. Wang, “Fracture failure of asphalt binder in mixed mode (Modes I and II) by using phase-field model,” *Road Materials and Pavement Design*, vol. 15, no. 1, pp. 167–181, 2014.
- [11] X.-J. Feng, P.-W. Hao, and X.-D. Zha, “Research on low temperature anti-cracking performance of the ATB30 asphalt treated base,” *Journal of Wuhan University of Technology*, vol. 29, no. 6, pp. 35–49, 2007.
- [12] S. Mun and H.-J. Lee, “Modeling viscoelastic crack growth in hot-mix asphalt concrete mixtures using a disk-shaped compact tension test,” *Journal of Engineering Mechanics*, vol. 137, no. 6, pp. 431–438, 2011.
- [13] Y. Zhao and D. Zhang, “Study of low temperature cracking of asphalt pavement based on cohesive zone model,” *Journal of Highway and Transportation Research and Development*, vol. 27, no. 1, pp. 11–16, 2010.
- [14] A. A. Griffith, “The phenomena of rupture and flow in solids,” *Philosophical Transactions of the Royal Society of London A*, vol. 221, no. 582–593, pp. 163–198, 1921.
- [15] Y. Hou, L. Wang, P. Yue, T. Pauli, and W. Sun, “Modeling mode I cracking failure in asphalt binder by using nonconserved phase-field model,” *Journal of Materials in Civil Engineering*, vol. 26, no. 4, pp. 684–691, 2014.
- [16] J. W. Cahn and J. E. Hilliard, “Free energy of a nonuniform system. I. Interfacial free energy,” *The Journal of Chemical Physics*, vol. 28, no. 2, pp. 258–267, 1958.

- [17] M. Fleck, *Solid-state transformations and crack propagation: a phase field study [Ph.D. thesis]*, University of Bayreuth, Bayreuth, Germany, 2011.
- [18] A.-T. Akono, P. M. Reis, and F.-J. Ulm, "Scratching as a fracture process: from butter to steel," *Physical Review Letters*, vol. 106, no. 20, Article ID 204302, 2011.
- [19] D. Gross and T. Seelig, *Fracture Mechanics: With an Introduction to Micromechanics*, Springer, New York, NY, USA, 2006.
- [20] J. E. Ponniah, R. A. Cullen, and S. A. Hesp, "Fracture energy specifications for modified asphalts," *Proceedings in ACS Division of Fuel Chemistry*, vol. 41, no. 4, pp. 1317–1321, 1996.

## Research Article

# Effect of the Yield Criterion of Matrix on the Brittle Fracture of Fibres in Uniaxial Tension of Composites

Sergei Alexandrov,<sup>1</sup> Yaroslav Erisov,<sup>2</sup> and Fedor Grechnikov<sup>2</sup>

<sup>1</sup>*Institute for Problems in Mechanics, Russian Academy of Sciences, 101-1 Prospect Vernadskogo, Moscow 119526, Russia*

<sup>2</sup>*Samara State Aerospace University, 34 Moskovskoe Shosse, Samara 443086, Russia*

Correspondence should be addressed to Yaroslav Erisov; [yaroslav.erisov@mail.ru](mailto:yaroslav.erisov@mail.ru)

Received 22 March 2016; Revised 12 April 2016; Accepted 13 April 2016

Academic Editor: Filippo Berto

Copyright © 2016 Sergei Alexandrov et al. This is an open access article distributed under the Creative Commons Attribution License, which permits unrestricted use, distribution, and reproduction in any medium, provided the original work is properly cited.

This paper examines the effect of the yield criterion of the matrix on brittle fracture of the fibre in continuous fibre reinforced metal matrix composites subjected to tension in the direction parallel to the fibres. It is assumed that the matrix obeys quite a general isotropic yield criterion. An approximate approach to predicting the tensile load at which the fibre breaks previously proposed in the literature is adopted. It is shown that this tensile load is practically independent of the yield criterion of the matrix. This is a great advantage for engineering applications since an analytic solution is available in the case of Tresca yield criterion. This solution can be used for a wide range of matrix materials with no loss of the accuracy of the prediction of the tensile load at which the fibre breaks.

## 1. Introduction

There are many applications in which continuous and short fibre reinforced metal matrix composites are required. There is a class of such composites in which the fibre is made of brittle material and the matrix of ductile material [1–3]. Failure of such composites involves various mechanisms such as fibre fracture, interfacial debonding, and matrix plasticity. The effect of short fibre reinforcement on the fracture toughness of metal matrix composites has been studied in [4, 5]. Interfacial debonding has been investigated in [6–8]. Computational methodologies for modeling fracture in continuous fibre reinforced metal matrix composites and in laminated composites at the micromechanical level have been proposed in [7–10]. It has been shown in [11] that the interfacial conditions strongly affect tensile fracture characteristics of a boron-fibre-reinforced aluminum composite.

In the present paper the brittle fracture of fibres in continuous fibre reinforced metal matrix composites subjected to uniaxial tension is predicted using the approach proposed in [1]. In the latter work, this approach has led to a simple analytic solution for the axial force at which the fibre breaks. In particular, the solution predicts the influence of the volume

fraction of fibres on the strength of composites, which is well known from experiment [12]. Tresca's yield criterion has been adopted for the matrix in [1]. However, it is known that the strength of metal matrix composites is influenced by many factors including matrix strength [13]. Moreover, the in situ flow properties of the matrix of metal matrix composites differ from the properties of the matrix bulk material and the experimental scatter is much larger for experiments in the matrix than in the corresponding bulk material [14]. It is therefore of importance to extend the approach proposed in [1] to generalized yield criteria. Such criteria have been proposed, for example, in [15, 16]. In the present paper, the criterion proposed in [15] is used. It is shown that the predicted magnitude of the axial force at which the fibre breaks is almost independent of the yield criterion of the matrix. Therefore, the analytical expression derived in [1] can be used for a large class of continuous fibre reinforced metal matrix composites. The main result of the present paper can be used in conjunction with methods developed to study the behaviour of composites in the presence of fractured fibres (e.g., [17]).

The rigid plastic solution found in the present paper is of academic interest as well. To the best of authors' knowledge,

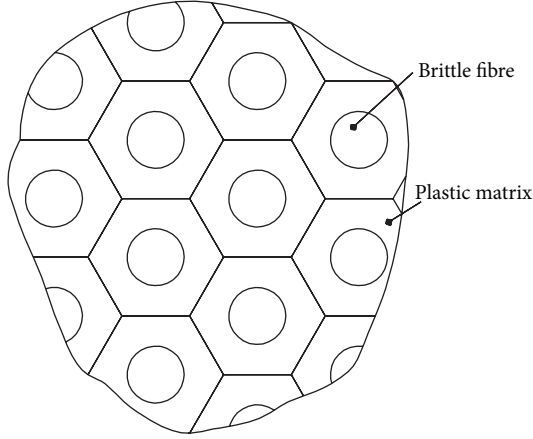


FIGURE 1: Typical cross section of the idealized composite.

the only available nontrivial axisymmetric semianalytic rigid plastic solution for the generalized yield criterion has been outlined in [18]. In this paper, flow through an infinite conical channel has been analyzed. An alternative solution to this problem and quantitative results have been presented in [19], where the yield criterion proposed in [15] was adopted. The present paper provides another solution. It is also worthy to note that the solution given in [1] has been extended to the double shearing model in [20] and to a viscoplastic model in [21]. The fracture of fibres has not been considered in these works. A description of the double shearing model can be found in [22].

## 2. General Approach

An elegant theory of the failure of ductile materials reinforced by elastic fibres has been proposed in [1]. This theory is outlined in this section to formulate the boundary value problem to be solved. It is assumed that the composite consists of a large number of equal cells, each of which is a hexagonal cylinder of the matrix material containing a concentric circular fibre. A typical cross section of the idealized composite is illustrated in Figure 1. These cells are further idealized replacing the hexagonal cylinders with circular cylinders of the same cross-sectional area. Figure 2 illustrates the cross section of a typical cell that will be used in the mathematical formulation. In particular, the radius of the fibre is denoted by  $a_0$  and the radius of the cell by  $b_0$ . The length of the cell will be denoted by  $2L$ .

It is supposed that the composite is subjected to uniaxial tension applied in the direction parallel to the fibres. The equations for the cell shown in Figure 2 are referred to a cylindrical polar coordinate system  $(r, \theta, z)$  whose origin is located at the centre of the cell and  $z$ -axis lies along the axis of the fibre (Figure 3). The plane  $z = 0$  coincides with the plane of symmetry of the cell. It is assumed that the state of stress is approximately axially symmetric about the  $z$ -axis. Therefore, the nonzero stress components referred to the cylindrical coordinate system are  $\sigma_{rr}$ ,  $\sigma_{\theta\theta}$ ,  $\sigma_{zz}$ , and  $\sigma_{rz}$ . The material of the matrix is isotropic. Therefore, the nonzero strain rate

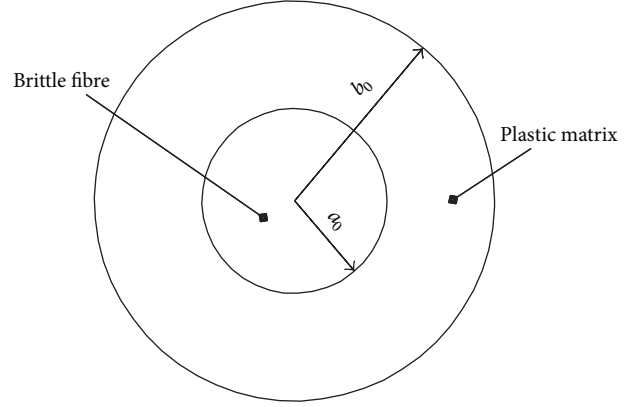


FIGURE 2: Cross section of a typical idealized cell.

components referred to the cylindrical coordinate system are  $\xi_{rr}$ ,  $\xi_{\theta\theta}$ ,  $\xi_{zz}$ , and  $\xi_{rz}$ . Moreover, the circumferential velocity vanishes everywhere. The radial and axial velocities will be denoted by  $u_r$  and  $u_z$ , respectively.

Since the boundary value problem is symmetric about the plane  $z = 0$ , it is sufficient to consider the region  $z \geq 0$ . Based on the assumptions made the following boundary conditions have been formulated in [1]:

$$u_r = -U \quad (1)$$

for  $r = b_0$ ,

$$u_r = 0 \quad (2)$$

for  $r = a_0$ ,

$$u_z = 0 \quad (3)$$

for  $z = 0$ ,

$$\sigma_{rz} = 0 \quad (4)$$

for  $r = b_0$ ,

$$\sigma_{rz} = \tau_f \quad (5)$$

for  $r = a_0$ , and

$$\int_0^L \sigma_{rr}|_{r=b_0} dz = 0. \quad (6)$$

In (5),  $\tau_f$  is the shear yield stress of the matrix. The boundary conditions (1) to (6) should be used to solve the plasticity boundary value problem in the matrix. It is also assumed that the ends of the fibres do not support tensile load (Figure 3). This load is transferred to the fibre only through the shear stress on the contact surface. The resulting force acting in the axial direction at the cross section  $z = L$  is

$$P = 2\pi \int_{a_0}^{b_0} \sigma_{zz}|_{z=L} r dr. \quad (7)$$

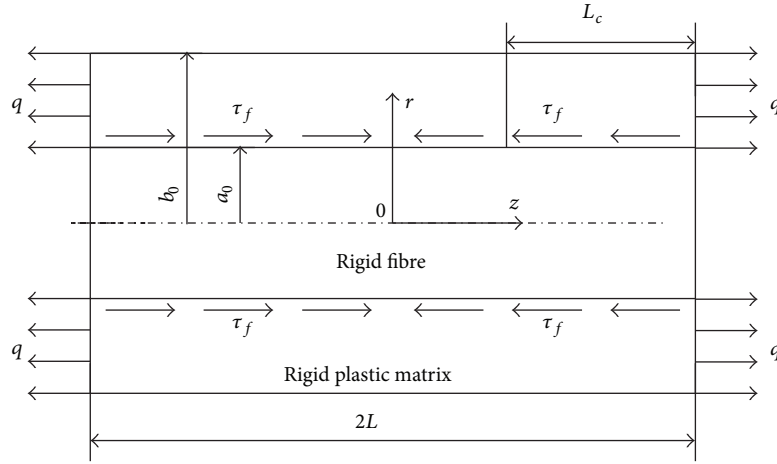


FIGURE 3: Configuration and coordinate system for a typical cell.

Let  $T$  be the mean tensile stress at which the fibre breaks. It has been shown in [1] that failure occurs by plastic flow of the matrix if  $L < L_c$  and by fracture of the fibre if  $L > L_c$  where

$$L_c = \frac{a_0 T}{2\tau_f}. \quad (8)$$

The approach to determining the tensile load at which the fibre breaks is as follows. It is assumed that in the matrix

$$\begin{aligned} \frac{\sigma_{zz}}{\sigma_0} &= 1 + C, \\ \frac{\sigma_{rr}}{\sigma_0} &= \frac{\sigma_{\theta\theta}}{\sigma_0} = C, \\ \sigma_{rz} &= 0 \end{aligned} \quad (9)$$

in the range  $0 \leq z \leq L - L_c$  (Figure 3). Here  $\sigma_0$  is the yield stress in tension and  $C$  is an arbitrary constant. It is evident that the state of stress given by (9) satisfies any yield criterion. The state of stress in the matrix in the range  $L - L_c \leq z \leq L$  should be found from the solution satisfying the boundary conditions (1) to (5). It is then assumed that

$$\left[ \int_{a_0}^{b_0} \sigma_{zz} r dr \right] = 0 \quad (10)$$

at  $L = L_c$ . Here  $[ ]$  denotes the amount of jump in the quantity enclosed in the brackets. Equations (6) and (10) allow the axial stress in the matrix to be determined. Then, (7) can be used to find the tensile load at which the fibre breaks.

The approach outlined in this section has been adopted in [1] in conjunction with Tresca's yield criterion in the matrix. As a result, the dimensionless tensile load at which the fibre breaks has been found as

$$\begin{aligned} \frac{P}{\pi\sigma_0 b_0^2} &= q_s \\ &= (1 - a^2) \left[ 1 - \frac{(2-n)L_c}{2L} \right] + \frac{Ta^2}{\sigma_0} \left( 1 - \frac{L_c}{2L} \right), \end{aligned} \quad (11)$$

where  $a = a_0/b_0$  and  $n$  is a numerical coefficient. This coefficient is given by

$$\begin{aligned} n &= -\frac{1}{2} + \frac{a^2}{(1-a^2)} \ln a - \frac{(1-a^2)}{a^2} \\ &\quad - \frac{(1+a^2)}{(1-a^2)} \left[ a^2 F(\gamma, \phi) - \frac{E(\gamma, \phi)}{a^2} \right]. \end{aligned} \quad (12)$$

Here  $F(\gamma, \phi)$  and  $E(\gamma, \phi)$  are the incomplete elliptic integrals of the first and second kinds, respectively, and

$$\begin{aligned} \gamma &= \sqrt{1-a^4}, \\ \phi &= \arctan\left(\frac{1}{a}\right). \end{aligned} \quad (13)$$

Many materials satisfy other yield criteria compared to that of Tresca. Therefore, it is of interest to correct (11) taking into account a generalized yield criterion or to show that this simple equation is accurate enough for predicting the tensile load at which the fibres breaks. In the present paper, the yield criterion proposed in [15] is adopted.

### 3. Rigid Plastic Solution in the Matrix

Let  $\sigma_1$ ,  $\sigma_2$ , and  $\sigma_3$  be the principal stresses. With no loss of generality it is possible to assume that

$$\sigma_1 \geq \sigma_2 \geq \sigma_3. \quad (14)$$

Then, the yield criterion proposed in [15] can be written as

$$\left[ \frac{(\sigma_1 - \sigma_2)^m + (\sigma_2 - \sigma_3)^m + (\sigma_1 - \sigma_3)^m}{2} \right]^{1/m} = \sigma_0. \quad (15)$$

The associated flow rule is

$$\begin{aligned} \xi_1 &= \lambda \left[ (\sigma_1 - \sigma_2)^{m-1} + (\sigma_1 - \sigma_3)^{m-1} \right], \\ \xi_2 &= \lambda \left[ (\sigma_2 - \sigma_3)^{m-1} - (\sigma_1 - \sigma_2)^{m-1} \right], \\ \xi_3 &= -\lambda \left[ (\sigma_2 - \sigma_3)^{m-1} + (\sigma_1 - \sigma_3)^{m-1} \right], \end{aligned} \quad (16)$$

where  $\xi_1$ ,  $\xi_2$ , and  $\xi_3$  are the principal strain rates and  $\lambda$  is a nonnegative multiplier. Equations (15) and (16) are supplemented with the condition that the principal stress and strain rate directions coincide. In the case under consideration the equilibrium equations in the cylindrical coordinate system are

$$\begin{aligned} \frac{\partial \sigma}{\partial r} + \frac{\partial \tau_{rr}}{\partial r} + \frac{\partial \tau_{rz}}{\partial z} + \frac{\tau_{rr} - \tau_{\theta\theta}}{r} &= 0, \\ \frac{\partial \tau_{rz}}{\partial r} + \frac{\partial \sigma}{\partial z} + \frac{\partial \tau_{zz}}{\partial z} + \frac{\tau_{rz}}{r} &= 0, \end{aligned} \quad (17)$$

where

$$\begin{aligned} \sigma &= \frac{\sigma_1 + \sigma_2 + \sigma_3}{3}, \\ \tau_{rr} &= \sigma_{rr} - \sigma, \\ \tau_{\theta\theta} &= \sigma_{\theta\theta} - \sigma, \\ \tau_{zz} &= \sigma_{zz} - \sigma, \\ \tau_{rz} &= \sigma_{rz}. \end{aligned} \quad (18)$$

It is reasonable to assume that

$$\sigma_2 = \sigma_{\theta\theta}. \quad (19)$$

This assumption should be verified a posteriori. It follows from (15) and (16) that

$$\tau_f = \frac{\sigma_0}{\sqrt[2m]{1 + 2^{m-1}}}. \quad (20)$$

The basic assumption concerning the velocity field is [1]

$$\frac{u_r}{U} = -\eta(\rho), \quad (21)$$

where  $\eta(\rho)$  is a function of  $\rho$  and  $\rho = r/b_0$ . Using (21) the radial and circumferential strain rates are found as

$$\begin{aligned} \xi_{rr} &= -\frac{U}{b_0} \frac{d\eta}{d\rho}, \\ \xi_{\theta\theta} &= -\frac{U}{b_0} \frac{\eta}{\rho}. \end{aligned} \quad (22)$$

Then, the axial strain rate is determined from the incompressibility equations as

$$\xi_{zz} = \frac{U}{b_0 \rho} \frac{d(\eta\rho)}{d\rho}. \quad (23)$$

Since  $\xi_{zz} = \partial u_z / \partial z$  and the right hand side of (23) is independent of  $z$ , this equation can be immediately integrated to give

$$\frac{u_z}{U} = \frac{\zeta}{\rho} \frac{d(\eta\rho)}{d\rho} + \mu(\rho), \quad (24)$$

where  $\zeta = z/b_0$  and  $\mu(\rho)$  is an arbitrary function of its argument. It follows from (21) and (24) that the shear strain rate in the cylindrical coordinate system is

$$\xi_{rz} = \frac{U}{2b_0} \frac{d}{d\rho} \left[ \frac{d(\eta\rho)}{\rho d\rho} \right] \zeta + \frac{U}{2b_0} \frac{d\mu}{d\rho}. \quad (25)$$

Let  $\varphi$  be the inclination of the  $\sigma_1$  principal stress direction to the  $r$ -axis, measured anticlockwise. Then,

$$\tan 2\varphi = \frac{2\tau_{rz}}{\tau_{rr} - \tau_{zz}} = \frac{2\xi_{rz}}{\xi_{rr} - \xi_{zz}}. \quad (26)$$

It follows from (22), (25), and (26) that

$$\tan 2\varphi = -\frac{(d/d\rho) [d(\eta\rho)/\rho d\rho] \zeta + d\mu/d\rho}{[d\eta/d\rho + (1/\rho)(d(\rho\eta)/d\rho)]}. \quad (27)$$

The solution derived in [1] suggests that  $\varphi$  is independent of  $z$ . Then, it follows from (27) that  $d(\eta\rho)/d\rho = 2C\rho$  where  $C$  is constant. Integrating this equation gives

$$\eta = C\rho + \frac{C_1}{\rho}, \quad (28)$$

where  $C_1$  is constant of integration. It is seen from (21) that the boundary conditions (1) and (2) are equivalent to the conditions  $\eta = 1$  for  $\rho = 1$  and  $\eta = 0$  for  $\rho = a$ , respectively. Using these boundary conditions the constants  $C$  and  $C_1$  are determined from (28) as

$$\begin{aligned} C &= \frac{1}{(1-a^2)}, \\ C_1 &= -\frac{a^2}{(1-a^2)}. \end{aligned} \quad (29)$$

Substituting (29) into (28) results in

$$\eta = \frac{(\rho^2 - a^2)}{(1-a^2)\rho}. \quad (30)$$

Substituting (30) into (27) and using (26) result in

$$\frac{2\tau_{rz}}{\tau_{rr} - \tau_{zz}} = \frac{\rho^2 (a^2 - 1) d\mu}{(a^2 + 3\rho^2) d\rho}. \quad (31)$$

It is convenient to introduce the stress variables

$$\begin{aligned} s &= \frac{\sigma_1 + \sigma_3}{2\sigma_0}, \\ t &= \frac{\sigma_1 - \sigma_3}{2\sigma_0}, \\ s_{\theta\theta} &= \frac{\sigma_{\theta\theta}}{\sigma_0}. \end{aligned} \quad (32)$$

It is evident from (14) that  $t > 0$ . Using (32) it is possible to express the stress components in the cylindrical coordinate system as

$$\begin{aligned} \frac{\sigma_{rr}}{\sigma_0} &= s + t \cos 2\varphi, \\ \frac{\sigma_{zz}}{\sigma_0} &= s - t \cos 2\varphi, \\ \frac{\sigma_{rz}}{\sigma_0} &= t \sin 2\varphi. \end{aligned} \quad (33)$$

The direction of flow requires that  $\sigma_{rz} > 0$  (Figure 3). Assume that  $\sigma_{zz} > \sigma_{rr}$ . This assumption should be verified a posteriori. Then, it is possible to find from (32) and (33) that

$$\frac{\pi}{4} \leq \varphi \leq \frac{\pi}{2}. \quad (34)$$

Equation (19) dictates that  $\xi_{\theta\theta} = \xi_2$ . Therefore,

$$\frac{\xi_{rr} - \xi_{zz}}{\xi_{\theta\theta}} = \frac{(\xi_1 - \xi_3)}{\xi_2} \cos 2\varphi. \quad (35)$$

Substituting (16), (22), and (28) into this equation and using (32) and (33) yield

$$\begin{aligned} &\frac{(3\rho^2 + a^2)}{(\rho^2 - a^2)} \\ &= \frac{[(s+t-s_{\theta\theta})^{m-1} + 2(2t)^{m-1} + (s_{\theta\theta}+t-s)^{m-1}] \cos 2\varphi}{[(s_{\theta\theta}-s+t)^{m-1} - (s-s_{\theta\theta}+t)^{m-1}]} \end{aligned} \quad (36)$$

It follows from (19) and (32) that the yield criterion (15) can be rewritten as

$$\left[ \frac{(s+t-s_{\theta\theta})^m + (s_{\theta\theta}-s+t)^m + (2t)^m}{2} \right]^{1/m} = 1. \quad (37)$$

Substituting (33) into the equilibrium equations (17) and assuming that  $t$  is independent of  $z$  yield

$$\begin{aligned} \frac{\partial s}{\partial \rho} + \frac{d(t \cos 2\varphi)}{d\rho} + \frac{s - s_{\theta\theta} + t \cos 2\varphi}{\rho} &= 0, \\ \frac{\partial s}{\partial \zeta} + \frac{d(t \sin 2\varphi)}{d\rho} + \frac{t \sin 2\varphi}{\rho} &= 0. \end{aligned} \quad (38)$$

These equations have a solution if and only if

$$s = C_2(\rho) + C_3\zeta, \quad (39)$$

$$s - s_{\theta\theta} = \beta(\rho),$$

where  $C_3$  is constant and  $C_2(\rho)$  and  $\beta(\rho)$  are arbitrary functions of  $\rho$ . Substituting (39) into (38) results in

$$\frac{d(C_2 + t \cos 2\varphi)}{d\rho} + \frac{\beta(\rho) + t \cos 2\varphi}{\rho} = 0, \quad (40a)$$

$$\frac{d(t \sin 2\varphi)}{d\rho} + \frac{t \sin 2\varphi}{\rho} = -C_3. \quad (40b)$$

Equation (40b) can be immediately integrated to give

$$t \sin 2\varphi = -\frac{C_3\rho}{2} + \frac{C_4}{\rho}, \quad (41)$$

where  $C_4$  is constant of integration. Using (33) the boundary conditions (4) and (5) are transformed to  $t \sin 2\varphi = 0$  for  $\rho = 1$  and  $t \sin 2\varphi = \tau_f/\sigma_0$  for  $\rho = a$ , respectively. These boundary conditions and (41) combine to give

$$C_3 = \frac{2a}{\sqrt[2m]{1 + 2^{m-1}(1-a^2)}}, \quad (42)$$

$$C_4 = \frac{a}{\sqrt[2m]{1 + 2^{m-1}(1-a^2)}}.$$

Therefore, (41) becomes

$$t = \frac{1}{2} \left( \frac{1}{\rho} - \rho \right) \frac{C_3}{\sin 2\varphi}. \quad (43)$$

Eliminating  $t$  and  $s - s_{\theta\theta}$  in (36) and (37) by means of (39) and (43) yields

$$\frac{(3\rho^2 + a^2)}{(\rho^2 - a^2)} = \frac{\left\{ [2\beta\rho \sin 2\varphi + C_3(1-\rho^2)]^{m-1} + 2^m C_3^{m-1} (1-\rho^2)^{m-1} + \dots + [C_3(1-\rho^2) - 2\beta\rho \sin 2\varphi]^{m-1} \right\} \cos 2\varphi}{[C_3(1-\rho^2) - 2\beta\rho \sin 2\varphi]^{m-1} - [2\beta\rho \sin 2\varphi + C_3(1-\rho^2)]^{m-1}}, \quad (44)$$

$$[2\beta\rho \sin 2\varphi + C_3(1-\rho^2)]^m + [C_3(1-\rho^2) - 2\beta\rho \sin 2\varphi]^m + \dots + 2^m C_3^m (1-\rho^2)^m = 2^{m+1} \rho^m \sin^m 2\varphi.$$

Equations (44) should be solved for  $\beta(\rho)$  and  $\varphi(\rho)$  numerically.  $C_3$  should be eliminated by means of (42). Once these equations have been solved,  $t$  can be found from (42) and (43) and, then,  $C_2$  is determined from (40a) as

$$C_2 = -t \cos 2\varphi + \int_a^\rho \frac{(\beta + t \cos 2\varphi)}{\chi} d\chi + C_5. \quad (45)$$

Here  $C_5$  is constant of integration and  $\chi$  is a dummy variable of integration.  $\beta$ ,  $t$ , and  $\varphi$  in the integrand are understood to be functions of  $\chi$ . The state of stress in the matrix is given by (33), (39), and (45). Then,  $C_5$  and  $C$  involved in (9) can be determined by means of the approach outlined in Section 2.

#### 4. Effect of the Yield Criterion of the Matrix on Brittle Fracture of the Fibre

It follows from (33), (39), and (45) that

$$\begin{aligned} \frac{\sigma_{rr}}{\sigma_0} &= C_3 \zeta + \int_a^\rho \frac{(\beta + t \cos 2\varphi)}{\chi} d\chi + C_5, \\ \frac{\sigma_{zz}}{\sigma_0} &= C_3 \zeta - 2t \cos 2\varphi + \int_a^\rho \frac{(\beta + t \cos 2\varphi)}{\chi} d\chi + C_5. \end{aligned} \quad (46)$$

These equations are valid in the range  $L - L_c \leq z \leq L$  (Figure 3). Substituting (9) and (46) into (6) and (10) yields

$$\begin{aligned} C \left( \frac{l}{l_c} - 1 \right) + C_5 & \\ = \frac{C_3}{2} (l_c - 2l) - \int_a^1 \frac{(\beta + t \cos 2\varphi)}{\rho} d\rho, & \quad (47) \\ C - C_5 & \\ = C_3 (l - l_c) - 1 & \\ + \frac{2}{(1 - a^2)} \int_a^1 \rho \int_a^\rho \frac{(\beta + t \cos 2\varphi)}{\chi} d\chi d\rho & \quad (48) \\ - \frac{4}{(1 - a^2)} \int_a^1 \rho t \cos 2\varphi d\rho, & \end{aligned}$$

respectively. Here  $l = L/b_0$  and  $l_c = L_c/b_0$ . Equations (47) and (48) constitute a linear system for  $C$  and  $C_5$ . The solution to this system can be found with no difficulty. Once the value of  $C_5$  has been found,  $P$  and its dimensionless representation,  $q$ , are determined from (7) and (46) as

$$\begin{aligned} \frac{P}{\pi \sigma_0 b_0^2} &= q \\ &= (C_3 l + C_5) (1 - a^2) - 4 \int_a^1 \rho t \cos 2\varphi d\rho \\ &\quad + 2 \int_a^1 \rho \int_a^\rho \frac{(\beta + t \cos 2\varphi)}{\chi} d\chi d\rho. \end{aligned} \quad (49)$$

In order to evaluate the effect of the yield criterion on the tensile force at which the fibre breaks, it is convenient to introduce the parameter  $\delta$  as

$$\delta = \frac{|q - q_s|}{q_s} \cdot 100\%. \quad (50)$$

Equations (44) have been solved numerically in the range  $1.05 \leq m \leq 20$ . Condition (19) has been verified using (32), (33), (39), and (45). Then,  $q$  has been calculated by means of (42), (47), (48), and (49). It has been found by means of (11) and (50) that  $\delta < 1.5\%$  for typical values of  $a$ ,  $l$ , and  $T/\sigma_0$  provided in [1]. Therefore, (11) derived in that paper is a very good approximation for the tensile load at which the fibre breaks independently of the yield criterion of the matrix.

#### 5. Conclusions

Brittle fracture of fibres in continuous fibre reinforced composites subjected to tensile loading in the direction parallel to the fibres has been predicted by means of the theory developed in [1]. A distinguished feature of this new solution is that the generalized yield criterion proposed in [15] has been adopted for the matrix. The solution has been compared to the analytic solution for Tresca's yield criterion derived in [1]. It has been found that the magnitude of the tensile load at which the fibre breaks is practically independent of the yield criterion of the matrix. In particular, formula (11) obtained in [1] predicts this magnitude for any isotropic pressure-independent yield criterion with a very high accuracy. In general, this feature of the solution is capable of experimental verification and hence provides a means for testing the theory. However, such verification requires the determination of the yield criterion of the matrix before testing the composite. To the best of authors' knowledge, no research that includes both testing the matrix material and testing the composite has been reported in the literature. Therefore, the present paper may be considered as an encouragement to experimentalists to attempt to verify the theoretical predictions made.

A new result of academic interest is the solution for the constitutive equations (15) and (16) supplemented with the equilibrium equations and satisfying the boundary conditions (1)–(5). This solution can be regarded as a generalization of the famous Prandtl's solution for plane strain compression of a plastic layer between parallel, rough plates (see, e.g., [23]). In contrast to the plane strain problem, the solution to the axisymmetric problem depends on the yield criterion chosen. A distinguished feature of the present solution is that the generalized yield criterion has been adopted.

#### Competing Interests

The authors declare that they have no competing interests.

#### Acknowledgments

The reported study was funded by RFBR according to the research project no. 16-58-52051.

## References

- [1] A. J. M. Spencer, "A theory of the failure of ductile materials reinforced by elastic fibres," *International Journal of Mechanical Sciences*, vol. 7, no. 3, pp. 197–209, 1965.
- [2] G. J. Dvorak and Y. A. Bahei-El-Din, "Plasticity analysis of fibrous composites," *Journal of Applied Mechanics*, vol. 49, no. 2, pp. 327–335, 1982.
- [3] C. Cheng and N. Aravas, "Creep of metal-matrix composites with elastic fibers—part I: continuous aligned fibers," *International Journal of Solids and Structures*, vol. 34, no. 31–32, pp. 4147–4171, 1997.
- [4] H. Naji, S. M. Zebarjad, and S. A. Sajjadi, "The effects of volume percent and aspect ratio of carbon fiber on fracture toughness of reinforced aluminum matrix composites," *Materials Science and Engineering A*, vol. 486, no. 1–2, pp. 413–420, 2008.
- [5] I. T. Lee, Y. Q. Wang, Y. Ochi, S. I. Bae, K. S. Han, and J. I. Song, "Effect of short fiber reinforcement on the fracture toughness of metal matrix composites," *Advanced Composite Materials*, vol. 19, no. 1, pp. 41–53, 2010.
- [6] S. Ghosh, Y. Ling, B. Majumdar, and R. Kim, "Interfacial debonding analysis in multiple fiber reinforced composites," *Mechanics of Materials*, vol. 32, no. 10, pp. 561–591, 2000.
- [7] A. Caporale, R. Luciano, and E. Sacco, "Micromechanical analysis of interfacial debonding in unidirectional fiber-reinforced composites," *Computers & Structures*, vol. 84, no. 31–32, pp. 2200–2211, 2006.
- [8] S. Li and S. Ghosh, "Modeling interfacial debonding and matrix cracking in fiber reinforced composites by the extended voronoi cell FEM," *Finite Elements in Analysis and Design*, vol. 43, no. 5, pp. 397–410, 2007.
- [9] D. H. Allen, R. H. Jones, and J. G. Boyd, "Micromechanical analysis of a continuous fiber metal matrix composite including the effects of matrix viscoplasticity and evolving damage," *Journal of the Mechanics and Physics of Solids*, vol. 42, no. 3, pp. 505–529, 1994.
- [10] C. R. Ananth, S. R. Voleti, and N. Chandra, "Effect of fiber fracture and interfacial debonding on the evolution of damage in metal matrix composites," *Composites Part A: Applied Science and Manufacturing*, vol. 29, no. 9–10, pp. 1203–1211, 1998.
- [11] Z. P. Luo and C. Y. Sun, "Effect of the interfacial bonding status on the tensile fracture characteristics of a boron-fiber-reinforced aluminum composite," *Materials Characterization*, vol. 50, no. 1, pp. 51–58, 2003.
- [12] S. Fukumoto, A. Hirose, and K. F. Kobayashi, "Evaluation of the strength of diffusion bonded joints in continuous fiber reinforced metal matrix composites," *Journal of Materials Processing Technology*, vol. 68, no. 2, pp. 184–191, 1997.
- [13] T. Pacheco, H. Nayeb-Hashemi, and H. E. M. Sallam, "The effects of matrix and fiber properties on the mechanical behavior and acoustic emission in continuous fiber reinforced metal matrix composites," *Materials Science and Engineering A*, vol. 247, no. 1–2, pp. 88–96, 1998.
- [14] J. L. Bucaille, A. Rossoll, B. Moser, S. Stauss, and J. Michler, "Determination of the matrix in situ flow stress of a continuous fibre reinforced metal matrix composite using instrumented indentation," *Materials Science and Engineering A*, vol. 369, no. 1–2, pp. 82–92, 2004.
- [15] W. F. Hosford, "A generalized Isotropic Yield Criterion," *International Journal of Applied Mechanics*, vol. 39, no. 2, pp. 607–609, 1972.
- [16] W. H. Yang, "A generalized von Mises criterion for yield and fracture," *Journal of Applied Mechanics*, vol. 47, no. 2, pp. 297–300, 1980.
- [17] S. R. Voleti, C. R. Ananth, and N. Chandra, "Effect of fiber fracture and matrix yielding on load sharing in continuous fiber metal matrix composites," *Journal of Composites Technology & Research*, vol. 20, no. 4, pp. 203–209, 1998.
- [18] R. T. Shield, "Plastic flow in a converging conical channel," *Journal of the Mechanics and Physics of Solids*, vol. 3, no. 4, pp. 246–258, 1955.
- [19] S. Alexandrov and F. Barlat, "Modeling axisymmetric flow through a converging channel with an arbitrary yield condition," *Acta Mechanica*, vol. 133, no. 1–4, pp. 57–68, 1999.
- [20] S. E. Aleksandrov and R. V. Goldstein, "Generalization of the prandtl solution to the case of axisymmetric deformation of materials obeying the double shear model," *Mechanics of Solids*, vol. 47, no. 6, pp. 654–664, 2012.
- [21] S. Alexandrov and Y.-R. Jeng, "A generalization of Prandtl's and Spencer's solutions on axisymmetric viscous flow," *Archive of Applied Mechanics*, vol. 81, no. 4, pp. 437–449, 2011.
- [22] A. J. M. Spencer, "Deformation of ideal granular materials," in *Mechanics of Solids: The Rodney Hill 60th Anniversary Volume*, H. G. Hopkins and M. J. Sewell, Eds., pp. 607–652, Pergamon Press, Oxford, UK, 1982.
- [23] R. Hill, *The Mathematical Theory of Plasticity*, Clarendon Press, Oxford, UK, 1950.

## Research Article

# Mechanical Behavior of 3D Crack Growth in Transparent Rock-Like Material Containing Preexisting Flaws under Compression

Hu-Dan Tang,<sup>1,2</sup> Zhen-De Zhu,<sup>1</sup> Ming-Li Zhu,<sup>3</sup> and Heng-Xing Lin<sup>4</sup>

<sup>1</sup>Key Laboratory of Ministry of Education for Geomechanics and Embankment Engineering, Institute of Safety and Disaster Prevention Engineering, Hohai University, Nanjing, Jiangsu 210098, China

<sup>2</sup>School of Civil Engineering, Henan Polytechnic University, Jiaozuo, Henan 454000, China

<sup>3</sup>School of Energy Science and Engineering, Henan Polytechnic University, Jiaozuo, Henan 454000, China

<sup>4</sup>Water Conservancy Project Planning and Design Departments, Shanghai Investigation Design & Research Institute Co. Ltd., Shanghai 200434, China

Correspondence should be addressed to Hu-Dan Tang; tanghudan@126.com

Received 23 September 2015; Accepted 22 November 2015

Academic Editor: Liviu Marsavina

Copyright © 2015 Hu-Dan Tang et al. This is an open access article distributed under the Creative Commons Attribution License, which permits unrestricted use, distribution, and reproduction in any medium, provided the original work is properly cited.

Mechanical behavior of 3D crack propagation and coalescence is investigated in rock-like material under uniaxial compression. A new transparent rock-like material is developed and a series of uniaxial compressive tests on low temperature transparent resin materials with preexisting 3D flaws are performed in laboratory, with changing values of bridge angle  $\beta$  (inclination between the inner tips of the two preexisting flaws) of preexisting flaws in specimens. Furthermore, a theoretical peak strength prediction of 3D cracks coalescence is given. The results show that the coalescence modes of the specimens are varying according to different bridge angles. And the theoretical peak strength prediction agrees well with the experimental observation.

## 1. Introduction

Most of the elastic-brittle materials contain different patterns of flaws. In general, the mechanical behavior of brittle materials may be affected by the micromechanical behavior of the defects. The evolution of cracks depends on the properties of cracks such as size, location, orientation, and loading condition. The propagation of cracks plays a vital role in predicting the breakage process of rock specimens [1–12]. As a rule, the fracture surface is perpendicular to the maximum tensile stress direction. The experimental and theoretical research have shown that microcracks developed in different ways, such as tensile cracks, mixture cracks (tensile cracks, and shear cracks), and shear cracks, and became closed, frictional sliding, intergranular propagating, and kink propagating [13–15]. In the crack evolution process of brittle materials containing preexisting flaws, usually two types of crack are observed, which are wing cracks originating from the tips of preexisting flaws and secondary cracks. Wing

cracks are usually caused by tension, while secondary cracks may develop due to shear [16]. Wing cracks initiation in rocks is favored with respect to secondary cracks because of lower toughness of the materials in tension than in shear [17–20]. It is mainly expected that crack initiation follows the direction parallel to the maximum compressive load [21]. Many experiments have been conducted to study the crack initiation, propagation path, and eventual coalescence of the preexisting flaws in specimens made of various substance, including natural rocks or rock-like materials under tensile and compressive loadings [4, 22–24].

From the practical point of view, nearly all rock engineering projects involve, to a certain extent, construction of structures in or on rock masses, which contain different types of flaws. As underground excavations progress into deeper and more complex geological environments, the eventual and ultimate limitation in all mining is depth [24]. Excavation-induced macroscale fractures, such as roof fall, side wall slab, and rock burst [25–29], occur extensively in the side walls

of underground working face. Understanding of the failure modes around cavities in brittle rocks under compressive loading conditions becomes more and more important in searching solutions to the problem that engineering meets.

Fracture propagation leading to rock failure is a very important topic in rock mechanics research. A number of studies have been done on two-dimensional models plate with preexisting flaws. Crack initiation, propagation, and coalescence have been subjects of intensive investigation in rock mechanics, both theoretically and experimentally. The first theoretical study on the growth of preexisting two-dimensional flaws was put forward by Griffith [30, 31]. Griffith [30] further introduced the concept of critical energy release rate and the crack tip stress intensity factor ( $K$ ). Relating to the field of rock mechanics, many experimental studies have been conducted to investigate the crack initiation, propagation, and interaction [1–12, 32, 33]. A number of studies have been done on two-dimensional (2D) model plates with throughgoing preexisting fractures, but as is known rock masses contain some finite size of flaws (three-dimensional (3D) flaws) existing inside or on the surface of rock materials. In terms of rock experiments, due to the nontransparency of rock material, it is difficult to trace the initiation, propagation, and interaction of fractures within the rock. That is to say, the crack growth analyses based on 2D model may not truly reflect the real failure properties. Then some studies have been done on 3D specimens [5, 34–46]. In reality, preexisting fractures are 3D in nature.

Recently, several experiments according 3D crack evolution have been investigated at the Rock Mechanics Laboratory at Hong Kong Polytechnic University. Samples that were prepared in the experiments included a variety of real rocks, PMMA, cement, gypsum, and resin samples. All samples contained a preexisting flaw [40–44]. According to these experiments, both wing cracks and petal cracks initiated from preexisting flaw tips of PMMA and marble samples, and shell-like cracks emerged from the flaw tips of the two materials referred to above sometimes. At the same time, antiwing cracks (opposite to the wing cracks) were induced from the tips of preexisting flaw at a certain distance in compressive stress zone in gabbros specimens [42, 43]. Liu et al. conducted a series of experimental tests to study 3D cracks propagation progress of a single surface flaw under the conditions of biaxial compression [44], and a 3D acoustic emission (AE) location system was used [42, 44].

However, most of previous studies were focused on the mechanisms and experiments of crack initiation, propagation, and interaction according to 2D cracks. Although some of significant results have been achieved, there were some deviations between the research results and the truth due to the nature of the material itself, the mechanisms of propagation and coalescence of 3D internal flaws are still not clear until now, and no existing theoretical explanation of 3D crack evolution was given.

Therefore, we attempt here to give a more refined study on the pattern of 3D crack initiation, propagation, and coalescence of transparent materials like rocks. On the basis of previous studies, the modeling material used in the paper is improved by being randomly embedded inside transparent

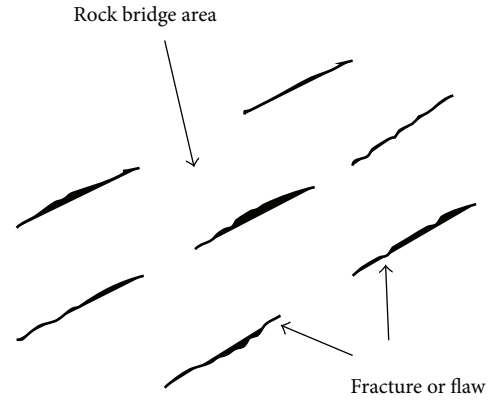


FIGURE 1: Rock bridge area in discontinuous rock.

resin material, certain aggregates of different sizes, and then heterogeneous transparent materials are obtained and successfully deal with the disadvantages of transparent materials which are isotropic. Experimental studies have shown newly developed transparent nonhomogeneous material properties close to real rocks, for the study of internal crack of rock which is no doubt highly beneficial. Due to fine brittle and transparency of the material, the internal crack growth can be clearly seen. Then the crack extension of the materials containing two preexisting flaws is investigated under uniaxial compression, with changing rock bridge angles, and rock bridge area is defined as shown in Figure 1; different modes of crack coalescence are observed in the 3D preexisting flaws specimens. Another main purpose of the paper is to predict the peak strength of transparent rock-like material containing preexisting flaws.

## 2. Sample Preparation and Experimental Technique

The discussion of the sample preparation and experimental technical contains three sections. The first section is the preparation of transparent casting resin modeling material; the second part is design of preexisting flaws in the samples; the third section is about the testing apparatus.

*2.1. Preparation of Transparent Casting Resin Modeling Material Specimen.* In the experiment, a new unsaturated resin is used to make specimens; sixty transparent rock-like parallelepiped samples are prepared and with cross section dimensions of 50 mm × 50 mm and a height of 100 mm are used. The mica sheet is fixed inside the mould through fine cotton according the needed angle. The precise calculation ratio of liquid resin is poured into the mould mica sheet fixed. Some aggregates with different particle sizes are randomly embedded inside the transparent resin material in the process of casting resin material modeling. At room temperature for 24 hours, the specimens are taken out from the mould. After repeatedly baking in the oven for 3 to 5 times, with each baking time about 30 minutes, the specimens are freezing to  $-30^{\circ}\text{C}$ , and then this material is perfectly brittle, deforms without barreling, and has linear stress-strain behavior up to

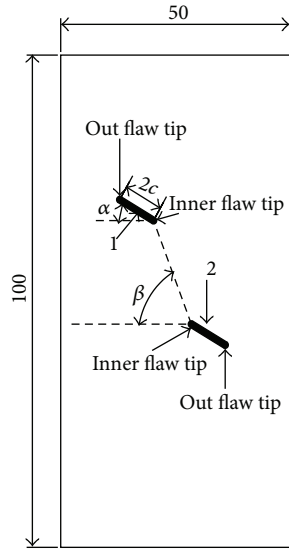


FIGURE 2: A specimen containing two preexisting flaws: the inclination is  $\alpha$ , the rock bridge angle is  $\beta$ , the length of the preexisting flaw is  $2c$ , and the location of inner and outer flaw tips is defined.

its burst-like fracture. The mechanical properties evaluated during the tests are as follows: Young's modulus  $E = 7.553$  GPa; uniaxial compressive strength  $\sigma_c = 93.488$  MPa; fracture toughness  $K_{IC} = 0.6$  MPa·m<sup>1/2</sup>.

**2.2. Design of Preexisting Flaws.** A thin mica film (the thickness of 0.1 mm) is used to model internal preexisting flaw during casting and be hold in the mould by cotton threads; it can represent a native open fracture of the rocks better for smaller stiffness than copper. The sizes of elliptical preexisting flaw are long axis  $2c$  of 12 mm and short axis  $2b$  of 8 mm. The positions and orientations of the slots are predetermined to give the inclination of the cracks ( $\alpha = 30^\circ$ ) and different rock bridge angle ( $\beta$ ), which is the relative inclination between the cracks. For the sake of later discussions, the flaws are labeled as 1, 2. Three different bridge angles are used in the experiment, which are  $60^\circ$ ,  $85^\circ$ , and  $110^\circ$ , as well as integrated species. Therefore, we can investigate the cracks coalescence along different rock bridge angles, as illustrated in Figure 2.

**2.3. Testing Apparatus.** The uniaxial compression test is carried out with RMT-150B multifunction automatic rigid rock servo material testing machine (Figure 3). Displacement control mode is adopted as the load method in this experiment. The specimens are loaded to fail at a minimum loading speed of 0.01 mm/s. The loading system records the values of load, displacement, and other parameters and draws the curve of load-displacement instantaneously. A video camera is connected to the microscope and all the images are transferred to a computer instantaneously, so that the process of crack evolution can be analyzed conveniently after testing.

### 3. Results and Analysis

Three types of models containing different rock bridge angles are tested to investigate the development of 3D fracture patterns. The following three sections depict the crack initiation, propagation, and coalescence of transparent resin materials with preexisting 3D cracks. The first section is general experimental observation; the second section is different model of crack coalescence for specimens containing different rock bridge angles; the third one is peak strength of 3D preexisting flaws specimens.

**3.1. General Experimental Observation.** Specimen with double preexisting flaws is experienced process of pressure elastic deformation, crack expansion, brittle failure, and residual strength on the whole. The coalescence of the specimen has much to do with the rock bridge angles.

Now the crack propagation process of specimen rock bridge angle  $85^\circ$  is described in detail. According to the loading record and images obtained in the loading process, first stage is pressure dense phase and then the elastic deformation; when the stress reaches about 50% of the peak strength, the crack initiation appears first as a sudden at the inner tips of preexisting crack 1 in the form of leaping and is about half the length of the prefabricated crack axis; the typical pattern of wing crack is shown in Figure 4(a). The wrapping wing cracks then start to curve around the preexisting flaw boundary. When the stress reaches about 60% of the peak strength, the crack emerges from the tips of preexisting flaw 2 as a sudden, and the length is roughly the same as the length of axis. With loading increasing, the wing crack emerges from lower tip of preexisting flaw 1 and the upper tip of preexisting flaw 2 and grows in a stable way; later, different from the results of 2D crack growing, antiwing wrapping crack (its growth direction is opposite to the wing wrapping crack) is induced from preexisting flaw 2, but the growing length is limited, as long as one-third of length of the short axis. At the same time, the wing cracks, respectively, from the upper tip of preexisting flaw 2 and lower tips of preexisting flaw 1 are growing towards each other but not coalescence. When the stress reaches about 70% of the peak strength, a tiny type tension crack turns up in the middle part of rock bridge area; ultimately the growing of the secondary crack and the propagation of wing cracks lead to the coalescence of crack induced by the preexisting flaws. When the stress reaches about 75% of the peak strength, cracks begin to grow from the upper tip of preexisting flaw 1. When the stress reaches about 90% of the peak strength, cracks come up in the no fissure zone and are quickly growing connecting with the cracks induced by the preexisting flaws. When the stress falls to about 20% of the peak strength, the effective bearing load area between particles is gradually reduced, and the specimen eventually damages, as shown in Figures 4(a) and 4(a').

The earlier stage of crack evolution of specimens with rock bridge angle  $110^\circ$  has little difference from the one with rock bridge angle  $85^\circ$ . The wrapping wing cracks all come up from the inner tips of the preexisting flaws. The difference is that no secondary cracks are produced in the area of rock bridge during the process of crack growing, but the eventual

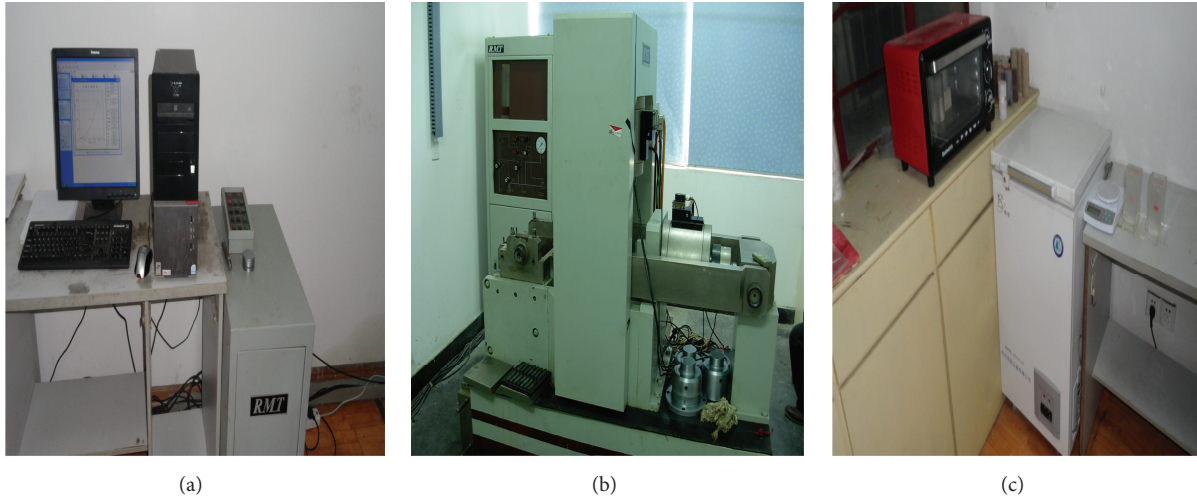


FIGURE 3: Test equipment: (a) data logger of RMT-150B multifunction automatic rigid rock servo material testing machine, (b) loading system of RMT-150B multifunction automatic rigid rock servo material testing machine, and (c) oven, which is used to test sample, make its curing as soon as possible, and increase its brittleness.

fracture is caused by wing cracks growing. That is to say, changing rock bridge angles will produce different mode of crack coalescence. As shown in Figures 4(b) and 4(b'), when loading is going on, the wing cracks start to curve towards the direction of loading, and wing crack plays a vital role in rock fracture.

The early stage of crack extension mode with bridge angle  $60^\circ$  resembles rock bridge angles  $85^\circ$  and  $110^\circ$  of the specimens; wing crack emerges from the inner and outer tips of crack 1 and crack 2 long axis one after another. When the stress reaches about 70% of the peak strength, secondary cracks emerge from the inner tips of crack 1 and crack 2, respectively. With loading increasing, when the stress reaches about 70% of the peak strength, cracks are growing quickly and begin coalescence in rock bridge area. Eventually they damage and form a shear failure surface, as shown in Figures 4(c) and 4(c').

In general, most cracks initiation appeared first at the inner tips of the preexisting flaws; then growth follows at the outer tips of the preexisting flaws, but some cracks initiation occurs in the reverse order, growth at the inner tips followed by cracks initiated at the outer tips. The growth of cracks at the outer tips is faster than that observed at inner tips. The types of cracking in rock bridge area can appear as either shear, tensile, or mix of both modes of crack coalescence. Shear cracks initiate in two different directions: coplanar or quasi-coplanar and oblique to the flaw [43]. A detailed discussion will be present in the next section.

#### 4. The Modes of Crack Coalescence in Rock Bridge Area

In 2D modes, Wong and Chau [46] concluded that there were three modes of coalescence in rock bridge area. Patterns of crack coalescence of sandstone-like material containing two parallel inclined frictional cracks under uniaxial compression

load are shown in Figure 5. The influence roles of the possible orientations of cracks included the values of inclination of preexisting cracks  $\alpha$ , bridge angle  $\beta$ , and the frictional coefficient  $\mu$  on the surfaces of the two preexisting cracks. When crack coalescence occurs, three main types of cracking can be identified in the rock bridge area: wing cracks, which are tensile in nature; secondary cracks, which are mainly shear in nature and are normally parallel to the preexisting cracks; mixed shear/tensile crack coalescence. In all, three main modes are as follows: S-mode (shear crack coalescence), M-mode (mixed shear/tensile crack coalescence), and W-mode (wing tensile crack coalescence), as can be seen in Figure 5. According to the loading record, our interest is placed on the coalescence pattern in the rock bridge area. When the bridge angle is  $85^\circ$  and when the stress reaches about 70% of the peak strength, a tiny secondary crack turns up in the middle part of rock bridge area; ultimately the growing of the secondary crack and the propagation of wing cracks lead to the coalescence of crack induced by the preexisting flaws. As can be seen in Figures 4(a) and 6(a), contrasting with the modes of 2D crack coalescence concluded by Wong, when  $\alpha = 30^\circ$ ,  $\beta = 85^\circ$ , the observations are resemblance as the situation shown in Figure 5(b). And the mode is M-mode (mixed shear and tensile crack coalescence). When the rock bridge angle is  $110^\circ$ , under uniaxial compression load, wing cracks initiate and grow from tips of preexisting cracks. Wing cracks from the inner tip of crack 1 propagate downward to the outer tip of crack 2; at the same time, wing cracks from outer tip of crack 2 propagate upward to the inner tip of crack 1.

However, the specimens failed by axial splitting rather than localized coalescence failure. As shown in Figures 4(b) and 6(b), comparison with the coalescence mode of 2D crack induced which is proposed by Wong, seen in Figure 5(f), this crack coalescence mode is W-mode (wing tensile crack coalescence). When the rock bridge angle is about  $60^\circ$ , wing cracks nucleation at both inner and outer tips of the

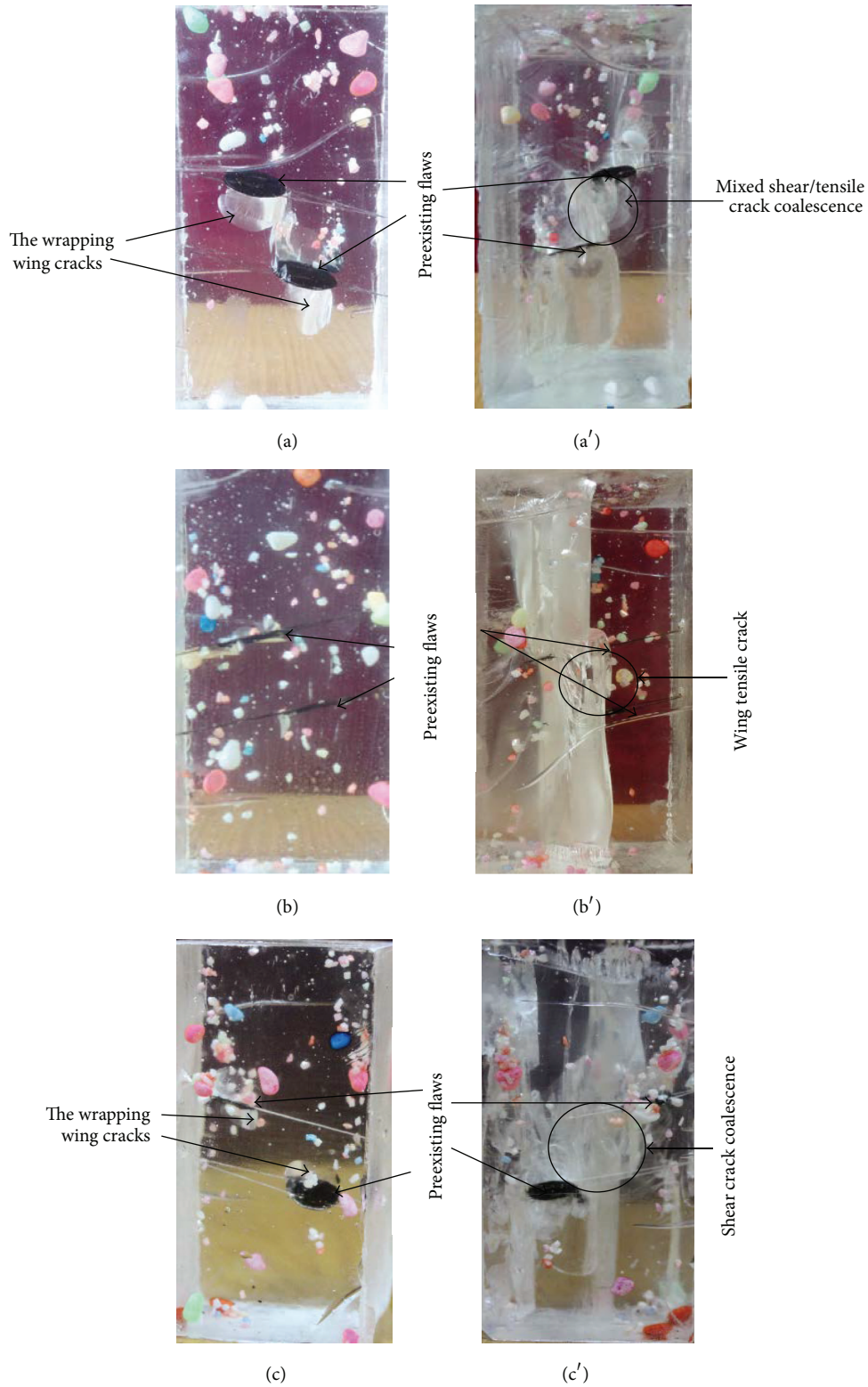


FIGURE 4: Modes of crack coalescence with different rock bridge angles: the inclination angle is about  $30^\circ$ ; the frictional coefficient  $\mu$  is about 0.577. (a) Showing the early stage of crack coalescence process under uniaxial compression when rock bridge angle is  $85^\circ$ , (a') showing the failure of the specimen under uniaxial compression when rock bridge angle is  $85^\circ$ ; (b) showing the early stage of crack coalescence process under uniaxial compression when rock bridge angle is  $110^\circ$ , (b') showing the failure of the specimen under uniaxial compression when rock bridge angle is  $110^\circ$ ; (c) showing the early stage of crack coalescence process under uniaxial compression when rock bridge angle is  $60^\circ$ , (c') showing the failure of the specimen under uniaxial compression when rock bridge angle is  $60^\circ$ .

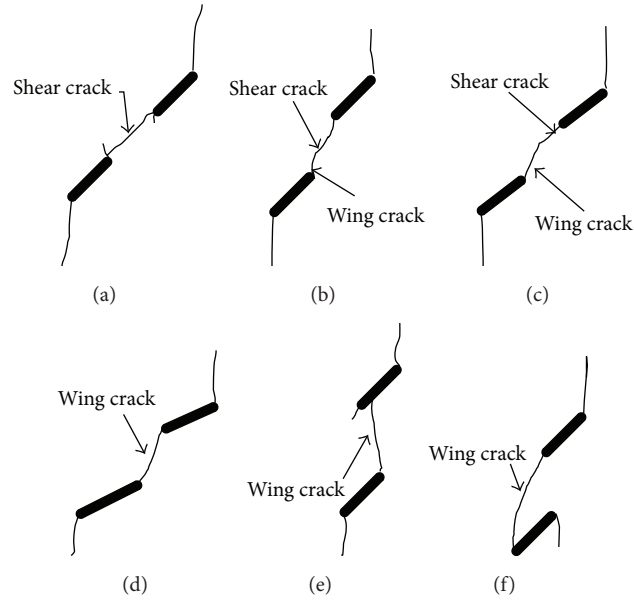


FIGURE 5: Six different patterns of crack coalescence were observed in the 2-flaw specimens. The notion of S, M, and W indicated the shear mode crack coalescence, mixed (shear/tensile) mode crack coalescence, and wing tensile mode crack coalescence (after Wong and Chau [46]).

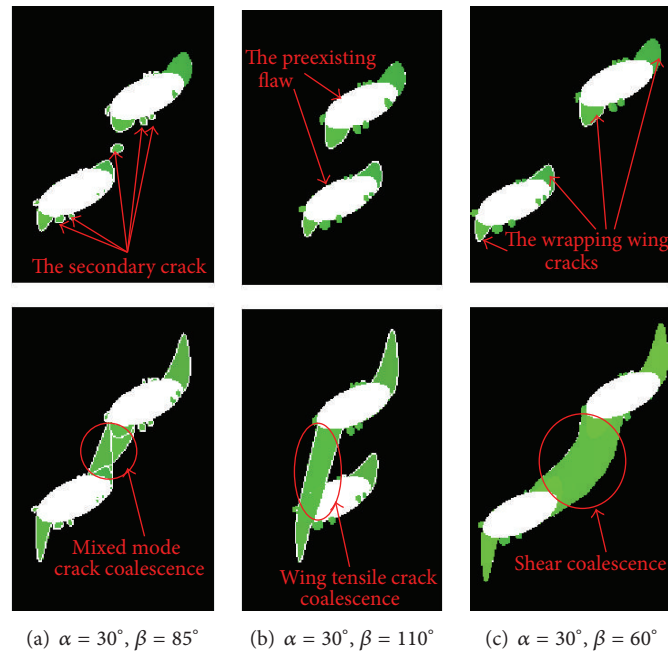


FIGURE 6: Three different patterns of 3D crack coalescence are observed in the tests.

preexisting crack normally occurs first, but before the wing cracks propagate further, secondary shear cracks nucleate from both kinks at inner tips. The secondary cracks nucleate from both kinks at tips. The propagation of these secondary cracks leads to shear coalescence in the rock bridge area while wing cracks spread to the edges of the specimen, as shown in Figures 4(c) and 6(c), and shear failure surface is

formed eventually. This kind of coalescence is mainly induced by a high shear stress concentration in the bridge area. Our observations suggest that whenever the two preexisting main cracks are in alignment, the shear interactions between the preexisting cracks become dominant. In contrast with the coalescence mode of 2D crack induced which is proposed by Wong, seen in Figures 4(c) and 6(c), this crack coalescence

mode is S-mode (shear crack coalescence), but there are some differences that the dominant induced role is shear stress, but the effect of tensile cannot be neglected.

## 5. Peak Strength of Specimen with Flaws

Peak strength prediction of rock containing preexisting flaws is discussed in this section. The mode raised by Ashby and Hallam [47] is employed. Ashby and Hallam derived the following approximate for wing cracks growing, which nucleated from a preexisting inclined crack of length  $2c$  when the specimen was subject to uniaxial compression strength  $\sigma_1$ :

$$\begin{aligned} \frac{K_I}{\sigma_1 \sqrt{\pi c}} &= \frac{(\sin 2\psi - \mu + \mu \cos 2\psi)}{(1 + L)^{3/2}} \left[ 0.23L + \frac{1}{\sqrt{3}(1 + L)^{1/2}} \right] \\ &+ \left[ \frac{2\varepsilon_0 (L + \cos \psi)}{\pi} \right]^{1/2}, \end{aligned} \quad (1)$$

where  $\sigma_1$  is the uniaxial compression strength,  $\psi$  is the angle measured from the  $\sigma_1$ -direction along the main surface of the flaw ( $\psi = 90^\circ - \alpha$ ),  $2c$  is the length of the preexisting flaw, and the flaw density  $\varepsilon_0$  is defined as  $Nc^2/A$  ( $N$  is the number of flaw per area  $A$ ). Although strictly speaking (1) is for the case of multiple initial flaws, it was found that it also can be employed for the specimen containing two flaws. Thus, the peak uniaxial compressive strength  $\sigma_1^{\max}$  of a flawed specimen can be estimated by Wong and Chau [46]:

$$\begin{aligned} \sigma_1^{\max} &= \frac{K_{IC}}{\sqrt{\pi c}} \left\{ \frac{[\sin 2\psi - \mu + \mu \cos 2\psi]}{(1 + L_{cr})^{3/2}} \left[ 0.23L_{cr} \right. \right. \\ &\left. \left. + \frac{1}{\sqrt{3}(1 + L_{cr})^{1/2}} \right] + \left[ \frac{2\varepsilon_0 (L_{cr} + \cos \psi)}{\pi} \right]^{1/2} \right\}^{-1}, \end{aligned} \quad (2)$$

where  $K_{IC}$  is the fracture toughness (in this paper  $K_{IC} = 0.6 \text{ MPa}\cdot\text{m}^{1/2}$  for our modeling material),  $L_{cr} = l_{\max}/c$  ( $l_{\max} = 2b \sin \beta$  is the maximum possible value for length of the coalesced wing cracks, and  $2b$  is the distance between the two flaws), and  $\mu$  is the frictional coefficient along the main shear crack; the orientation of the shear crack for which the nucleation of the wing crack is most favorable is given by  $2\psi = \tan^{-1}(1/\mu)$ .

In this paper, the initial flaw density of specimen containing two flaws is  $e_0 = 0.015$  ( $\varepsilon_0 = Nc^2/A$ ; note that  $N = 2$ ,  $A = 0.05 \text{ m} \times 0.10 \text{ m}$ , and  $c = 0.004 \text{ m}$ ). Predictions of the normalized peak strength ( $\sigma_1^{\max} \sqrt{\pi c}/K_{IC}$ ) by using (2) are listed in Table 1; furthermore the relationship between stress and strain of experimental results with different rock bridge

TABLE 1: Mechanical parameters of specimens with preexisting cracks of different bridge angles.

$\beta$ ( $^\circ$ )	Peak strength		$\varepsilon/10^{-3}$	$E/\text{GPa}$
	Experimental	Theoretical		
Complete specimen	21.46	—	16.08	6.15
60	13.13	10.09	15.12	5.33
85	12.86	16.51	14.04	5.15
110	12.71	13.68	14.65	5.21

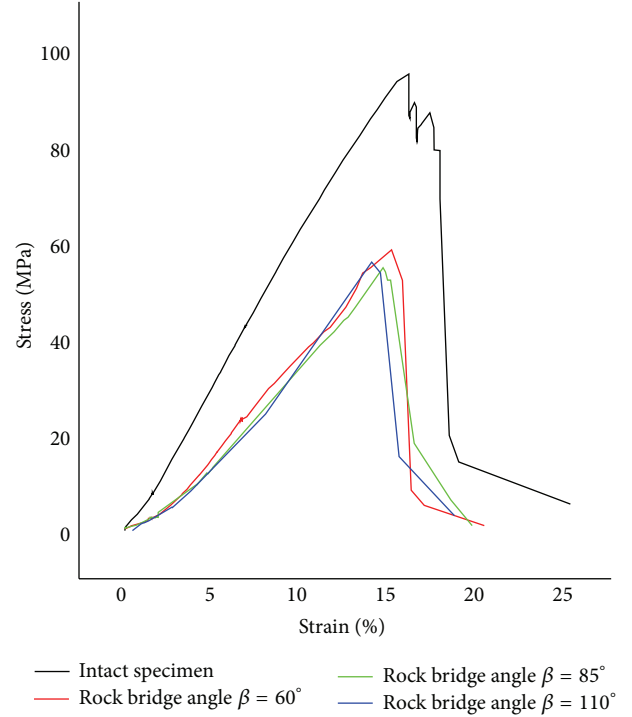


FIGURE 7: Stress and strain curves of samples with preexisting cracks of different bridge angles.

angles is compared (see in Figure 7). As given in (1), the former part of the formula,

$$\begin{aligned} \frac{K_I}{\sigma_1 \sqrt{\pi c}} &= \frac{(\sin 2\psi - \mu + \mu \cos 2\psi)}{(1 + L)^{3/2}} \left[ 0.23L + \frac{1}{\sqrt{3}(1 + L)^{1/2}} \right]. \end{aligned} \quad (3)$$

Equation (3) was derived by Ashby and Hallam, which is an approximate expression for mode I stress intensity factor  $K_I$  at the tip of the wing cracks, and the wing cracks nucleate from a preexisting inclined crack of length  $2c$  when the solid is subject to uniaxial compression strength  $\sigma_1$ .

If peak strength is to be predicted, crack interaction and coalescence must be incorporated into the analysis. Using beam theory, the following  $K_I$  is due to crack interactions

using beam theory, as can be seen from the later part of (2), and written as follows:

$$\frac{K_I}{\sigma_1 \sqrt{\pi c}} = \left\{ \frac{2e_0 (L + \cos \psi)}{\pi} \right\}^{1/2}. \quad (4)$$

Combining (3) and (4) gives the total stress intensity factor  $K_I$  for the wing cracks with crack interaction. Equation (3) completes the elastic theory for cracks. But, as known, rock materials can become plastic if the compressive stress is large enough. When a beam of thickness  $t$  and depth  $b$  is subjected to an axial stress  $\sigma_1$  and a bending moment  $m$ , it starts to yield when the maximum surface stress reaches the yield strength. Hence, an additional contribution to stress intensity can be written as (4). But as shown in Figure 7, the transparent resin material undergoes elastic deformation dominantly; it suffers axial compression load but no significant bending. In other words, stress-strain curves are typical of brittle behavior: the nonlinear strain before peak strength is fairly small, and resistance drops dramatically afterwards. So the influence of beam is negligible, and the equation which can be applied in the study is (3). However, some modification has been made about the equation; that is, when  $\alpha < 45^\circ$ ,  $|\cos 2\psi|$  should be applied. The experimental observations and theoretical results of peak strength of specimens are shown in Table 1.

The prediction by using the Ashby-Hallam model [46], which is description in the previous section, is presented here for comparison, as shown in Table 1; it is clear to see that the predicted theoretical peak strength agrees well with the experimental observation, but some deviations still exist in the modified model. For example, the intensity tendency does not perfectly agree with the result of the experiment. Furthermore, the Ashby-Hallam model should not be applied without modification when the inclination of preexisting flaws  $\alpha < 45^\circ$  and the modification to be made requires more detailed analysis in the future.

## 6. Conclusion

In this paper, experimental results on the mechanism of 3D crack propagation and coalescence as well as the peak strength of transparent rock-like material containing preexisting flaws under uniaxial compression are presented. The specimens used in this study are made of frozen transparent resin material with different rock bridge angles; the following is found:

- (i) It can be observed that coalescence in 3D flaws with different rock bridge angles can be identified as the shear mode, the mixed mode (tensile mode and shear mode), and wing tensile mode. When the inclination angle  $\alpha = 30^\circ$  and frictional coefficient  $\mu = 0.57$ , the coalescence mode is dominated by different rock bridge angles. When  $\beta = 60^\circ$ , shear mode coalescence occurs; when  $\beta = 85^\circ$ , mixed mode coalescence occurs; when  $\beta = 110^\circ$ , wing tensile mode coalescence occurs. Nevertheless, more 3D experimental and theoretical studies need to be carried out.
- (ii) The existence of flaws greatly reduces the compression strength of the specimen, and the cracks existing

make the peak strengths reduced. The uniaxial peak strength prediction of 3D cracks by Ashby-Hallam [46] compares well with the experimental result. And there is some modification of the mode which has been made. Nevertheless, further modification should be done to give a better prediction of peak strength.

## Conflict of Interests

The authors declare that there is no conflict of interests regarding the publication of this paper.

## Acknowledgments

The authors are grateful for the support of this work by the Natural Science Foundation of China (nos. 51404095, 51379065, and 41272329), the Chinese National Key Fundamental Research 973 Programme (2011CB013504), Colleges and Universities in Henan Province, the Construction of Deep Mine Open and Key Laboratory Open Fund (2013KF-06), the Education Department of Henan Province Science and Technology Research Projects (13B560040), and Scientific Research Foundation of Henan Polytechnic University, Dr. (B2011-105).

## References

- [1] Y. Ichikawa, K. Kawamura, K. Uesugi, Y.-S. Seo, and N. Fujii, "Micro- and macrobehavior of granitic rock: observations and viscoelastic homogenization analysis," *Computer Methods in Applied Mechanics and Engineering*, vol. 191, no. 1-2, pp. 47-72, 2001.
- [2] H. Haeri, K. Shahriar, M. F. Marji, and P. Moarefvand, "Cracks coalescence mechanism and cracks propagation paths in rock-like specimens containing pre-existing random cracks under compression," *Journal of Central South University*, vol. 21, no. 6, pp. 2404-2414, 2014.
- [3] A. Bobet, "The initiation of secondary cracks in compression," *Engineering Fracture Mechanics*, vol. 66, no. 2, pp. 187-219, 2000.
- [4] R. H. C. Wong, K. T. Chau, C. A. Tang, and P. Lin, "Analysis of crack coalescence in rock-like materials containing three flaws—part I: experimental approach," *International Journal of Rock Mechanics and Mining Sciences*, vol. 38, no. 7, pp. 909-924, 2001.
- [5] E. Sahouryeh, A. V. Dyskin, and L. N. Germanovich, "Crack growth under biaxial compression," *Engineering Fracture Mechanics*, vol. 69, no. 18, pp. 2187-2198, 2002.
- [6] Y.-P. Li, L.-Z. Chen, and Y.-H. Wang, "Experimental research on pre-cracked marble under compression," *International Journal of Solids and Structures*, vol. 42, no. 9-10, pp. 2505-2516, 2005.
- [7] L. N. Y. Wong and H. H. Einstein, "Crack coalescence in molded gypsum and Carrara marble: part 1. Macroscopic observations and interpretation," *Rock Mechanics and Rock Engineering*, vol. 42, no. 3, pp. 475-511, 2009.
- [8] L. N. Y. Wong and H. H. Einstein, "Crack coalescence in molded gypsum and Carrara marble: part 2—Microscopic observations and interpretation," *Rock Mechanics and Rock Engineering*, vol. 42, no. 3, pp. 513-545, 2009.

- [9] C. H. Park and A. Bobet, "Crack coalescence in specimens with open and closed flaws: a comparison," *International Journal of Rock Mechanics and Mining Sciences*, vol. 46, no. 5, pp. 819–829, 2009.
- [10] T. Y. Ko, H. H. Einstein, and J. Kemeny, "Crack coalescence in brittle material under cyclic loading," in *Proceedings of the 41st US Symposium on Rock Mechanics*, ARMA-06-930, Golden, Colo, USA, June 2006.
- [11] C. H. Park and A. Bobet, "Crack initiation, propagation and coalescence from frictional flaws in uniaxial compression," *Engineering Fracture Mechanics*, vol. 77, no. 14, pp. 2727–2748, 2010.
- [12] C.-a. Tang and Y.-f. Yang, "Crack branching mechanism of rock-like quasi-brittle materials under dynamic stress," *Journal of Central South University*, vol. 19, no. 11, pp. 3273–3284, 2012.
- [13] H. Li and L. N. Y. Wong, "Influence of flaw inclination angle and loading condition on crack initiation and propagation," *International Journal of Solids and Structures*, vol. 49, no. 18, pp. 2482–2499, 2012.
- [14] H. Haeri, K. Shahriar, M. F. Marji, and P. Moarefvand, "A coupled numerical-experimental study of the breakage process of brittle substances," *Arabian Journal of Geosciences*, vol. 8, no. 2, pp. 809–825, 2015.
- [15] C. Nielsen and S. Nemat-Nasser, "Crack healing in cross-ply composites observed by dynamic mechanical analysis," *Journal of the Mechanics and Physics of Solids*, vol. 76, pp. 193–207, 2015.
- [16] K. Horii, R. Yamada, and S. Harada, "Strength deterioration of nonfractal particle aggregates in simple shear flow," *Langmuir*, vol. 31, no. 29, pp. 7909–7918, 2015.
- [17] R. H. C. Wong, C. A. Tang, K. T. Chau, and P. Lin, "Splitting failure in brittle rocks containing pre-existing flaws under uniaxial compression," *Engineering Fracture Mechanics*, vol. 69, no. 17, pp. 1853–1871, 2002.
- [18] B. Shen, O. Stephansson, H. H. Einstein, and B. Ghahreman, "Coalescence of fractures under shear stresses in experiments," *Journal of Geophysical Research*, vol. 100, no. 4, pp. 5975–5990, 1995.
- [19] H. Jiefan, C. Ganglin, Z. Yonghong, and W. Ren, "An experimental study of the strain field development prior to failure of a marble plate under compression," *Tectonophysics*, vol. 175, no. 1–3, pp. 269–284, 1990.
- [20] J. T. Miller and H. H. Einstein, "Crack coalescence tests on granite," in *Proceedings of the 42nd US Rock Mechanics Symposium (USRMS '08)*, ARMA-08-162, San Francisco, Calif, USA, June 2008.
- [21] L. N. Y. Wong and H. H. Einstein, "Using high speed video imaging in the study of cracking processes in rock," *Geotechnical Testing Journal*, vol. 32, no. 2, pp. 164–180, 2009.
- [22] S. Nemat-Nasser and H. Horii, "Compression-induced nonplanar crack extension with application to splitting, exfoliation, and rockburst," *Journal of Geophysical Research*, vol. 87, no. 8, pp. 6805–6821, 1982.
- [23] S. Q. Yang, Y. H. Dai, L. J. Han, and Z. Q. Jin, "Experimental study on mechanical behavior of brittle marble samples containing different flaws under uniaxial compression," *Engineering Fracture Mechanics*, vol. 76, no. 12, pp. 1833–1845, 2009.
- [24] R. J. Fowell and C. Xu, "The use of the cracked Brazilian disc geometry for rock fracture investigations," *International Journal of Rock Mechanics and Mining Sciences and*, vol. 31, no. 6, pp. 571–579, 1994.
- [25] S. L. Crouch, "Analysis of stresses and displacements around underground excavations: an application of the displacement discontinuity method," University of Minnesota Geomechanics Report, University of Minnesota, Minneapolis, Minn, USA, 1967.
- [26] E. Hoek and E. T. Brown, *Underground Excavations in Rock*, Institute of Mining and Metallurgy, London, UK, 1980.
- [27] B. G. White, "Shear mechanism for mining-induced fractures applied to rock mechanics of coal mines," in *Proceedings of the 21st International Conference on Ground Control in Mining*, pp. 328–334, West Virginia University, Morgantown, WV, USA, 1999.
- [28] R. T. Ewy and N. G. W. Cook, "Deformation and fracture around cylindrical openings in rock—I. Observations and analysis of deformations," *International Journal of Rock Mechanics and Mining Sciences & Geomechanics Abstracts*, vol. 27, no. 5, pp. 387–407, 1990.
- [29] R. T. Ewy and N. G. W. Cook, "Deformation and fracture around cylindrical openings in rock—II. Initiation, growth and interaction of fractures," *International Journal of Rock Mechanics and Mining Sciences and*, vol. 27, no. 5, pp. 409–427, 1990.
- [30] A. A. Griffith, "The phenomena of rupture and flow in solids," *Philosophical Transactions of the Royal Society of London Series A*, vol. 221, pp. 163–198, 1921.
- [31] A. A. Griffith, "The theory of rupture," in *Proceedings of the 1st International Congress for Applied Mechanics*, pp. 55–63, Delft, The Netherlands, April 1924.
- [32] R. L. Kranz, "Crack-crack and crack-pore interactions in stressed granite," *International Journal of Rock Mechanics and Mining Sciences & Geomechanics Abstracts*, vol. 16, no. 1, pp. 37–47, 1979.
- [33] M. L. Batzle, G. Simmons, and R. W. Siegfried, "Microcrack closure in rocks under stress: direct observation," *Journal of Geophysical Research*, vol. 85, no. 12, pp. 7072–7090, 1980.
- [34] A. V. Dyskin, R. J. Jewell, H. Joer, E. Sahouryeh, and K. B. Ustinov, "Experiments on 3-D crack growth in uniaxial compression," *International Journal of Fracture*, vol. 65, no. 4, pp. R77–R83, 1994.
- [35] A. V. Dyskin, E. Sahouryeh, R. J. Jewell, H. Joer, and K. B. Ustinov, "Influence of shape and locations of initial 3-D cracks on their growth in uniaxial compression," *Engineering Fracture Mechanics*, vol. 70, no. 15, pp. 2115–2136, 2003.
- [36] A. V. Dyskin, L. N. Germanovich, R. J. Jewell, H. Joer, J. S. Krasinski, and K. K. Lee, "Study of 3-D mechanisms of crack growth and interaction in uniaxial compression," *ISRM News Journal*, vol. 2, no. 1, pp. 17–20, 1994.
- [37] A. Srivastava and S. Nemat-Nasser, "Overall dynamic properties of three-dimensional periodic elastic composites," *The Royal Society of London—Series A: Proceedings*, vol. 468, no. 2137, pp. 269–287, 2012.
- [38] C. K. Teng, X. C. Yin, and S. Y. Li, "An experimental investigation on 3D fractures of non-penetrating crack in plane samples," *Acta Oceanologica Sinica*, vol. 30, no. 4, pp. 371–378, 1987 (Chinese).
- [39] X. C. Yin, S. Y. Li, and H. Li, "Experimental study of interaction between two flanks of closed crack," *Acta Geophysica Sinica*, vol. 31, no. 3, pp. 307–314, 1988 (Chinese).
- [40] R. H. C. Wong, M. L. Huang, M. R. Jiao, C. A. Tang, and W. Zhu, "The mechanisms of crack propagation from surface 3-D fracture under uniaxial compression," *Key Engineering Materials*, vol. 261, no. 1, pp. 219–224, 2004.

- [41] R. H. C. Wong, Y. S. Guo, and L. Y. Li, "Anti-wing crack growth from surface flaw in real rock under uniaxial compression," in *Fracture of Nano and Engineering Materials and Structures: Proceedings of the 16th European Conference of Fracture, Alexandroupolis, Greece, July 3-7, 2006*, E. E. Gdoutos, Ed., pp. 825-826, Springer, Amsterdam, The Netherlands, 2006.
- [42] R. H. C. Wong, Y. S. Guo, and K. T. Chau, "The fracture mechanism of 3D surface fault with strain and acoustic emission measurement under axial compression," *Key Engineering Materials*, vol. 358, pp. 2360-3587, 2007.
- [43] Y. S. Guo, R. H. C. Wong, W. S. Zhu, K. T. Chau, and S. Li, "Study on fracture pattern of open surface-flaw in gabbro," *Chinese Journal of Rock Mechanics and Engineering*, vol. 26, no. 3, pp. 525-531, 2007.
- [44] L. Q. Liu, P. X. Liu, H. C. Wong, S. P. Ma, and Y. S. Guo, "Experimental investigation of three-dimensional propagation process from surface fault," *Science in China, Series D: Earth Sciences*, vol. 51, no. 10, pp. 1426-1435, 2008.
- [45] Y. S. Guo, *The study on experiment, theory and numerical simulation of fracture of three-dimensional flaws in brittle materials [Ph.D. thesis]*, Shandong University, Jinan, China, 2007.
- [46] R. H. C. Wong and K. T. Chau, "Crack coalescence in a rock-like material containing two cracks," *International Journal of Rock Mechanics and Mining Sciences*, vol. 35, no. 2, pp. 147-164, 1998.
- [47] M. F. Ashby and S. D. Hallam, "The failure of brittle solids containing small cracks under compressive stress states," *Acta Metallurgica*, vol. 34, no. 3, pp. 497-510, 1986.